Spectroscopic and photometric analysis of eclipsing close sdB binaries
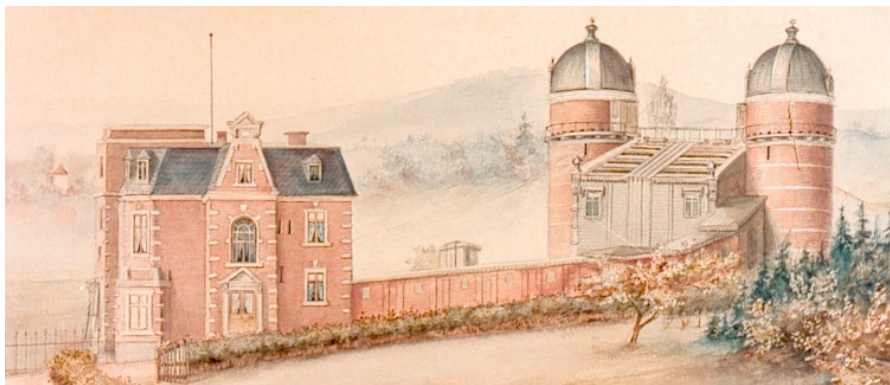
Masterarbeit aus der Physik

vorgelegt am **11. April 2018**

von **Maximilian Wolz**

Dr. Karl Remeis-Sternwarte

Astronomisches Institut der

Friedrich-Alexander-Universität Erlangen-Nürnberg

Betreuer: **Prof. Dr. Ulrich Heber**

Contents

1 Introduction

For thousands of years (and maybe much longer), the humans are interested in the night Sky. Advanced civilizations' remains show that they were able to observe orbital motions of planets, Moon, and Sun precisely and tried to find an order in the constellations of the stars. Although they discovered some remarkable findings - e.g. Aristarchus of Samos measured the radius of the Moon (unit: Earth radii), found a lower limit for the distance between Earth and Sun, and was the first proclaiming the heliocentric system -, astronomy was highly interleaved with mythology and astrology, because there was no sophisticated observing method, which is why many phenomena remained unknowable and mysterious. Hence, Sun, Moon, and planets were considered to be divinities, that were accordingly adored, and celestial constellations were considered to be responsible for all kinds of calamities.

To change this, science, especially math and physics, had to refine itself so that knew techniques and instruments could be devised - a process requiring for centuries. The invention of the refracting telescope by the Dutchman Hans Lipperhey and the keen observation of Mars's orbital motion by Tycho Brahe were of particular importance because these are considered indispensable requirements by the discoveries of Galileo Galilei (Galilean moons) and Johannes Kepler (Kepler's law of planetary motion).

The rapid technical progress, starting in the 19th century, allowed the further improvement of the telescopes as well as the invention of completely new astronomical observation techniques (e.g. photometry, spectroscopy, and most recently gravitational wave astronomy). With the help of these new methods, many discoveries changed our idea of the formation, the structure and the evolution of the stars and the Universe. Among other things, the development of the Harvard spectral classification - a system, which allows to make a statement about the surface temperature of a star only by its spectrum - as well as the Hertzsprung-Russell diagram, or, just a few years later, the development of physical models by Payne-Gaposchkin and Eddington respectively, which can give information about the stellar atmospheres and the stellar interior, are milestones of astronomic research.

Therefor, binary and multiple star systems played an important role to find physical regularities, because in contrast to single stars such as the Sun, binaries are gravitational bound and, hence, their components orbit around their common centre of mass. Using the classical mechanics of Newton, several parameters can be determined - in the most favourable case, masses and radii of the binary components just as the distance of the system to earth are included. Currently, the analysis of binary systems is the primary way of making a point about the masses and radii of stars, since it is only possible to determine these parameters with the accuracy needed, if we have a system showing eclipses (Eggleton, 2006). A large number of eclipsing binaries has to be analyzed in order to get an accurate comparative catalogue with which other stars can be classified. Furthermore, binaries can act as very good standard candles for distances in the nearby parts of the universe, because they occur masses, radii and - using the parallax - the distances to Earth. Since close binaries including a white dwarf (WD) are most likely progeni-

tors of Supernovae type Ia, they may also be important to derive the distances to other galaxies (Voigt, 2012).

This work deals with a special kind of close, eclipsing binary systems, the so-called HW Vir systems which consists of a hot subdwarf (sdO/B) star and a faint, low mass companion (usually an M- or a brown dwarf). These systems are quite rare, only 20 are currently known (Wolz et al., 2018). This work reports the spectroscopic and photometric observation and analysis of five previously unknown HW Vir systems and two non-eclipsing post-common-envelope sdB binaries with reflection effect. First, the actual knowledge of close binaries and the possible methods to analyze them are discussed in Chapter 2, ensuing the evolution and formation of hot subdwarf stars in Chapter 3. Following this, some important observational programs, especially those, of whose data are used in this work, are presented in Chapter 4. Chapter 5 elucidates the spectroscopic and photometric analysis methods, the used programs, and presents finally the analysis and the therefrom resulting findings for all seven binaries, before the most important conclusions are summarized in Chapter 6.

2 About binary stars

It is not easy to give an answer to the questions, what is a binary system and - on the other hand - what an isolated star, because the gravitational force has a longe-range impact. However, detailed observations of the night Sky showed that the separation between some stars is destinctly closer than it usually is for neighboured stars. There exist pairs of stars in which the two components are moving around their common centre of mass on Keplerian orbits, usually called binary system of stars, or just binary systems.

Although one would actually think, these systems are quite rare, extensive observational programs of the early eighties revealed that binary and multiple stars are approximately as abundant as isolated stars (Abt, 1983).

The following elucidations about binaries are mostly based on the textbooks of Eggleton (2006), Carroll & Ostlie (2007) and Hilditch (2001). Additionally utilized literature is cited in the usual way.

2.1 Classification of binary stars

The better the optical method engineering and the computer technique become, the better performed astronomical instruments such as telescopes or spectrographs, and computers could calculate models more accurate. Today, astronomers are able to determine a variety of stellar parameters and characteristics, even for isolated stars. Spectral analysis provides information on atmospheric parameters as effective temperature T_{eff}, surface gravity $log(g)$, or chemical abundances, but not on the stellar ones like mass and radius. Just the luminosity to mass ratio $\frac{L}{M}$ can be inferred from:

$$\frac{L}{M} \propto \frac{T_{\text{eff}}^4}{g} \tag{1}$$

Unfortunately, this won't give us the mass. The mass may only be derived by two different procedures: The first and more precise is a combination of photometric and spectroscopic analysis of eclipsing binaries as described in section 2.1.4 and performed in this thesis. The second needs a very accurate measurement of the stars' parallaxes. With the help of the distance and the visual magnitude m_v, the absolute magnitude M_v can be calculated using the distance modulus. Bolometric corrections from model atmospheres allow us to derive the bolometric magnitude M_{bol}, which is proportional to the luminosity of the star. Since luminosity and surface temperature are given now, one can determine the radius by $R \propto \frac{L^{0.5}}{T_{eff}^2}$. Finally, the mass follows from Eq. (1). But even if the parallax would have very small uncertainties, gravity is much less accurate because absorption lines are generally not as sensitive to gravity as required. Moreover, parallaxes with an accuracy of 10% or better are currently just available for a few stars closer than 100 pc. Consequently, masses calculated by means of the parallax show wide uncertainties and, thus, precise measurements of stellar masses are only possible by analysing the orbital data of binaries.

Depending on the system's geometry and distance from Earth, the observation and analysis methods, that were used to determine the orbital parameters, differ. Thus, it is obvious that binary stars are classified according to the method used at which we shall take a closer look at hereafter.

2.1.1 Visual binaries

A binary system is called visual if both stars are conspicuously separated and if they can be resolved independently by imaging. Usually, one can observe the motion of primary and secondary around their common centre of mass, except the orbital period is too long. Such binaries supply information about the members' angular separation to the barycentre of the system, the inclination i of the orbit to the line of sight, and the period P. If its distance is also known, it is possible to calculate the linear semi-major axes of the stars.

2.1.2 Astrometric binaries

Astronomers speak of an astrometric binary if the existence of one member can't be verified directly and, consequently, only one star is visible. This special kind of binary system exists normally in case of a significant difference of luminosity between the two components. The visible member shows a periodic variation of its proper motion which is caused by gravitational forces of the unseen companion. Only because of this oscillating proper motion of the visible star around the common centre of mass, this object can be identified as a binariy (Voigt, 2012).
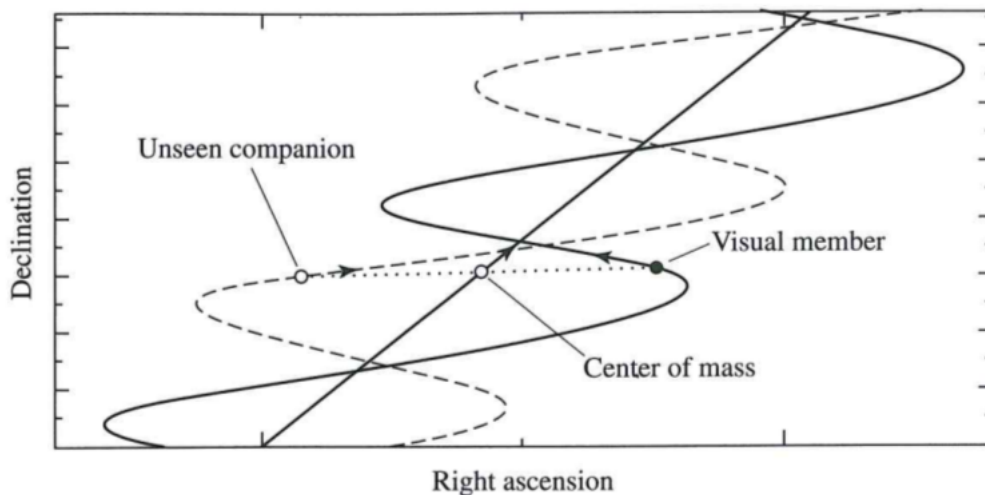
Figure 1: Sketch of an astrometric binary consisting of a visible primary and an unseen companion. The primary shows an oscillating motion which is indicative of the existing of the unseen star. The system's proper motion is reflected by the motion of the barycentre in a straight line (Carroll & Ostlie, 2007)

.

Astrometric measurements provide the period, the eccentricity e, and the inclination of the system, but since the mass ratio and in many cases also the parallaxes are unknown, no information

about their masses can be derived which is why the astrometric method plays a minor role in the detection and analysis of binaries.

2.1.3 Spectroscopic binaries

Spectroscopy is one of the most important and most powerful observation and analysis methods in astronomy. Therefor, spectrographs are used to disperse white, polychromatic light of a star according to its wavelength and, thus, make a statement about the nature of the star. Even if many different concepts of spectrographs exist, the basic principle, which is discussed in the following, is always the same (see Figure 2).

Firstly, the light of a star is focused by a telescope onto the entrance slit of the spectrograph. The slit is of particular importance, since the slit width b determines the resolution R of the recorded spectrum ($R \propto \frac{1}{b}$). Subsequently, the beam is parallelized by a collimator lens, before the light reaches the dispersive element - usually a prism or a grating, but also a combination of both, called grism, is possible. The dispersive element is the centrepiece of every spectrograph
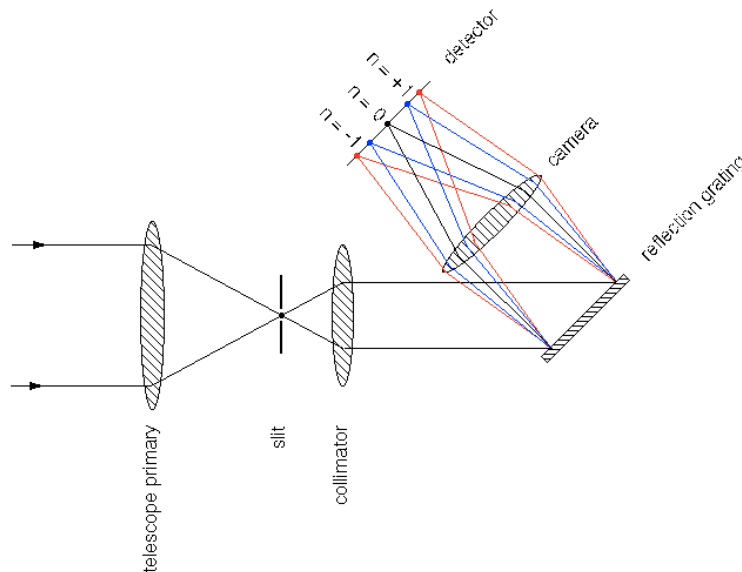
Figure 2: Functionality of a spectrograph using a reflective grating as dispersive element.[1]

because it separates the white light according to its wavelength following the dispersion relation and the Bragg condition. Afterwards, the dispersed light passes the camera lens, which is focusing the light onto the CCD chip of the detector. The CCD measures the incident intensity per pixel and generates hereby a digital image of the star's spectrum, that can be analyzed by computer programs (Irrgang, 2014).

When spectral analysis started in the mid to late 19th century with the Secchi (1863), scientist found out that spectral lines of the stellar spectra are caused by absorption. Experiments,

---

[1] http://www.vikdhillon.staff.shef.ac.uk/teaching/phy217/instruments/spectrograph_refl.png; Last access on: 02.02.18

performed in the late 19th century, proved that every absorption line is affiliated to a specific chemical element and, hence, every spectral line has a characteristic rest wavelength at its minimum. At the beginning of the 20th century, astronomers from Havard University detected a significant coherence of the effective temperature of a star and the presence of specific absorption lines in the spectra which is the basic of spectroscopic star classification.

The spectral analysis can be used to prove if a spectrum is recognisable of a binary or not. There are two different possibilities indicating that a spectrum originates from a binary: Either, the absorption lines are periodically shifted with wavelength (see Fig. 3) caused by the permanent orbital motion of the stars around their common centre of mass, or the spectrum is composite. In a composite spectrum, a combination of absorption lines can be seen, that would normally occur in the spectra of completely different spectral classes (e.g. Ca II in G-dwarf and He II in O-subdwarf spectra). Since we won't get any information on binaries' orbits from spectra, which show only compositions and no wavelength shifted absorption lines, we have to concentrate us in this work on wavelength shifted, spectroscopic binaries.
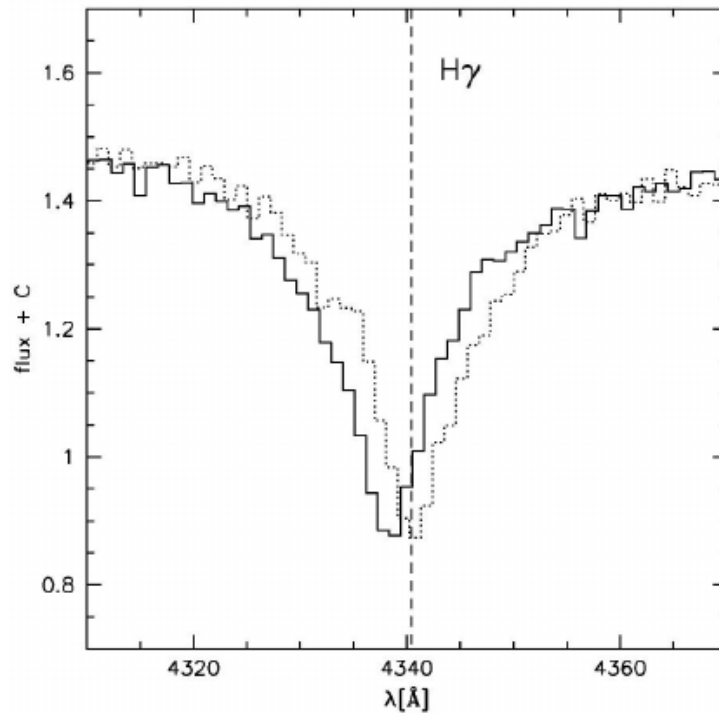
Figure 3: The shift of the H_γ line of a spectrum caused by the Doppler effect is shown. The grey, dotted line epitomizing the usual position of the H_γ absorption line at rest, while the full drawn profile marks the observed position of the hydrogen Balmer line. Obviously, H_γ is clearly blue shifted (Geier, 2015b).

If several spectra were consecutively recorded, the strength as well as the direction of the wavelength shift changes, which originates in the orbital motion of the stars around their barycentre, and, therefor, the stars are sometimes approaching (blueshift) and sometimes receding (redshift) from us. Using the Doppler formula $\frac{\Delta\lambda}{\lambda} = \frac{v_{rad}}{c}$, one may derive the radial velocities of

the stars at different times, which gives us, if plotted against time, the radial velocity curve (RV curve). Star systems with approximately circular orbits have constant velocities for both components, which is why the measured radial velocities of those binaries will produce a sinusoidal RV curve. If both stars are of comparable luminosity, both spectra are observable, but if the secondary is much fainter than the primary, the spectrum of the more luminous component will overwhelm that of its faint companion. In the first case, astronomers speak of a double-lined binary (SB1) while the second case is called single-lined binary (SB2) (see Fig. 4). Usually, spectroscopic binaries are single-lined, but also the RV variation of the single spectrum allows the period P, the eccentricity e, and the semiamplitude K_1 of the RV curve to be determined. The projected semi-major axis $a \cdot sin(i)$ can be obtained too, because it is correlated to the three parameters named before ($a \cdot sin(i) \propto K_1 P \sqrt{1 - e^2}$). Assuming the eccentricity to be zero, the following formula is derived for K_1:

$$K_1 = \frac{2\pi a}{P} \frac{M_2 sini}{M_1 + M_2}$$

$$\text{so that: } a = \frac{K_1 P}{2\pi} \frac{M_1 + M_2}{M_2 sini} \tag{2}$$

Now, we can plug in the result of the semi-major axis to the third law of Kepler yielding:

$$f(M_1, M_2) = \frac{K_{1,2}^3 P}{2\pi G} = \frac{M_2^3 sin^3 i}{(M_1 + M_2)^2} = \frac{M_2 sin^3 i}{(1 + \frac{M_1}{M_2})^2} \tag{3}$$

with the gravitational constant G and the inclination i. The units, that were used here, are $\frac{km}{s}$ for K_1, days for P, plus solar masses for $M_{1,2}$. The resulting formula is called mass function, convolving the masses of both stars as the unknown inclination i.
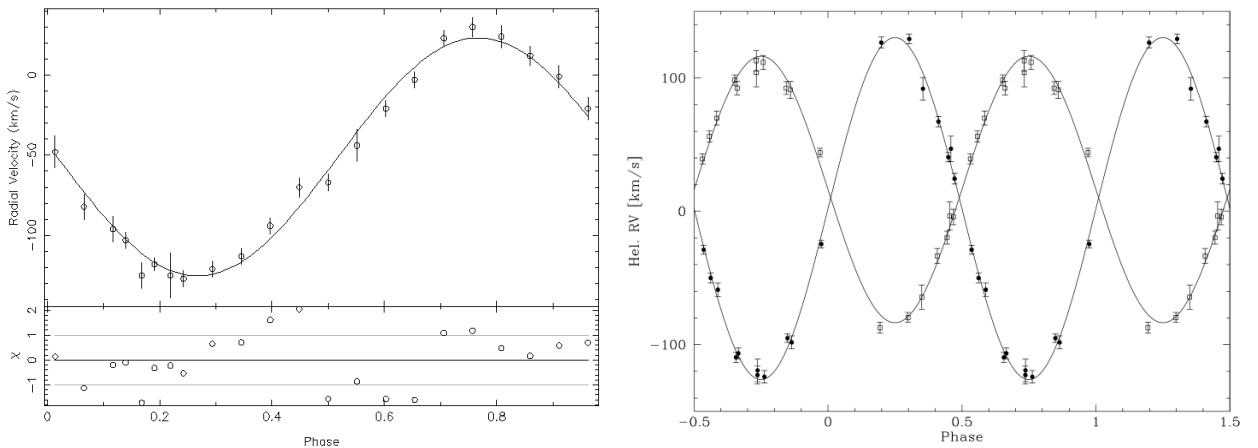

Figure 4: Left: Radial velocity curve of a single lined binary system (Wolz et al., 2018). Right: RV curve of a double-lined binary (Napiwotzki et al., 2002). Both curves are plotted against their orbital phase. Note: The right picture displays the RV curve plotted against two orbits, while the left picture presents just one orbital phase.

Eq. (2) shows the reciprocal proportionality between K_1 and P. Due to this correlation and the previously discussed proportionality between a and K_1, it ensues that the smaller the semi-major axis is, the larger is the semiamplitude. Consequently, an upper limit for the semi-major axis exist, where, if exceeded, wavelength shifts won't be detectable in the spectra anymore. Regardless of whether the spectroscopic binary is single- or double-lined, no information on inclination can be derived by spectroscopy, because only one dimension of orbital motion is known, namely the line of sight. Hence, the mass function depicts the lower mass limit for the unseen companion (case: $M_1 = 0$ and $sin(i) = 1$). Today, the only opportunity to determine the masses consists in studying a spectroscopic binary that does show eclipses, which have to be measured by photometry.

2.1.4 Eclipsing binaries

Eclipsing binaries are systems with high inclination angles so that each star may pass periodically in front of the other as seen from Earth. If a binary does show eclipses in the observer's line of sight, light of the eclipsed component gets blocked causing periodic brightness variations. By measuring the magnitude or the flux of the system at many several times, astronomers are able to detect these variations. During one orbit, two eclipses occur. The first, known as primary eclipse, takes place, when the fainter companion, called secondary, is crossing the more luminous primary. The second happens conversely, in other words, if the secondary is behind the primary star. As seen in Fig. 5, the variations' extent depends on the radii of the stars and their luminosity: The larger the transiting star compared to the transited one is, the longer the
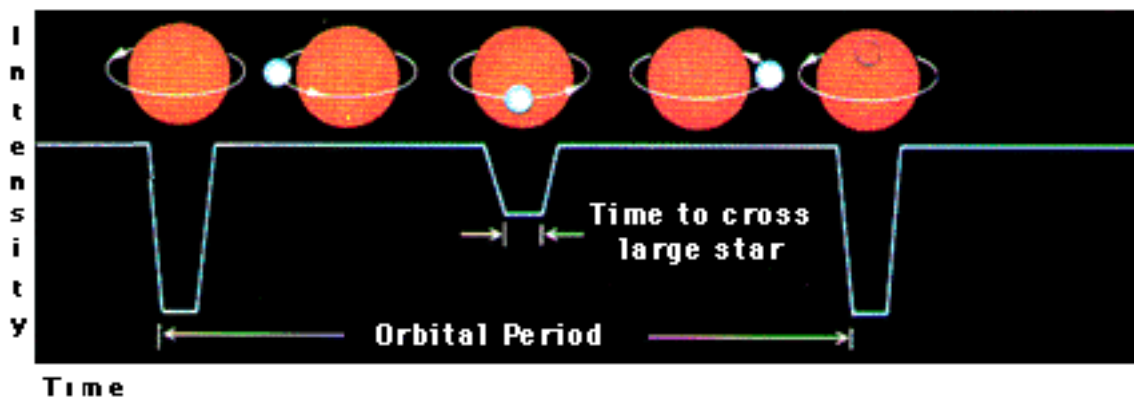
Figure 5: Graphical illustration of the light curve of an eclipsing binary with an inclination angle close to $90°$.[2]

eclipse takes; one the other hand, we have: The higher the luminosity ratio $\frac{L_1}{L_2}$ - where L_1 is the luminosity of the brighter companion - the deeper the primary minimum and the shallower the secondary minimum, respectively. The large majority of eclipsing binary stars have short orbital periods; just 10% of them need more then ten days for one orbit. Hence, most eclipsing

---

[2]https://imagine.gsfc.nasa.gov/educators/hera_college/eclipsing_binary.gif; last access on: 06.02.18

systems are close binaries. This is traced back to the fact, that the possible inclination range, at which the eclipses are visible, gets smaller with increasing system's separation (Voigt, 2012). The light curve analysis can yield the period P, the eccentricity e, the inclination angle i as well as the ratios of the components' radii to the orbital semi-major axis ($\frac{R_1}{a}$ and $\frac{R_2}{a}$). Fortunately, eclipsing binaries are usually variable in radial velocity too. Using the spectroscopic and photometric data of a binary, astronomers may determine besides the orbital parameters the masses and the radii of both stars. On closer consideration of Fig. 5, one can see that the eclipses show partial and total segments. The range between the first contact t_1, where intensity starts to decrease, and the reaching of the minimum t_2 is called partial eclipse as well as, conversely, the section between the end of the minimum t_3 and the last contact t_4. The ratio of the radii to the orbital semi-major axis is approximately given by

$$\frac{t_4 - t_1}{P} = \frac{D_1 + D_2}{L} = \frac{2(R_1 + R_2)}{2\pi a} \tag{4}$$

with the stellar diameters $D_{1,2}$ and the length L of the related orbit.

Deriving stellar parameters from photometry is much more difficult than from spectroscopy since the light curve depends on geometric principles, while the RV curve is liable to dynamical laws. Compared to spectroscopy, much more parameters have to be considered for the photometric analysis which is why a sophisticated model is needed including all effects that may change the light curve's shape. Usually, scientists assume both stars to fill equipotential surfaces of the Roche-potential which will be discussed in section 2.2. Previously, the most important effects got itemized and shortly elucidated (see e.g. Hilditch, 2001, for a review).

- **Ellipsoidal deformation:** The closer binaries are, the stronger become the interacting forces because these forces are inversely proportional to the tidal separation of both components. Hence, gravity may get so strong for very close binaries - especially for a compact and massive companion - that one or both components will show ellipsoidal deformations due to the tidal forces. This results to a periodic variability of the measured flux depending on the size of the cross sectional area in the observer's line of sight (see Fig. 6, right curve). Consequently, the measured flux reaches its maximum if the seen cross sectional area gets maximum. The period of the light variation, which is caused by ellipsoidal deformation, is amounted to half of the orbital period.

- **Reflection effect:** Close binary stars won't affect each other just gravitational. If the system is gravitationally bound into synchronous rotation, and the primary has a significantly higher effective temperature than its companion, the hemisphere of the cooler component, facing the hotter one, is heated up by the radiation of the primary. Since intensity and temperature are highly correlated (see Stefan-Boltzmann law), radiation from the heated side of the secondary will be more intense, which means, the more of the companion's heated half is visible for an observer, the higher the measured flux. Hereby, a continually changing, periodic effect - called reflection effect - is created onto the light
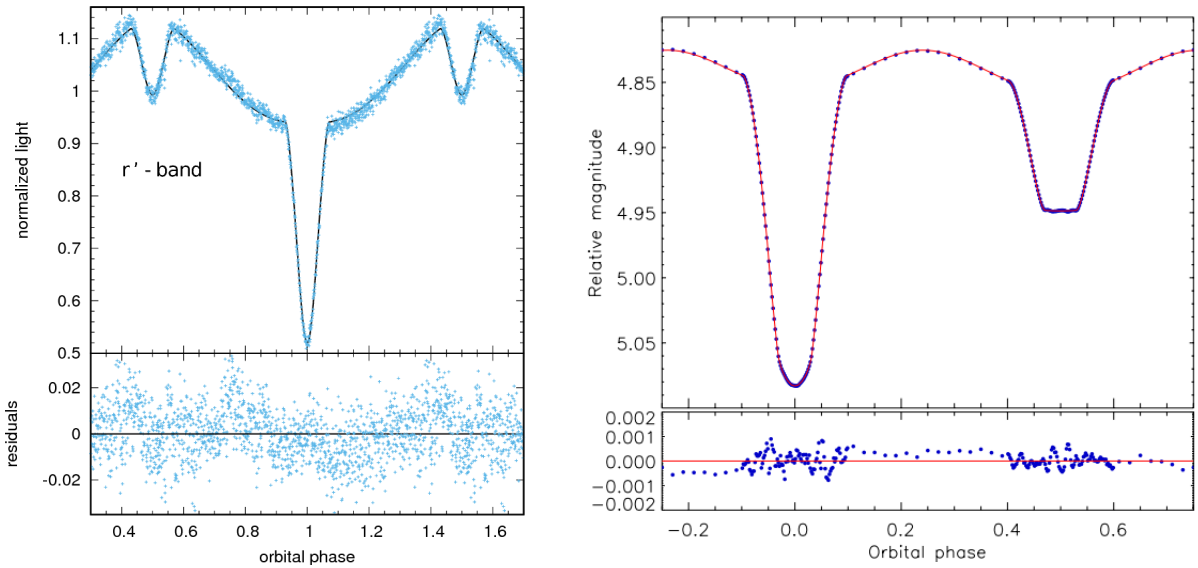
Figure 6: In this figure, the light curves of two different systems are shown. The plots are consisting of the measured data points, the synthetic light curves, which is fitted to the measurements, and below the residuals are illustrated. Left: Fitted light curve with reflection effect and eclipses showing 1.5 orbits (Wolz et al., 2018), right: Fitted light curve showing ellipsoidal deformations as well as eclipses (Lehmann et al., 2013)

.

curve (see Fig. 6, left side). The period of the reflection effect corresponds to the orbital period. While ellipsoidal deformations occur for massive and compact companions, the reflection effect requires a huge secondary with a large surface, which can be heated up by primary's radiation.

- **Limb darkening:** At the beginning of the 20th century, the German physicist Karl Schwarzschild could prove that stars are consisting of gas whose temperature and density is decreasing outwards. This does result in a not uniform illumination of the projected star disc, the limb of the disc appears to be darker than its centre. Accordingly, this effect is called limb darkening. Limb darkening occurs because the column density as well as the optical depth of the stars are changing with the distance to the centre.

- **Gravitational darkening:** If a star rotates very fast, it will be flattened and the local effective gravity will change with latitude resulting in a flux variation at its surface. This effect is mentioned as gravity darkening (Espinosa Lara & Rieutord, 2012). The ellipsoidal deformations occur due to centrifugal forces. Since the centrifugal force at a point *P* of the stellar surface is proportional to its distance to the rotational axis, the centrifugal force is minimum at the poles and reaches its maximum at the equator. As a consequence, this force pushes the gas near the surface from the poles to the regions of lower latitudes resulting in lower pressures in the equatorial area than near the poles. Furthermore, pressure and effective temperature are highly correlated which is why fast rotators possess

higher temperatures at the poles than at the equator. Using Stefan-Boltzmann's law, we obtain that rapidly rotating stars are fainter at their equators where effective gravity has lower values than at the poles.
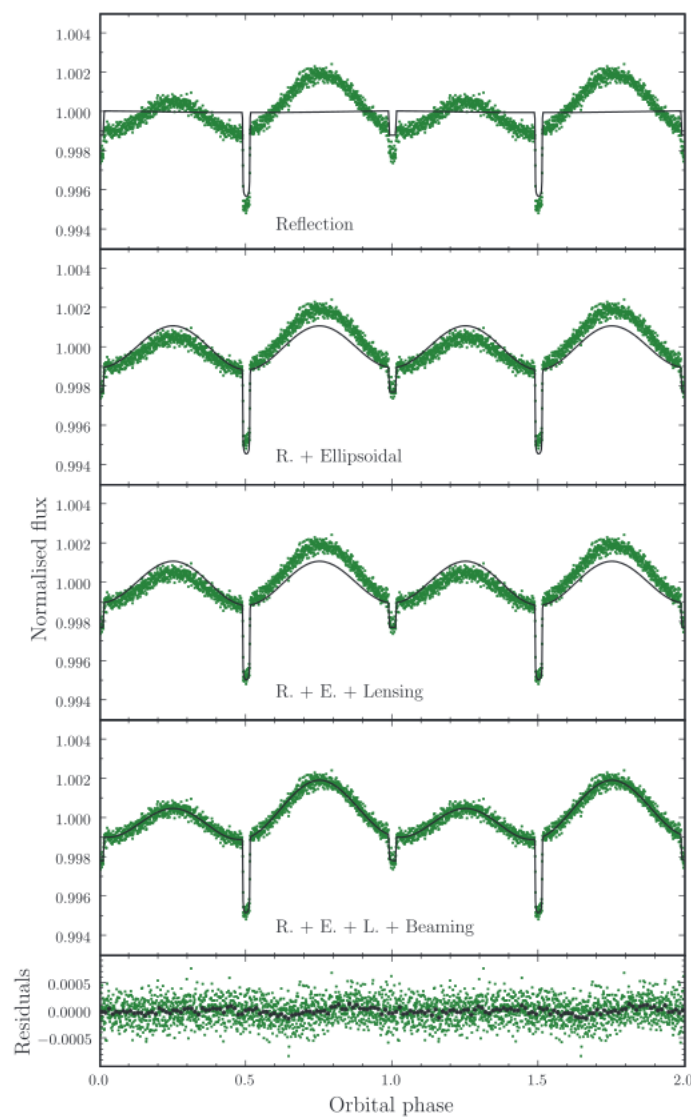
Figure 7: Impact of reflection effect, ellipsoidal deformation, gravitational lensing, and Doppler beaming to the light curve's shape (Bloemen et al., 2011).

Moreover, there are two further effects basing on Einstein's general relativity, known as gravitational lensing and Doppler beaming. Both effects have the lowest impact to the light curve of all discussed effects.

- **Doppler beaming (boosting):** There are two different effects that were usually called Doppler beaming even if their occurrence is caused by different phenomena. To make a clear distinction between these two effects, we call the first rotational and the second orbital Doppler beaming. Rotational Doppler beaming occurs if both binary components

are fast rotators and if the system does show eclipses. Especially in close binary systems, where the stars are gravitationally bounded, rotational Doppler beaming should be detectable. This effect behaves similarly to the well studied Rossiter-McLaughlin effect: Because of the star's rotation one half of the star approaches from us, while the other half recedes resulting in a blue- and redshift, respectively, according to Doppler formula. Since this is a symmetric effect, blue- and redshift usually neutralize each other. But during eclipse ingress and egress, when the transiting star covers just a part of the other component, the axial symmetry is canceled (Groot, 2012). Actually, this phenomenon is just of theoretical nature - it wasn't detected yet.

Orbital Doppler beaming is more important and occurs if the radial velocities of the binary components are quite high. Hot stars may assumed to be black bodies, because the maximum of intensity lies in the Rayleigh-Jeans range according to Wien's displacement law. This is changing the light curves values by $(1 - \frac{v_{rad}}{c})^3$. In the optical, a shift of $1 - \frac{v_{rad}}{c}$ is detectable because the Doppler effect causes a factor given by $(1 - \frac{v_{rad}}{c})^{-2}$ (see Maxted et al., 2000; Loeb & Gaudi, 2003). However, the orbital Doppler beaming leads to asymmetries in the light curve's shape: one ellipsoidal maximum gets amplified, while the other one is weakened, as one can see in the lowest panel of Fig. 7.

- **Gravitational lensing:** Astronomers refer to gravitational lensing if a massive celestial body is causing a brightening of another object while it crosses in front of the other one. This effect originates in the fact that very massive orbs act to light as a lens - they can bend light by curving the space-time. But while normal lenses deflect the course of light the more the further it passes the lens on their edge, conversely, gravitational lenses changes the way of light especially in the near of the massive object, because the space is mostly curved close to the heavy mass. In photometric binary systems, gravitational lensing is observable during the eclipses. This effect has especially consequences to the depth of of the light curves minima, which are caused by eclipses, and will slightly decreasing it (see Fig. 7, third panel).

2.2 Roche model, Lagrangian points and mass transfer

As discussed in the previous section, the two binary components influence each other gravitationally, and the closer the system, the stronger the mutual exerted forces. If all binaries would be well detached, so that the gravitational and tidal forces won't cause any ellipsoidal deformations, then an easy mathematic formulation using the Legendre polynomials would suffice to describe their shapes and formation. But some of these systems are so close, that the stellar surfaces of the two components are nearly touching each other, and the light curve clearly shows the ellipsoidal deformation of the stars. Hence, a universal mathematical formulation is needed describing the shapes of the binary stars in all possible cases. Such a formulation was provided by the French mathematician Edouard Roche in the late 19th century when he tried to solve the three-body problem. Thereby, he found an analytic solution for a special case of the general

three-body problem, the so called restricted three-body problem. In the quest for the solution, Roche assumed two bodies to be point masses moving on circular orbits around their common centre of mass, whilst the third, an infinitesimally small mass, moves in the gravitational field of the two masses. By means of this third, infinitesimal mass, Roche was able to determine the gravitational potential Φ at every position P. Furthermore, Roche could prove that one can construct a three-dimensional hypothetical surface around the the two mass points for a given value of Φ. This surface represents the areas where the third body's velocity would be zero relative to the uniformly rotating coordinate system of the two masses circling around their common centre of mass. While surfaces of zero velocity, that were further away from the two massive bodies, enclosing both, surfaces close to the masses won't show this behavior (Hilditch, 2001). In the following, the most important mathematical formula describing the Roche potential are introduced and motivated shortly. For a detailed review, the textbooks of Kopal (1989), Hilditch (2001), and Carroll & Ostlie (2007) are reffered.

To simplify this complex three-dimensional problem, we assume the orbits of the two masses to be circular and located in the x-y-plane, so that both masses are rotating around their common centre of mass with constant angular speed ω. Furthermore, we consider a co-rotating coordi-
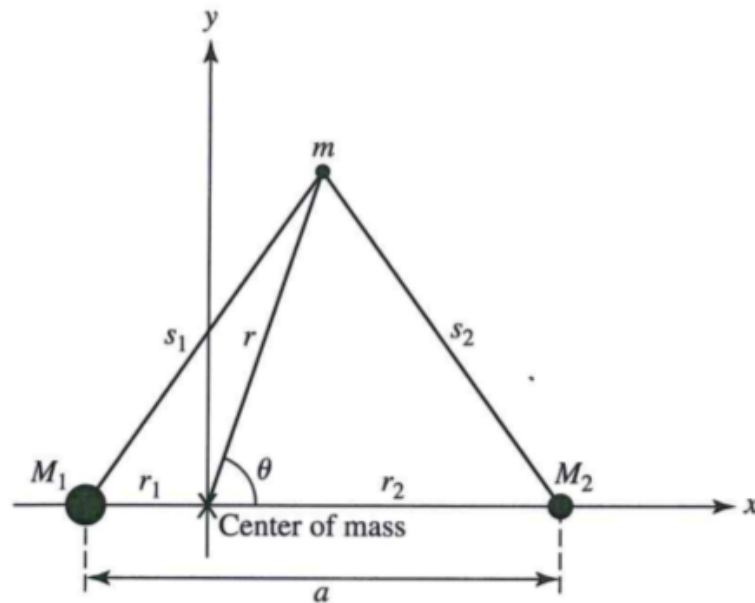
Figure 8: Co-rotating coordination system of a close system in which two massive bodies M_1 and M_2 orbiting each other, where $M_1 > M_2$. An X marks their common centre of mass, and m epitomizing the infinitesimal mass of the third body (Carroll & Ostlie, 2007).

nate system where the barycentre is located at the origin. The point masses M_1 and M_2, where M_1 is more massive, have a distance a to each other, and have a distance r_1 and r_2, respectively, to their common centre of mass. Furthermore, the test mass m is located at a distance r to the barycentre - the distances to the massive bodies are s_1 and s_2, respectively. Using the centre-of-mass theorem and the potential energy of the system, a mathematical description of the effective

gravitational potential is given by:

$$\Phi = -\frac{GM_1}{s_1} - \frac{GM_2}{s_2} - \frac{\omega^2 r^2}{2} \tag{5}$$

The value of the angular speed ω can be calculated for every system applying the third law of Kepler: $\omega^2 = (\frac{2\pi}{P})^2 = G\frac{M_1+M_2}{a^3} = G(M_1+M_2)$. In the last step, we convert the distances to units of separation (and thus: $a \equiv 1$). By means of this correlation, we are able to define the normalized potential Φ_n, which is dimensionless:

$$\Phi_n = -\frac{2\Phi}{G(M_1+M_2)} = \frac{2}{(1+q)s_1} + \frac{2q}{(1+q)s_2} + r^2 \tag{6}$$

where $q = \frac{M_2}{M_1}$ is the mass ratio. This normalized potential is known as the Roche potential.
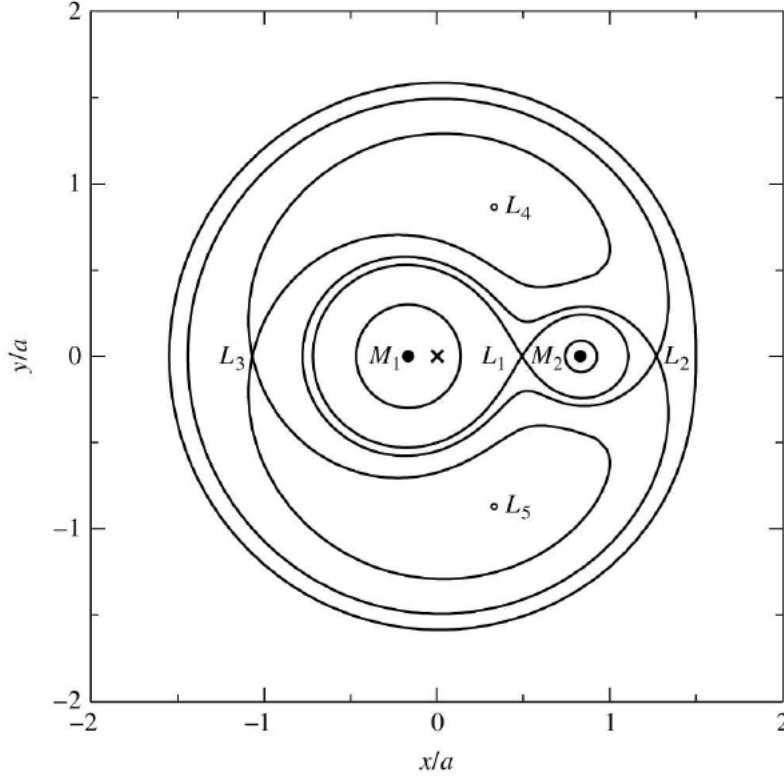
Figure 9: Cross section of the equipotential in the orbital plane for $M_1 = 0.85M_\odot$, $M_2 = 0.17M_\odot$ and $a = 5 \cdot 10^8$m. The barycentre is placed at the origin. In this figure, Φ was plotted in units of $\frac{G(M_1+M_2)}{a}$ (here: $2.71 \cdot 10^{11} \frac{J}{kg}$). Starting at the top of the outline and moving then down to the barycentre, one get the following values for the normalized gravitational potential: $\Phi_n =$ -1.875, -1.768, -1.583, -1.583, -1.768, -1.875 and -3. Also marked are the Lagrangian points, where L_4 and L_5 are the global maxima of the potential (Carroll & Ostlie, 2007).

Usually, the distances $s_{1,2}$ of the two point masses to the test mass are not known, but they can be calculated with the help of the law of cosines, the distances $r_{1,2}$, and the angle θ between the

centre of mass, m and M_2 (see Fig. 8). We obtain:

$$s_1 = \sqrt{r_1^2 + r^2 + 2r_1 cos\theta}$$
$$s_2 = \sqrt{r_1^2 + r^2 - 2r_1 cos\theta}$$

(7)

The results, discussed so far, can be utilized to determine the normalized gravitational potential for every position $P(x,y,z)$ of the three-dimensional space. If a force effects on m, we can describe it by:

$$F = -m\frac{\partial \Phi}{\partial r}$$

(8)

Calculating the gravitational potential and, thus, the form of the equipotential surfaces around the two massive bodies, one will find several points where F becomes zero and $\frac{\partial \Phi}{\partial r} = 0$ applies - the Lagrangian points. Hence, we found local extrema of the gravitational potential encircling the two components. As seen in Fig. 9, three of the Lagrangian points are positioned on a straight line joining the two masses and their common centre of mass, where one of the three points, labeled as L_1, is located between the two mass points. This point is called the inner Lagrangian point.

Furthermore, Fig. 9 shows several equipotential surfaces for different values of Φ_n. Surfaces close to the masses M_1 or M_2 look nearly spherical, but, further away, the mutual gravitational influence of both masses deform the equipotential surfaces until they touch at the inner Lagrangian point, which is, hence, a local, instable saddle point of the gravitational potential. The surfaces, that touch each other at L_1, are referred to as Roche limits for the two bodies defining a three-dimensional, teardrop like limit for the maximum volumes of both stars, usually called the Roche lobes up to which a star in a binary can gravitationally hold its mass. Their volumes may be calculated with the help of the Roche radius R_L - this is the radius of a sphere owning the same volume as the Roche lobe - given for the primary by

$$\frac{R_L}{a} \approx \frac{0.49q^{2/3}}{0.6q^{2/3} + ln(1+q^{1/3})}, 0 < q < \infty$$
$$\approx \frac{0.44q^{0.33}}{(1+q)^{0.2}}, 0.1 < q < 10$$

(9)

where $q = \frac{M_1}{M_2}$ is the mass ratio (Eggleton, 2006). The Roche radius of the secondary can be derived by using the inverse mass ratio $Q = \frac{M_2}{M_1}$

However, if a star becomes too large to fit inside its Roche lobe, its envelope won't be stable anymore and parts of its matter may be transfered from one star to its companion. As already seen for the potential, also the size of the Roche lobes depends on the system's separation a as well as on the mass ratio of the two stars. Hence, if both stars have the same mass, they would possess Roche lobes of same sizes. Beyond the equipotential surface, that includes L_1, we have a region, where a test mass would feel the influence af both stars. Consequently, the equipotential surfaces surround both stars and, if both stars would fill their Roche lobes, mass

would fill this region and a common-envelope would emerge showing a "peanut shape" (see Fig. 9). The common-envelope is surrounded by another equipotential surface owning a gravitational potential Φ_n with a somewhat higher value than the common-envelope possesses. This surface encompasses not only the region of the common-envelope but also the entire system. While its cross section with the orbital plane is almost spherical for the outer parts, there exists a point on the line of masses, where the surface is clearly non-spherical. This point, also named outer Lagrangian point L_2, is the only intersection of the inner and the outer part of this equipotential surface and, as a consequence, L_2 is the point, through which matter can escape the common-envelope in the most easiest way. On the other hand, all masses, that were located beyond this surface, are not part of the systems' common-envelope anymore, but are forced to a Keplerian orbit around the two stars (Voigt, 2012).

On the other side of the line of the sight, another Lagrangian point L_3 exists representing an alternative escape path to L_2 through an area of higher gravitational potential. Hence, its easier for matter to overcome L_2 than L_3 (see Fig. 10).
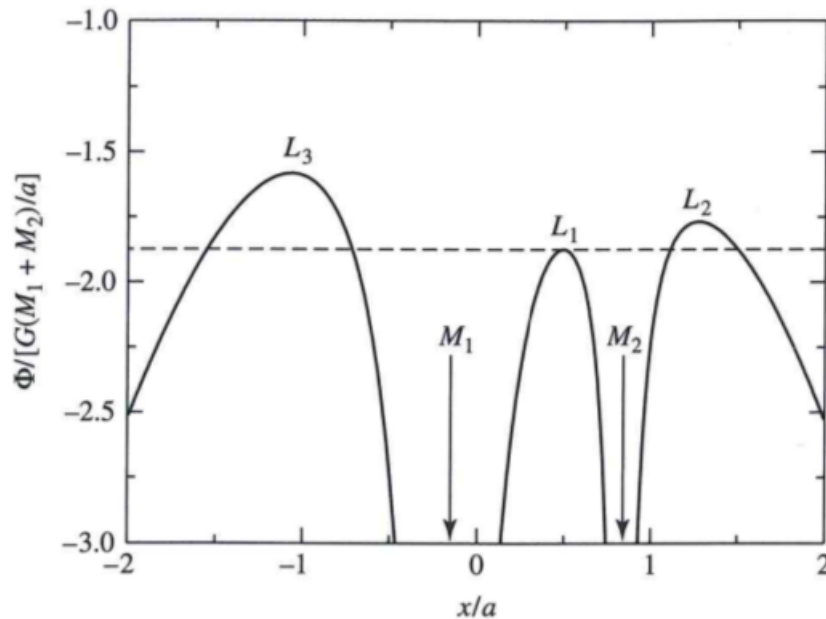
Figure 10: Shape of the effective gravitational potential Φ of a binary consisting of two stars with the masses $M_1 = 0.85 M_\odot$ and $M_2 = 0.17 M_\odot$. Their common centre of mass is located at the origin of the x-axis. The dash dotted line marks the value of the potential at the inner Lagrangian point L_1 (Carroll & Ostlie, 2007).

2.3 Classes of close binaries

The classification of close binaries depends on the size of the stars with respect to the Roche radius. Accordingly, three different kinds of close binary systems were distinguished: The first group of close binaries are the detached systems. Here, both stars have radii, that were much smaller than their separation and, consequently, they don't fill their Roche lobe completely.

Detached binary stars are usually almost spherical and evolve nearly independent (see Fig. 11). The second class is called semi-detached binaries. These systems consists of a star reaching its Roche limit while the other doesn't. In such a binary, mass can be transfered from the larger primary, that fills its Roche lobe, to the smaller secondary. For example, such a binary may occur if a detached system is composed of two main sequence stars with different masses, so that the more massive star evolves faster than its companion. After hydrogen burning ceases in the core, shell burning starts causing a slight expansion of the envelope - the star becomes a red giant. When the primary expands, the star will eventually fill its Roche lobe. While further extension, the star can't gravitationally bind the outer parts of its envelope anymore. Instead, mass will be transfered from the red giant to its companion via the inner Lagrangian point which is still located at the main sequence (Carroll & Ostlie, 2007).

Sometimes, it may happens, that both stars will fill their Roche lobes. In this case, neither the primary nor the secondary can transfer atmospheric gas, which they can't gravitationally bind anymore, to its companion. Then, the two stars share a common atmosphere confined by a peanut shaped gravitational potential. Astronomers name such a system a contact binary.
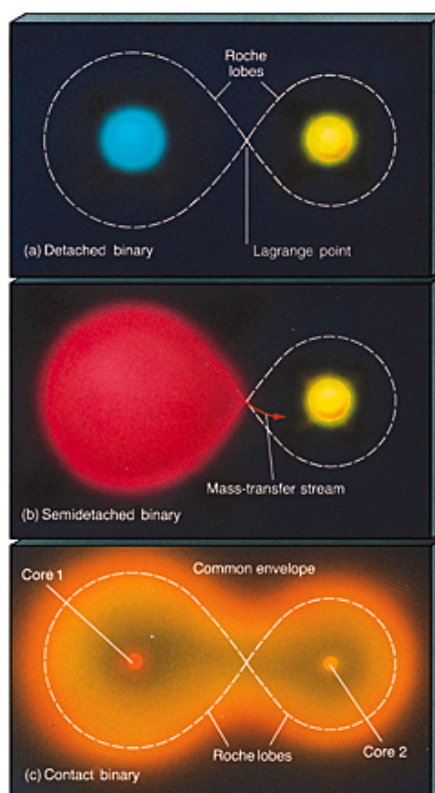
Figure 11: The upper figure outlines the appearance of a detached system, where both stars are nearly spherical. The figure in the middle shows a so-called semi-detached binary, meaning one star fills it entire Roche lobe, while the other doesn't. In this case mass transfer from the star, which fills its Roche lobe, to its companion may occur. The figure in the bottom epitomizes a contact binary, in which both stars fill their Roche lobes. Consequently, none of them can transfer mass through the inner Lagrangian point to the other, which is why a common-envelope develops. The Roche lobes are marked with a dash-dotted line in each figure.[3]

3 Hot subdwarfs

Due to the mass-luminosity relation, more massive, hot stars spend less time on the main sequence than less massive, cooler stars such as the Sun. For this reason, astronomers expected no radiation in the far-UV, when they observed old, ellipsoidal galaxies which should only contain low mass, red shining, late-type dwarfs and giants (according to their large age of more than ten billion years). All the more, they were very surprised when they checked the first far-ultraviolet images of ellipsoidal galaxies taken by the NASA mission "orbiting astronomical observatory" in 1969, because UV light was clearly detected against the established theory of that time. According to this theory, old galaxies should only emit light in the optical and infrared range because they consists solely of late type dwarfs and giants. The effect was therefor called the "UV-upturn" or the "UV rising-branch" (O'Connell, 1999).
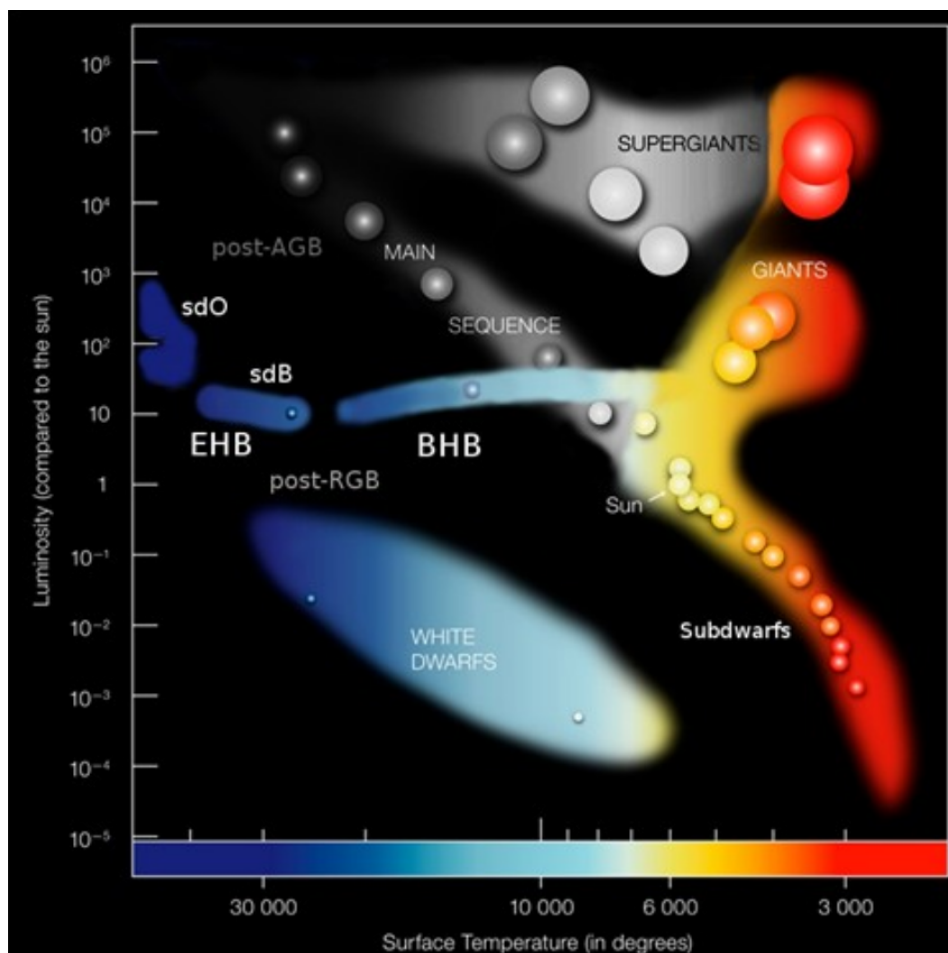
Figure 12: Position of the hot subdwarf (marked with sdO and sdB) in a Hertzsprung-Russel diagram (Heber, 2009).

During the following years, astronomers puzzled their head over the origin of the UV-upturn, but they could not find an answer because no further data with high resolution were available at this

---

time. This changed in the early 1990s when Ferguson et al. could prove by using the Hopkins Ultraviolet Telescope (HUT) that the emitted radiation was not caused by a few hot, luminous, young main sequence stars, but rather by older and fainter helium-burning stars showing effective temperatures around 25000 K. These special stars turned out to be hot subdwarfs, these are core helium-burning stars which were firstly described in the 1950s, but in another context. The technical terms, which are usually applied for these stars, is sdO and sdB, respectively, where the last letter denotes the spectral type belonging to their absorption spectra. While the effective temperatures of hot subdwarfs are similar to that of the corresponding dwarfs, their luminosities don't since the luminosity of a star is highly correlated with its radius ($L \propto T_{\mathrm{eff}}^4 R^2$), meaning that subdwarfs' radii must be much smaller than the solar radius. The radii of the most sdOs and sdBs are found to be in a range between 0.1 and 0.35 solar radii. Nevertheless, hot subdwarfs are ten to hundred times more luminous than the Sun (Geier, 2015a).

Because hot subdwarfs are core helium-burning, they are, as a consequence, part of the horizontal branch (HB). Due to their high effective temperatures, they lie on the hot end of the HB, the so-called extreme horizontal branch (EHB), which is why sdO and sdB stars mark the blue end of the HB in a Hertzsprung-Russel diagram, as can be seen in Fig. 12. Since they are not as luminous as usual main sequence O- or B-type stars, hot subdwarfs are also called hot subluminous stars.

Hot subdwarfs are very interesting celestial objects because most of the sdO/-B stars are variable stars, meaning they show periodic light variations i.a. due to pulsations (Kilkenny et al., 1997). For this reason, hot subluminous stars are interesting targets for astroseismology which may provide information about their stellar structure. Astroseismologic analysis allows the inner structure of stars to be probed by measuring the refractive index through sound waves and, thus, one can obtain information about the star's mass which can usually be derived only for eclipsing, and concurrently double-lined spectroscopic binaries (see Sect. 2.1).

Although many parameters of the atmospheres, the stellar structure, etc. of hot subdwarfs could have been derived, their origin remained unresolved because no stellar evolution model exists in which hot, subluminous core helium-burning stars would occur. Today, many theories about sdOs' and sdBs' formation are available, but not all mechanism, that they require, are fully understood. The following section shall give a short summary of the most important formation theories of hot subluminous stars.

3.1 Evolution of hot subdwarfs

To generate such a hot, subluminous, core helium-burning star, its progenitor has necessarily left the main sequence joining the red giant branch (RGB). Due to the small radii and the high surface temperatures of an sdB star, the giant has to lose its entire hydrogen envelope before reaching the tip of the RGB. In recent years, astronomers have found out that more than 50% of the sdB stars evolve in close binaries with periods below 30 days (Maxted et al., 2001; Morales-Rueda et al., 2003). Hence, astronomers have to develop models for subdwarfs depending on

whether they are part of a binary or not. Firstly, we will discuss the formation channels for sdB stars in a binary scenario, then the evolutionary tracks for single stars. The description of the formation channels, following below, is based on Han et al. (2002) and Podsiadlowski et al. (2008).

If the progenitor of an sdB star is part of a binary system, it usually has to fill its Roche lobe near the tip of the RGB in order to lose its envelope, hence, a semi-detached system is needed. Depending on how fast the red giant is expanding, two different cases may occur:

If the red giant won't rapidly expand to and over its Roche limit, its companion is able to accrete all the matter that is passing the Lagrangian point - a stable mass transfer ensues, also called stable Roche lobe overflow (stable RLOF). But it may also happen that the red giant expands too fast and, thus, its hydrogen-rich envelope expand too quickly beyond the giants' Roche lobe to get fully accreted by the companion, a scenario, which astronomers have named the unstable RLOF. As a consequence, the accretion disc is rapidly increasing finally reaching the Roche limit of the companion, so that excessing matter from the giant will stream to areas of higher gravitational potential Φ which surrounds both binary stars forming a common-envelope (CE). The emergence of a hot subdwarf in a binary scenario depends on the system's mass ratio $q = \frac{M_1}{M_2}$, where the more massive star of the original system is called primary.

If both stars have fairly similar masses, so that the mass ratio is $q < 1.2$-1.5, two different phases of mass transfer occur. The original binary system is assumed to have a separation of a few AU and consists of two main sequence stars. Because the more massive primary evolves faster, it leaves the main sequence first joining the red giant branch. While the shell hydrogen-burning starts in the primary, its envelope begins to extent reaching soon the stars Roche lobe. Since its companion is still on the main sequence, which is why the secondary doesn't fill its Roche lobe, this leads to a stable RLOF. After the red giant has transfered almost its entire envelope, a helium white dwarf (He WD) and a more massive MS star remain in a wide binary. As a consequence of the mass transfer, the mass ratio of the stars has completely changed. It is approximately given by: $Q = \frac{1}{q} = \frac{M_2}{M_1} > 1.2$-$1.5$. After billions of years, also the companion will have fused its hydrogen to helium in its core and, hence, will follow the same path as the primary did before - it will become a red giant and fill its Roche lobe causing a mass transfer to its companion. But compared to the first RLOF, the mass ratio is much larger and a WD reacts differently to normal stars, when its mass is increasing. While normal stars enlarge their radii with mass, white dwarfs (and also their Roche limit) are shrinking according to the mass-radius relationship of white dwarfs. For these reasons, the white dwarf is not able to accrete all the matter of the giant floating over the inner Lagrangian point. Consequently, the WD starts to fill and finally overfill its Roche lobe leading to the formation of a common-envelope. During the common-envelope phase, friction between the helium cores of both stars and the envelope causes a transfer of angular momentum and energy from the orbit planes to the common-envelope. The loss of angular momentum leads to a spiral-in phase of the cores, which is ongoing, until enough orbital energy was released to eject the CE, as seen on the left side of Fig. 13. A much closer binary system remains with orbital periods of $P \approx 0.1 - 40$d consisting of a He WD and the core of the giant

which is now called a hot subdwarf.

If the mass ratio of the original wide binary is larger than $q > 1.2$-1.5, then the unstable RLOF occurs as soon as the primary evolve into a red giant and overfills its Roche lobe. The appearance of the common-envelope phase is similar to the one described before: The immersed cores lose angular momentum and energy due to friction to the envelope, which is why the spiral towards each other until the envelope is ejected (see Fig. 13, right side). After the ejection, a very close sdB + MS binary remains showing periods about $P \approx 0.1$-10d and sdB masses between 0.4 and 0.47 solar masses. In the best-fit models of Han et al. (2003), the birthrates of sdB stars
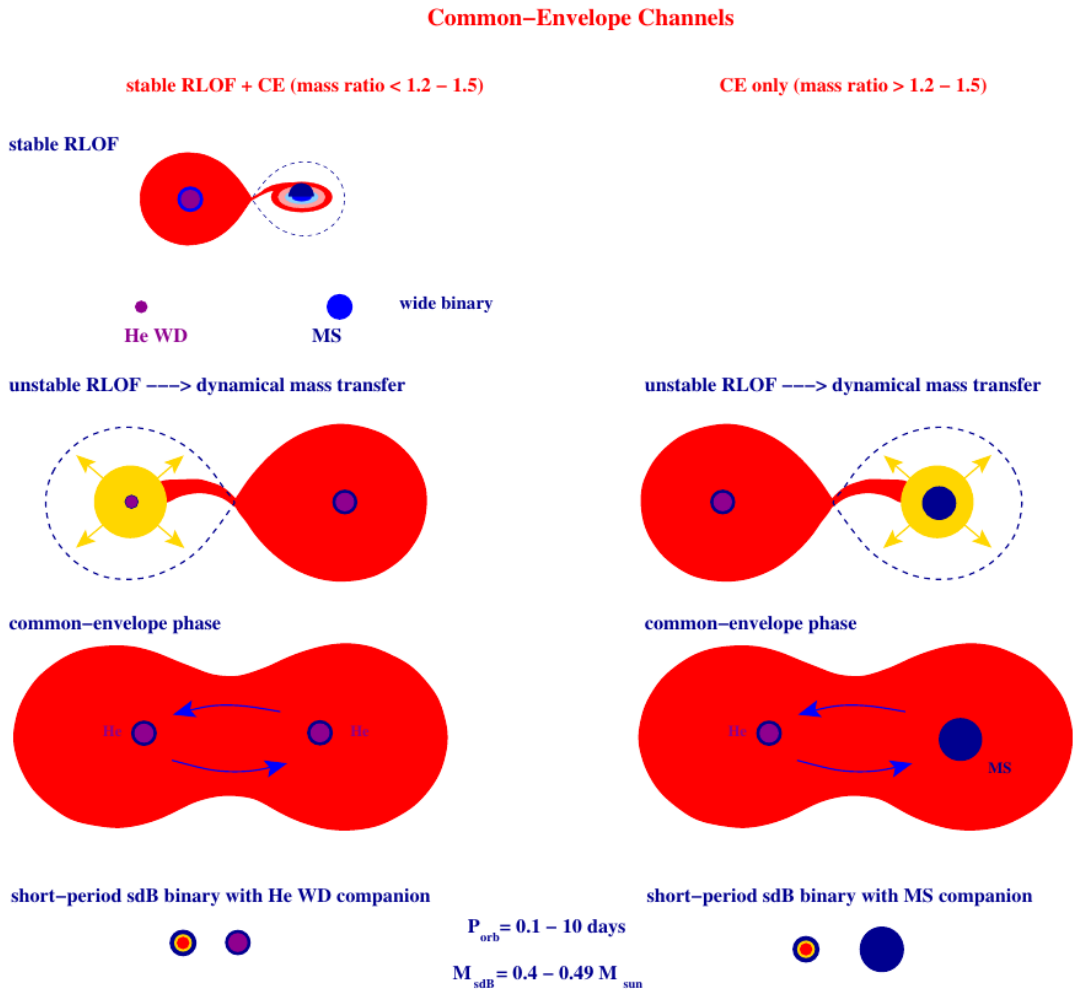
Figure 13: Possible evolutionary tracks for sdBs showing a common-envelope phase. Left side: Evolutionary track with a small mass ratio ($q < 1.2$-1.5). Right side: Common-envelope channel for binary stars with a larger mass ratio ($q > 1.2$-1.5). Both common-envelope channels lead to a close, post common-envelope system with orbital periods between 0.1 and 10 days (Podsiadlowski et al., 2008).

were found to be about $0.7 \cdot 10^{-2} yr^{-1}$ for sdB stars with a main sequence star as companion and $0.4 \cdot 10^{-2} yr^{-1}$ for sdBs with WD companion, respectively.

If both stars have quite similar masses, so that their mass ratio lies below 1.2-1.5, and if the red giant fills its Roche lobe briefly before reaching the tip of the RGB, then the giant will lose most of its hydrogen-rich envelope by stable RLOF remaining a degenerated helium core (see Fig. 14) which may be massive enough to ignite core-helium burning. In contrast to the previously discussed common-envelope channels, just a stable mass transfer occurs which won't lead to a common-envelope and a spiral-in phase. Consequently, sdB binaries, that have evolved by stable RLOF, tend to widen showing orbital periods about 10 to 500 days. Newer model calculations by Chen et al. (2013) exhibit that also larger orbital periods of sdB binaries are possible by the stable RLOF channel. All in all, the stable RLOF produces wide sdB binaries consisting of a hot subdwarf usually with a mass between 0.3 and 0.49 solar masses and a main-sequence star as companion.
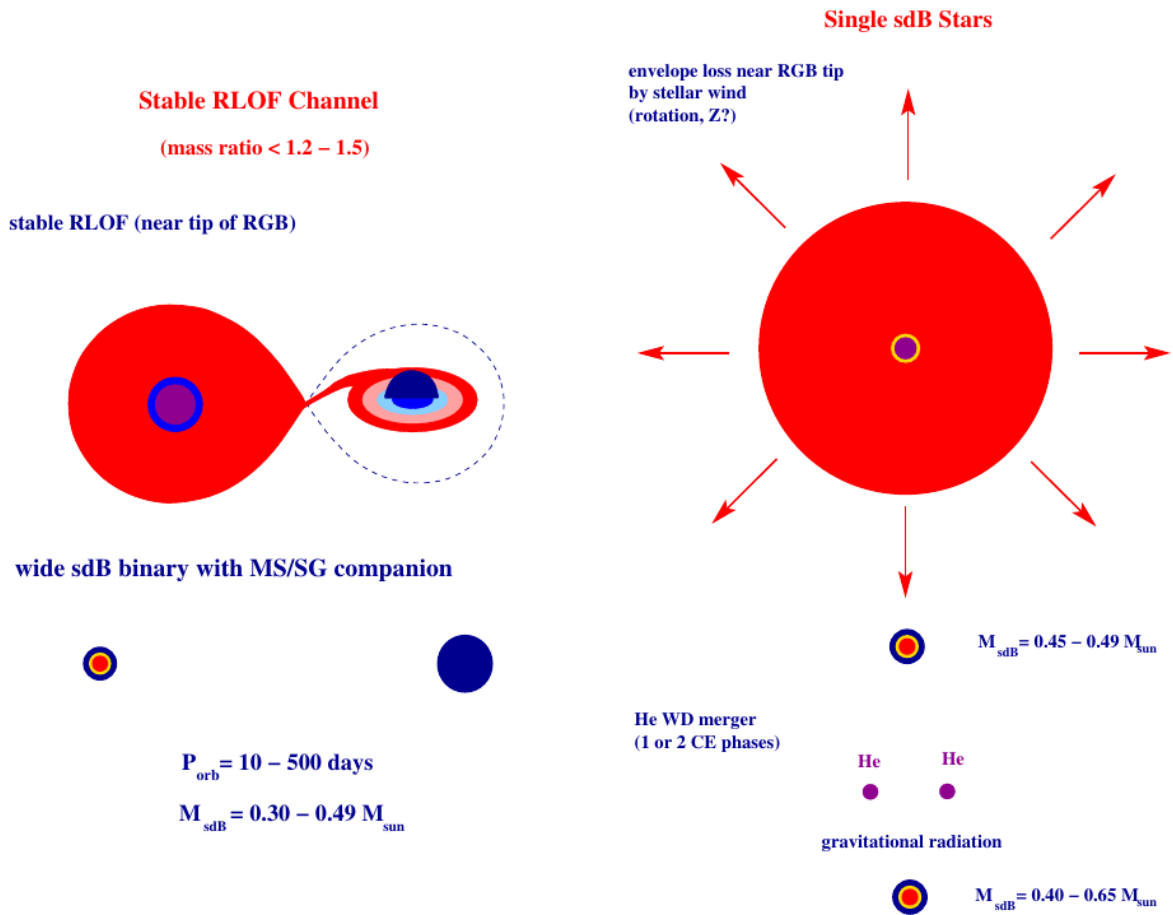
Figure 14: Further formation channels for sdB stars. Left panel: Stable RLOF channel leading to a wide binary which consists of an sdB and a main sequence star. On the right side, possible evolutionary tracks yielding single hot subdwarfs are shown. Upper panel: Envelope loss of a red giant near the RGB tip due to stellar winds. Lower panel: Merger scenario for two helium white dwarfs (Podsiadlowski et al., 2008).

So far, the binary channels were discussed, in the following, we shift our attention to the sce-

narios producing single sdB stars. Two different scenarios exist which will be shortly presented below.

The first is called the merger channel. In this formation, two helium white dwarfs are orbiting their common centre of mass in a very short period ($P \lesssim 8$ hrs). Due to gravitational waves radiation, the system loses angular momentum and energy and, hence, the orbital periods as the stars' separation are getting closer, until the lighter (and larger) WD fills its Roche lobe. Then, the lighter star gets dynamically disrupted. Consequently, its remnant matter is almost fully accreted by the more massive WD. If the surviving white dwarf will reach a certain mass, helium burning ignites in its core and the white dwarf turns into a single sdB (see lower panel on the right side of Fig. 14). Hot subdwarfs, which were produced via the merger channel show a broad mass distribution ranging from 0.4-0.65$M_{\odot}$. The birthrate of sdBs from the merger scenario is comparable to that from the common-envelope channels. The best-fit models of Han et al. (2003) gives 0.8-1.6 $\cdot 10^{-2} yr^{-1}$.

Beside this, further merger scenarios are presumed to produce hot subdwarfs, e.g. the merger of a brown dwarf with the core of red giant (Politano et al., 2008). There are also models suggesting that an sdB star may have evolved from an isolated star. In this case, the star has to lose much matter of its hydrogen-rich envelope on the red giant branch (maybe because of fast rotation) or during the helium flash, whereby core helium-burning ignites and a strong stellar wind emerges (see upper panel on the right side of Fig. 14). However, no detailed results from these theories exist.

3.2 General properties of hot subdwarfs

As previously discussed, hot subdwarfs are helium-burning cores of red giants that lost most of their hydrogen-rich envelope on the RGB. The remaining rest of the envelope usually shows masses below 0.01 solar masses, which is too small for hydrogen shell-burning (Heber, 1986). The stellar atmospheres are even less massive ($M_{atmo} \approx 10^{-10} M_{\odot}$), but very important for astronomers because stellar spectra originate from the stellar atmospheres. Hence, spectra derive only information about the stellar atmospheres and not about the inner stellar structure. Another consequence is that the few hydrogen on the surface of hot subdwarfs suffice to produce the hydrogen Balmer lines dominating their spectra. Surprisingly, their Balmer lines are even more pronounced as in normal main sequence B-type spectra. Beside the Balmer lines, the spectra of hot subluminous stars normally display He I and/or He II, whereby the latter only occur in the spectra of sdO stars. Depending on the incidence and the strength of the helium lines, astronomers classify hot subdwarfs in the following way:

- **sdB stars:** SdB stars posses strong hydrogen Balmer lines in their spectra. The absorption lines of neutral helium are not very pronounced (see Fig. 17, upper spectrum). Most of the sdB stars are part of this class owning helium-poor atmospheres. Due to their temperatures between 25000 and 35000 K, no He II lines are detectable in their spectra.

- **He-sdB stars:** This class of hot subdwarfs shows strong He I lines in their spectra and also less pronounced Balmer lines.

- **sdO stars:** sdO stars are hotter than sdB stars and, consequently, they posses absorption lines of ionized helium. A sdO star spectrum exhibits strong Balmer and He II lines, but He I lines are usually weak or can't be found in the spectrum at all.

- **He-sdO stars:** Helium rich sdO stars show both, He I and He II lines, but exhibit only very weak hydrogen Balmer lines which can be completely missing in many He-sdO spectra (see Fig. 17, lower spectrum).

- **sdOB stars:** SdOB stars ranges between sdO and sdB stars, especially their effective temperature, but also the appearance of their spectra because sdOB stars show broad hydrogen Balmer lines as well as He I and He II lines. In contrast to most sdOs, the helium lines of the sdOB stars are much weaker.
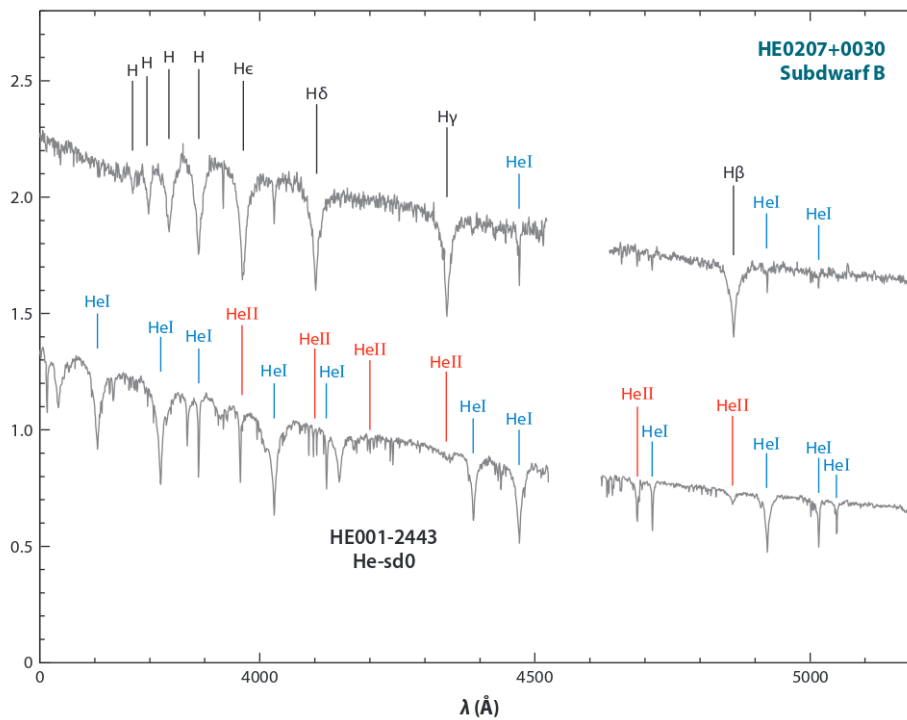
Figure 15: Spectral appearance of two hot subdwarfs plotted against wavelength, where the upper spectrum belongs to a cooler sdB star, while the lower spectrum accompanies to a He-sdO star. In the spectra, the spectral lines of hydrogen (*H*), neutral helium (*He* I), and ionized helium (He II) are marked (Heber, 2009).

Due to this classification, it is obvious that hot subdwarfs' spectra may differ largely as illustrated in Fig. 17.

The classification of hundreds of hot subdwarf stars started in the 1980s, whereby astronomers identified several differences, but also similarities between the various subclasses. Quantitative spectroscopic analyses of the different subdwarf types revealed that each of the three main

classes have their specific, but partly overlapping ranges of effective temperature and surface gravity. The effective temperature of sdB stars was found to lie in-between 25000 and 35000 K, for sdOB the temperature ranges from 30000 to 45000 K, while sdO stars usually posses temperatures between 37000 and 47000 K, but also much hotter sdOs are reported. In contrast to the prominent differences for the effective temperatures, the intervals for the usual surface gravities overlap distinctly. SdB stars usually show surface gravities ranging between $log(g) = 5.0 - 5.7$, sdOB stars gravity is located between 5.0 and 6.3, and sdO stars exhibit values between 5.3 and 5.9 (in cgs-units). For most stars, the surface gravity tends to increase with rising effective temperature, because surface gravity and temperature are correlated ($g \propto T_{\rm eff}^4$) (Heber, 1986).

Large variations were detected for the helium abundances in the subdwarfs' atmospheres. While the helium abundance, usually stated logarithmic, lies for sdB stars in the range of 0.1 to 2.5%, the helium abundance of sdOB stars exhibits a much larger interval ranging from 0.07 to 6% (Heber, 1986). On the other hand, sdO stars can show much larger helium abundances, such as some sdOs in the GALEX sample with helium abundances of $\frac{n_{He}}{n_H} = 1000$ (Heber, 2016).

3.3 HW Vir and reflection effect systems

A very special kind of close binaries is called HW Vir systems consisting of an sdB and an M-dwarf or a brown dwarf (BD) - a celestial object, that has not enough mass to ignite the hydrogen burning. Furthermore, HW Vir stars are eclipsing and single-lined spectroscopic binaries since the companion is much fainter than the hot subdwarf. HW Vir systems, named to the first system found showing this properties, are produced by a common-envelope phase of the progenitor stars which forms the sdB star. Because the HW Vir show periodic radial velocity as well as light variations, they are perfect candidates for mass determinations of sdB stars. Beside this, this kind of binary systems received some attention when astronomers found exoplanets orbiting around the common centre of mass of HW Virginis (Heber, 2009). Currently, 20 HW Vir systems are known (Wolz et al., 2018).

Reflection effect systems consists, as HW Vir systems, of an sdB and a much fainter late main-sequence star or an substellar object. But, in contrast to HW Vir stars, reflection effect systems are not eclipsing just showing a prominent reflection effect. Consequently, the inclination of the system can't be determined that precisely as for HW Vir stars resulting in much higher uncertainties for masses, radii and separation of the stars.

4 Observational programs

Many surveys are monitoring the Sky in search for variable objects. Those projects are of great importance in order to detect new HW Vir stars. For this thesis, three different surveys are of particular significance which is why they shall be shortly presented below.

4.1 SDSS and MUCHFUSS

The Sloan Digital Sky Survey (SDSS) program is a collaboration between several institutions from the United States, Germany, Japan and South Korea aiming a precise and large-scale observation of the northern hemisphere. To reach this aim, almost a decade of planning was necessary. In 2000, the SDSS program started after construction works on the 2.5 m Sloan Foundation wide-field telescope, which is located in the Sacramento mountains near Sunspot, New Mexico, where finished. For the observations of the celestial objects, SDSS uses several sophisticated spectrographs and imagers. Originally, SDSS was focused on the analysis of brightness, position and distance of faraway galaxies and quasars so that more than one million galaxies could be detected until today. If one is checking so many objects, not only galaxies and quasars but also many other celestial objects such as close binaries were detected. It appeared, that spectra and photometric data, which were taken with a high-resolution camera including 30 CCDs and five different bandpass filters, are well suited to study asteroids. Beside this, a huge number of brown dwarfs, dwarf galaxies, and gravitational lenses could be detected with the help of the SDSS program, moreover some hyper-velocity stars and three HW Vir systems. Because the SDSS group can't analyze all of the recorded data, there is a huge data release every year. Actually, the fourth phase of SDSS is running.[4]

The Massive Unseen Companions to Hot Faint Underluminous Subdwarfs from SDSS project or shortly called the MUCHFUSS project aimed the analysis of binaries consisting of a hot subdwarf and a companion owning a mass of more than one solar masses ($M_{comp} > 1M_\odot$) (see e.g. Geier et al., 2015). Due to this high mass, only white dwarfs, neutron stars (NS) or black holes come therefor into question. The existence of such binaries is predicted by evolutionary theories, but are quite rare. For the target selection, spectra from the 6th and the 7th data release of SDDS were used. The astronomers searched in the data base for spectra showing the typical colors and absorption lines of hot subdwarfs. Furthermore, they checked if the stars show radial velocity variations whereby only stars with huge variations were selected (Geier et al., 2011a). So far, the MUCHFUSS project could find more than 1900 hot subdwarfs in the data of SDSS, where 110 stars show RV variability (Geier et al., 2015).

Due to this preselection of potential candidates, one will find not only systems consisting of an sdB star and a massive secondary, but also very close binaries with low mass companions such as HW Vir systems. So far, three HW Vir systems were found by the MUCHFUSS project, one of them has a brown dwarf as companion.

---

[4]More and detailed information can be found on the following webpage: `http://www.sdss.org/`

4.2 OGLE and EREBOS

The Optical Gravitational Lensing Experiment (OGLE), is a long-term photometric Sky survey, which is now in its fourth phase since its establishments in the early 1990s. The first phase, called OGLE-I, took place in the years 1992-1995 using the 1.0 m Swope telescope (Udalski et al., 2015). Since this phase was quite successful - OGLE-I was one the first large scale variability surveys -, OGLE was continued and optimized. For the second phase, called OGLE-II, a new 1.3 m telescope, which is used for all further observations, was built at the Las Campanas Observatory. OGLE-II increased the number of known detected microlensing phenomena rapidly. At the end of the second phase, the astronomers started the next major instrumental upgrade. This time, the camera was significantly improved - a specifically designed wide-field multichip camera was deployed on OGLE-III. Hence, the photometric data derived by OGLE-III are very precise allowing the first discoveries of extrasolar planets and many variable stars. Today, the OGLE-III sample is one of the largest samples of variable stars, amongst them were also some HW Vir stars.

With the help of the data from the OGLE project, Pietrukowicz et al. (2013) and Soszyński et al. (2015) found 36 new HW Vir candidates due to their blue color and their typical light curve shape. Although not all of the candidates will be HW Vir type in the end, this will remarkably increase the number of known HW Vir systems. Lately, Soszyński et al. (2016) has published a catalogue comprising 450000 eclipsing binaries in the Galactic bulge. To check this large sample for further HW Vir candidates, some astronomers analyzed the catalogue of Soszyński et al. (2016) in detail. First, they searched for systems in the sample that show orbital periods less than one day and made a colour cut $V - I < 1$mag. Hereby, they identified 55 further HW Vir candidates. These 55 and the previously found 36 candidates were used to train a machine-learning algorithm which could then identify another 20 systems. All in all, 111 HW Vir candidates were found. For their spectroscopic and photometric analysis, the EREBOS (Eclipsing Reflection Effect Binaries from the OGLE survey) project was initiated. Hence, the EREBOS project aims at recording and analysing time-series spectra of the sample, and photometric follow-up observations to derive the atmospheric and orbital parameters (Schaffenroth et al., 2017).

4.3 Catalina Sky Survey

The Catalina Sky Survey (CSS) is a NASA funded projected aimed at the detection and tracking of near-Earth objects (NEOs), which are larger than 140 meters, because some of them could pose an impact threat to Earth. Therefor, they use three different telescopes in the Santa Catalina mountains which are part of the Steward Observatory, were each of them can cover a specific field on Sky[5]. Because the CSS astronomers are covering a wide field in the Sky to detect NEOs, they are mostly recording other celestial objects photometrically. Currently, the photometric observations of two data releases are available on open access.

---

[5]`https://catalina.lpl.arizona.edu/`; Last access on: 24.02.18

5 Analysis of sdB binaries with cool companions

The previous chapters provided us a theoretical input for the analysis of several HW Vir and reflection effect systems performed in this chapter. The spectroscopic and photometric analysis and my chosen procedure form the essence of this chapter. Firstly, the analysis methods and programs, which are used, will be described, before observation and data analysis of the seven binary star systems will be elucidated in detail.

5.1 Methods and used programs

In chapter 2, four different methods were presented with which astronomers are able to observe and analyze binary stars. Two of the four methods are of high importance for this work: the spectroscopic and the photometric analysis. As previously discussed, the combination of the both analysis methods may provide information about the binary stars' masses and radii.

5.1.1 Light curve analysis and MORO

At first, we consider the light curve analysis. As we have seen in Section 2.2, the Roche model provides the basis for the photometric analysis from which a synthetic light curve can be calculated and fitted to the measured data in order to determine the parameters by χ^2-minimization techniques. The parameters of the best-fit model are assumed to agree with the real parameters of the system examined. To calculate a synthetic light curve, one has to set start values for all the parameters, with which beginning the light curve modeling program tries to determine the parameters according to the best-fit model by using the χ^2-minimization. A suitable method for the calculation of synthetic light curves is the procedure of Robert Wilson and Edward Devinney. Their model introduces $12 + 5n$ parameters (see Table 1), where n is the number of light curves recorded in different pass-bands which were then fitted simultaneously. If the WD method is used, the monochromatic flux of both stars is summed up at each phase (Wilson & Devinney, 1971).

Table 1: List of the parameters used by the Wilson-Devinney method.

Physical symbol	Parameter's name
i	Inclination
$g_{1,2}$	Graviational darkening exponents
$T_{1,2}$	Effective temperatures of both stars
$A_{1,2}$	Bolometric albedos
$\Omega_{1,2}$	Roche potentials
$q = \frac{M_2}{M_1}$	Mass ratio with $M_1 \geq M_2$

Table 1: (Continuation)

$\delta_{1,2}$	Radiation pressure parameters
$L_{1,2}$	Luminosities
$x_{1,2}$	Limb darkening coefficients
l_3	Fraction of third light

For the light curve analysis, several physical effects have to be considered some of which have already been described in the Sect. 2.1.4:

- **Limb darkening:** As previously discussed, limb darkening occurs due to the change of column density and optical depth of the stars with the distance to their centre. Consequently, the stars' discs seem to be darker and fainter at the limb than at the centre. The intensity is given by $I(cos(\theta)) = I(1) \cdot x(1 - cos(\theta))$, where $I(1)$ is the intensity at the centre of the stellar disc and x the limb darkening coefficient (Wade & Rucinski, 1985).

- **Reflection effect:** The reflection effect is very strong for close binaries consisting of a hot primary and a much cooler companion such as the post common-envelope sdB binaries discribed in this thesis. The hotter star heats up the hemisphere of the secondary which is causing a brightening of this hemisphere according to Stefan-Boltzmann law. Consequently, this is resulting in a periodical sinusoidal flux variation because the visible part of the heated side changes with the phase (see Sect. 2.1.4).
  Using the Wilson-Devinney method for light curve analysis, the reflection effect is considered in a very simple way: the effect is assumed to be the reflection of the incoming flux whereby the strength of the reflected flux finds its expression in the bolometric albedos A. The change of the secondary's effective temperature caused by the reflection effect is given by: $T_{\mathrm{refl}} = T_2 \cdot (\frac{A_2 F_1}{F_2})^{\frac{1}{4}}$ where $F_{1,2}$ are the fluxes of the stars and A_2 is the albedo of the secondary (Schaffenroth, 2015).

- **Radiation pressure:** In very close binary systems, the hot, luminous star puts a non-negligible radiation pressure on the cooler secondary which may cause deformations of the companion's shape. The radiation pressure is represented by the momentum $p = \frac{h\nu}{c}$ of the photons emitted from the primary and then absorbed in the companion's atmosphere. For a detailed description of the absorption process, one has to take many physical and chemical effects into account (see e.g. Drechsel et al., 1995). The radiation pressure parameter δ is approximately given - without considering the flux vector - by: $\delta = \frac{F_{press}}{F_G} = \frac{kL}{4\pi cGM}$, with k the mass absorption coefficient.
  To calculate the synthetic light curve, the shape of the two components is firstly determined with the help of the Roche model and then modified under consideration of the radiation pressures of the system.

- **Gravity darkening:** Because stars in close binaries may be fast rotating (due to bound rotation), their effective gravities become smaller at their equator while gravity is increasing at the poles (see Sect. 2.1.4). Surface temperature and gravity are correlated, hence, temperature shows the some behavior. According to Stefan-Boltzmann law, the equator region appears darker and the emitted flux is smaller than at the poles: $F(P) = F_{pole}(\frac{g(P)}{g_{pole}})^g$, where $g(P)$ is the gravity at a point P and g the gravity darkening exponent. If the envelope of a star is completely radiative, then the gravity darkening exponent can be set to 1 according to von Zeipel (1924), but if convection dominates the envelope, then g is approximately given by $g \approx 0.33$ in accordance to Lucy (1967).

The Wilson-Devinney method is very important for light curve analysis because it includes several modes, so that various system configurations can be modeled. In this work, only the second mode was used which is for detached and semi-detached systems. Furthermore, the second WD mode connects the companions' luminosity to its temperature using the Planck function, while all the other parameters are not restricted.

Many programs implementing the Wilson-Devinney code exist which allow the modeling of synthetic light curves. One of them is the MOdified ROche model-based light curve analysis program MORO, which was developed at the Dr. Karl Remeis Observatory in Bamberg by Drechsel et al. (1995) and is utilized in this work. MORO uses an alternative Roche-model considering the radiation pressure during the modeling process of the synthetic light curve, a case, which makes it possible to analyze also young, massive stars (Drechsel et al., 1995). MOROs fit process, in which the synthetic light curve is adjusted to the shape of the measured light curve, is based on a classical χ^2-minimization applying the simplex algorithm - a special algorithm developed by Kallrath & Linnell (1987). The simplex algorithm defines a set of $m+1$ start parameter sets where m is the quantity of the start parameters. All start parameters can be set by the user. For every set of parameters, a synthetic light curve is generated, then compared to the measured data and adjusted. The adjusting works as follows: For every light curve point P the residual d_v between the measured and the calculated light curves is determined ($d_v = l_{meas} - l_{calc}$). With their help, the standard deviation - in this case an indicator for the quality of the fit - can be calculated by:

$$\sigma_{fit}(x) = \sqrt{\frac{n}{n-m} \frac{1}{\sum_{v=1}^{n} \omega_v} \sum_{v=1}^{n} \omega_v d_v^2(x)} \tag{10}$$

with n the number of measured data points, m the quantity of start parameters for the simplex algorithm, and ω_v the weighting of the single data points. The parameter set with the largest standard deviation σ_{fit} is discarded and then replaced by a new parameter set, which MORO finds by using fixed operations. This step will be repeated until a convergence criterion is fulfilled or the maximimum number of iterations was reached. Usually, this method works very well and reaches a minimum in any case. But the minimum does not have to be the global minimum, especially if the start parameters are badly chosen (Schaffenroth, 2015).

Huge differences exists between the parameters' effects on the light curves: while changing the inclination i and mass ratio q largely affect to the shape of the light curve, however, others like the effective temperature of the secondary have a negligible effect in an sdB+dM binary system. Furthermore, some parameters, that are used for the light curve analysis, are strongly correlated, especially the mass ratio and radii of the stars. This may cause some problems, for example if too many and inadequate combinations of parameters are fitted simultaneously. For this reason, as many parameters as possible should be fixed at values established by theoretical models or known from spectroscopy. For example the range of the mass ratio can be restricted by using the radial velocity curve and the primary's effective temperature, which is determined by a quantitative spectral analysis. Then, every single value of this range can be used once and is fixed while all other parameters are varied. On this way, a large number of fits has to be performed for all mass ratios to ensure that the global minimum will be found. In the end, the σ_{fit} value of every single fit is calculated and compared. The fit with the lowest value of σ_{fit} is adopted to be the best solution (Schaffenroth, 2015).

5.1.2 Spectral analysis and SPAS

To determine the masses and the radii of the two binary stars, another method is needed: the time-resolved quantitative spectral analysis (see section 2.1.3). As usual for close systems with huge brightness differences, sdB binaries and, especially all the HW Vir systems are single-lined binaries. Using time-resolved spectroscopy, astronomers can derive the RV curve of the hotter star by fitting a sinusoidal function to the phased RV points as well as the semiamplitude K_1 which is very important for the calculation of the mass ratio.

Beside this, the atmospheric parameters of the star, namely the effective temperature, the surface gravity, and the helium abundance, can be determined with the help of the quantitative spectral analysis. To derive these three parameters, model atmospheres and synthetic spectra are required. The three parameters are derived by interpolating them in a solid grid of precomputed, synthetic spectra with the help of a two times continuously differentiable, cubic polygonal chain (Press et al., 1986). Such an analysis program is the Spectrum Plotting and Analysis Suite developed by Heiko Hirsch which bases on the FITSB2 program designed by Napiwotzki et al. (2004), but has a simplified user interface and can include the rotation of a star to its analysis (Hirsch, 2009). The fit of the parameters works nearly similar at both programs: The Downhill-Simplex algorithm is used in which a test function determines the goodness of every vertex of the simplex and replaces the one with the lowest goodness. This algorithm continues the replacing until the relative difference of the test function falls below a threshold or the predefined maximal number of iteration has been performed. SPAS is using a χ^2-function as test function yielding a probability distribution of the parameters (Hirsch, 2009).

The radial velocities are derived by fitting a combination of Gaussian, Lorentzian and polynomial functions to the line profile of the absorption lines of the spectrum which have to be selected by the program user (Hirsch, 2009).

In the following, the usual procedure for the analysis of the atmospheric parameters shall be

explained:

- **Effective temperature:** The effective temperature of a star is determined by matching the strength and the depth of the absorption lines. The temperature is decisive for the thermal excitation of the elements and, hence, the shape of every absorption line depends on the star's temperature. Elements, that show several ionization stages simultaneously (such as helium or silicon), are well adapted for a precise determination. Since the spectra, used in this work, are of low resolution, and sdB stars are not hot enough to ionize helium, the hydrogen Balmer lines were used to determine the effective temperature. The depth and the shape of the Balmer lines is increasing with the temperature and reaches its maximum for A0 stars. At higher temperatures, hydrogen is ionized which is why stars of earlier classes show shallower hydrogen lines in their spectra.

- **Surface gravity:** As all absorption lines are influenced by the stars' temperature, they are also influenced by the surface gravity because local pressure and gas density are correlated with the surface gravity. Hence, if the surface gravity increases, the plasma density does too so that the probability for electron captures of ions increases, while the ionization degree of the plasma decreases. Consequently, elements with different ionization stages are well adapted for a precise analysis of $log(g)$. As discussed for the effective temperature, we do not find different ionization stages of any element in low resolution sdB spectra which is why we have to use the hydrogen Balmer lines for the determination of $log(g)$. While the centre of the Balmer lines are important for the analysis of the temperature, the wings are crucial for the surface gravity. They proved to be very sensitive for surface gravity's changes, because they are broadened by the linear Stark-effect (Schaffenroth, 2015).

- **Helium abundance:** To derive the helium abundance of a star, two different possibilities exist and are chosen depending on the temperature of the investigated star.
  The first is checking the shape and depth of the helium lines and works well at high temperatures because then helium lines are visible in the spectra and their shape and depth give some indication of the helium abundance. But it has to be considered that the coherence between the depth of the helium lines and the helium abundance in the stellar atmosphere is non-linear (curve of growth). Instead, the coherence can be described by a continuous, strictly monotonically increasing function which has three different areas of varyingly strong increase. For weak helium lines in the spectra, the coherence is approximately linear, for stronger lines the curve becomes shallower because saturation occur. If the lines are very strong and deep, then they develop damping wings resulting to a renewed increase of the equivalent width (Schaffenroth, 2015).
  If the star is cooler ($T_{\text{eff}} \lesssim 10000$K), the helium lines are not visible in the spectra. Here, one may use the hydrogen Balmer lines again. The larger the helium abundance in the stellar atmosphere, the higher is the photospheric pressure. The higher gas pressure

causes then a quenching of the higher-order Balmer lines, so that they become shallower (Liebert & Wehrse, 1983). However, spectra of very high resolution are needed.

5.2 Observation and data reduction

5.2.1 Spectroscopy

In the following, we consider the spectra and light curves of seven systems, namely OGLE 173411, OGLE 361688, OGLE 416194, EC 20323-4648, Pn23l1-18, PG 2259+134, and MCT 0049-3059. The spectra of the three OGLE systems, EC 20323-4648, MCT 0049-3059, and some spectra of PG 2259+134 were recorded at the 3.6 m New Technology Telescope (NTT), which is part of the La Silla Paranal Observatory of the European Southern Observatory (ESO) located in the Atacama desert in Chile. The other spectra were recorded at the 2.5 m Isaac Newton Telescope (INT) of the Observatorio del Roque de los Muchachos at La Palma, Spain.

The La Silla spectra originated in the nights of the 1st to the 4th of July 2017, the LaPalma
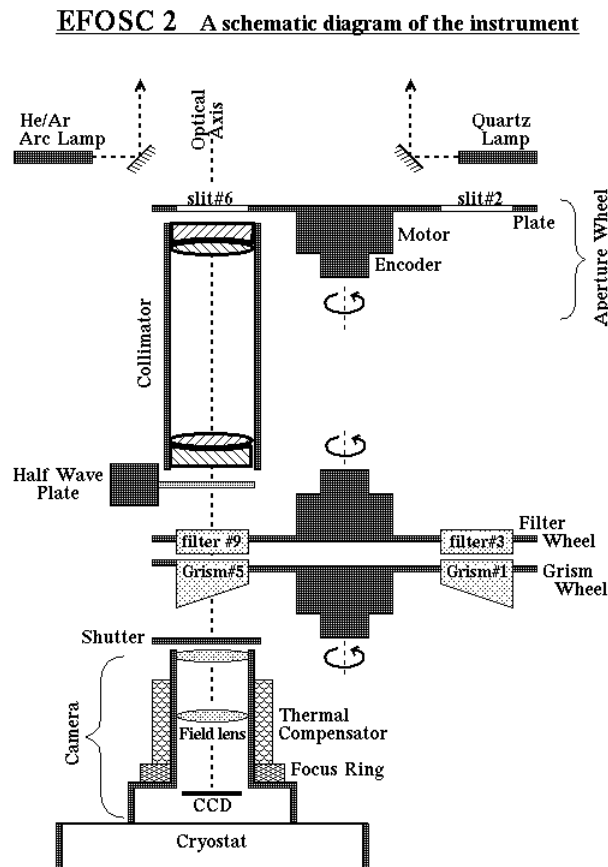

Figure 16: Structure of the EFOSC2 multi-mode instrument. In the long slit spectrograph mode, the filters are not used.[6]

spectra are recorded between the 22nd and the 25th of September, 2016. Firstly, the circumstances at La Silla shall be described. The EFOSC2 long slit spectrograph was connected to the NTT telescope to record the spectra of the sdB binaries. After light is collimated in the focal plane of the NTT telescope, it passes a slit and enters the EFOSC2 spectrograph. Thereby, the observer can select one of ten different slits with various widths by using the slit wheel (see Fig.16). Afterwards, a lens collimates the light before the beam reaches the grism. The observer can select from several grisms. The grisms differ in dispersion, resolution, blaze angle, grating, and, consequently, in the optical range, that can be observed. For the spectra, that are analyzed in this work, two different grisms are deployed: grism 7 and grism 19. Grism 7 has a dispersion of $0.96 \frac{\text{Å}}{pixel}$, an optical range of $3270 - 5240$ Å, and a spectral resolution element of FWHM$= 7.4$ Å. Hence, the resolution of the spectra taken with grism 7 is $R = \frac{\lambda}{FWHM} \approx 570$ at 4500Å. Grism 19 has a smaller optical range ($4441 - 5114$Å), a distinctly smaller FWHM of about 1.5 Å, and a lower dispersion ($0.55 \frac{\text{Å}}{pixel}$). Since the FWHM is much smaller than for the grism 7, the resolution of the spectra, that were taken under the usage of grism 19, have a significantly higher resolution: $R \approx 3000$ at $\lambda = 4500$ Å[7]. For the wavelength calibration, a HeAr-lamp was used.

The spectra taken at LaPalma were recorded by using the Intermediate Dispersion Spectrograph (IDS). IDS is a long-slit spectrograph and equipped with a 235 mm focal length camera offering two 4096x2048 pixel CCD detectors. While the RED+2 CCD chip is sensitive in the red, the EEV10 chip has its highest sensitivity in the blue optical range. Because most of the hydrogen Balmer lines are positioned in the blue part of the optical range, the EEV10 CCD was used for our observations. Moreover, the IDS spectrograph offers 16 different gratings to the observer[8], whereby for the sdB spectra, that were pertinent for this work, only the R400V grating was used. The Blaze angle of the R400V grating shows the highest efficiency for light with the wavelength of 5100 Å.[9] For the wavelength calibration, a CuAr-lamp was deployed.

While the IDS spectra were reduced and calibrated by Stephan Geier with the help of the Munich Image Data Analysis System (MIDAS), a program package developed by the European Southern Observatory (ESO), we obtained the raw spectra of the systems that were recorded at La Silla. Hence, these spectra had to be reduced and calibrated by the author. The steps, that are needed to reduce and calibrate a spectrum, are slightly varying depending on the construction of the spectrograph. But the main concepts of each step, which shall be presented in the following, are always the same.

- **Removal of cosmics:** Cosmic particles of high energy may cause unwanted signals at the positions where they hit the CCD chip. Usually, their occurrence is restricted to single pixels and the signal is much stronger than that of photons. Hence, the cosmics

---

[7]`https://www.eso.org/sci/facilities/lasilla/instruments/efosc/inst/Efosc2Grisms.html`; last access on: 02.03.18

[8]see also: `http://www.ing.iac.es/astronomy/instruments/ids/`; last access on: 03.03.18

[9]`http://www.ing.iac.es/astronomy/instruments/ids/idsgrat_tables.html`; last access on: 03.03.18

can be easily identified and their signal can be removed by interpolating the signal of the neighbored pixels.

- **Subtraction of the bias frame:** The recording of a bias frame is needed because of the functionality of a CCD, which operates similarly to a photodiode, whereby photons generate free electrons and holes in the depletion region of the semiconductor material according to the inner photoelectric effect. The crucial difference between the CCD and the diode is that the emerged charges can't drain off in a CCD, but rather are collected in a potential well caused by a voltage gradient. One potential well corresponds to one pixel. To determine the charges collected per pixel, they have to be shifted step-by-step to the readout device, successively read out, and converted to a digital signal. Since this readout technique can only gather positive values of voltage and negative values may occur due to noise, a constant offset is automatically added, which has to be subtracted again after the readout. The signal strength of the offset can be detected with the help of an image, which has to be taken with closed shutter and zero exposure time, the so-called bias frame. Usually, several bias frames were recorded, averaged to reduce the noise, and then subtracted from all scientific measurements.

- **Removal of the dark current:** If the exposure time is increased compared to the bias frame, effects caused by the thermal excitation, which are called the dark current, can be detected too. Because dark frames quantify the offset as well as the dark current, the dark current can be subtracted from the data instead of the bias frame. However, modern CCDs show so lowly dark currents, that the effects of thermal excitation becomes negligible and a bias correction is sufficient.

- **Flatfield correction:** Very important is the flat-fielding of the spectra. A flatfield is a spectrum of a source (usually a halogen-lamp), which has a continuous spectrum and is emitting light as independent of the wavelength as possible. Because the flatfield lamp is uniformly illuminating the spectrograph, every pixel of the CCD should measure the same intensity. In reality, this won't pertain, because some pixel exhibit lower sensitivity or are damaged. Hence, the flatfield shows the deficiencies of the CCD. By dividing the scientific spectra through the flatfield, these effects can be removed. As previously done for the bias frame, several flatfields were taken and averaged. The averaged flatfield, usually called masterflat, is then adapted to the scientific spectra.

- **Wavelength calibration:** The application of the steps, discussed so far, yields to a spectrum showing the star's intensity per pixel. But, to derive any information about the spectrum, the intensity per wavelength is needed. This dispersion relation is derived from a reference spectrum of a gas-discharged lamp showing very narrow emission lines whose central wavelengths are well known. The reference spectrum is recorded with the same spectrograph. If MIDAS is used for the reduction and calibration, some emission lines have to be manually identified. On the basis of this identification, MIDAS calculates the

dispersion relation using a low order polynomial function. In this way, the pixel position of an emission line is mapped to the wavelength space using a catalogue of laboratory wavelength. Normally, the dispersion relation is calculated with a cubic function.

- **Rebinning:** With the help of a cross dispersion cut through the two-dimensional raw data, the central position of the star spectrum in the recording can be detected and extracted from the data resulting to a one-dimensional data set.

Details on the data reduction and calibration are described in the MIDAS user's guide on the ESO web page[10] or in the teacher's thesis of the author (Note: this thesis is written in German.).[11]

5.2.2 Photometry

The light curves of the three OGLE binaries were recorded by using the 1.3 m Warsaw telescope at the Las Campanas Observatory. Because OGLE is a Sky survey, the light curves of the three stars were not taken in one night, but rather recordings were repeatedly taken over a number of years. In contrast to other Sky surveys, OGLE is using bandpass filters resembling the standard BVI filters. For the three binaries, which are analyzed in the following, an I-band filter was used reproducing very closely the standard system band (Udalski et al., 2015). Accordingly, the central wavelength of the filter, where the sensitivity of the filter reaches its maximum, was assumed to be $\lambda_{cent} = 8000$ Å. The photometric data were phased and normalized by Veronika Schaffenroth, so that the centre of primary minimum is located at $\Phi = 0$ and, consequently, the centre of the secondary minimum at $\Phi = 0.5$. To normalize the light curves, the flux at a phase of $\Phi = 0.25$ was set to 1. All three systems show a strong reflection effect, a deep primary minimum, and a much weaker second minimum.

For the other stars, photometric observations from the Catalina Sky Survey (CSS) were used to derive the light curve. In contrast to the OGLE survey, CSS does not use any bandpass filters, which is why the sensitivity range of the CCD is crucial. Usual CCD-chips are particularly sensitive in the middle of the optical range. Hence, we estimated the central wavelength to be $\lambda_{cent} = 5500$ Å. The photometric data of all binaries, that were analyzed here, were recorded by using the 0.7 m Catalina Schmidt telescope and a single $4k$ x $4k$ CCD with 2.5" pixels (Drake et al., 2015). While the light curves of EC 20323-4648 and Pn23l1-18 do show eclipses, the light curves of PG 2259+134 and MCT 0049-3059 do not. However, all four systems exhibit a reflection effect in their light curves. In comparison with the OGLE light curves, the uncertainties of the photometric measurements recorded by CSS are much larger. Since the photometric data of the four systems were derived over one decade and only between 300 and 400 data points were available for the binaries, their ephemerids are not well determined.

---

[10]`https://www.eso.org/sci/software/esomidas//doc/user/98NOV/volb/index.html`; last access on: 11.03.18
[11]`https://www.sternwarte.uni-erlangen.de/docs/theses/2016-07_Wolz.pdf`; last access on: 11.03.18

5.3 MCT 0049-3059

5.3.1 Data reduction and radial velocities

At first, we start with the spectroscopic analysis of the binary system MCT 0049-3059. All spectra of the systems, that are used in this work, were recorded at La Silla with the EFOSC2 spectrograph. Because the observing conditions were suboptimal during the three observing nights (poor seeing, clouds, etc.), the observing schedule could not be kept up, which is why only three spectra of MCT 0049-3059 were recorded. Two of these three spectra were taken with grism 19, the other one with grism 7 offering a larger wavelength range at lower resolution (see Sect. 5.1.). Consequently, the two spectra of higher resolution and smaller wavelength interval are used for the determination of the radial velocities, while the spectrum recorded with the grism 7 was used for the quantitative spectral analysis because it contains much more absorption lines.

However, the spectra had to be reduced and calibrated first. Therefor, we proceeded as follows: Initially, we checked the spectra of the HeAr calibration lamp and tried to identify each emission line in the spectra by comparing them with wavelength-calibrated, high resolution spectra of the IRAF spectral atlas.[12] All emission lines of the HeAr lamp, that were recorded with grism 7 as well as with grism 19, could be identified. After the validation of the calibration spectra, we started the data reduction under the usage of MIDAS. To perform a data reduction with MIDAS, a script was set-up describing all steps that have to be performed by the program. Here, an available script originally developed for the analysis of DBSP spectra (Wolz et al., 2018) was modified to the conditions at La Silla (especially to the spectrograph and the CCD). During the first reduction attempts, it turned out that the coordinate unit, which describes the position of the single pixel on the CCD, was not pixel but rather right ascension and declination. But because pixel values are required for the data reduction with MIDAS, we had to delete the descriptor in the fits-header and subsequently redefined it in the coordinate unit needed. After this change, the data reduction and calibration worked smoothly.

Table 2: Radial velocities of MCT 0049-3059 from NTT EFOSC2 spectra. The RVs were determined by using SPAS. In the last column the absorption lines of each spectrum are listed, that were used for calculating the radial velocities.

BJD	v_{rad} $[\frac{km}{s}]$	Δv_{rad}	used lines
2457937.93284663	-23	11	H_β, He I 4471
2457938.92846426	-5	10	H_β

Now, the determination of the radial velocities of the sdB spectra could be proceeded. Therefor,

---

[12]available at `http://iraf.noao.edu/specatlas/`; last access on: 26.03.18

the analysis program SPAS was used which is explicitly described in Sect. 5.1. Since the optical range of grism 19 is very small (4441 − 5114 Å), only the hydrogen Balmer line H_β and the helium line at 4471 Å could be used. The results as well as the used lines can be found in Table 1. Due to the fact that only two spectra were recorded, which are suitable for the determination of the radial velocities, it is impossible to derive the binary's radial velocity curve. For this reason, we omitted the light curve analysis of MCT 0049-3059 - no useful results would be derived for the components' masses nor radii.

5.3.2 Atmospheric parameters

The only spectrum of this system, that was recorded with grism 7, is used to constrain the atmospheric parameters of the primary star. As previously described, spectra measured with this grism offer a larger spectral range and, hence, more absorption lines can be used for further analysis of the atmospheric parameters. The more spectral lines can be identified in a star's spectrum, the more precise will be the results from quantitative spectral analysis.
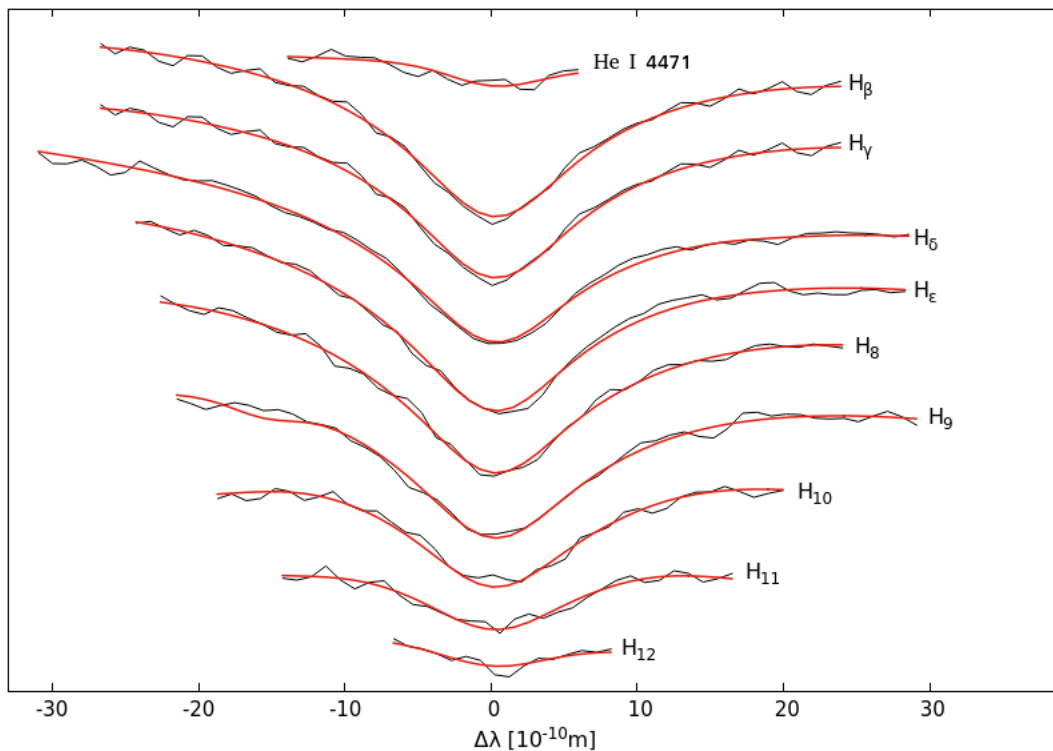
Figure 17: Fit to the absorption lines of the only EFOSC2 spectrum of MCT 0049-3059 taken with grism 7 in order to determine the atmospheric parameters. The synthetic spectra were calculated from LTE model atmospheres (Heber et al., 2000).

Since the wavelength array of the spectra taken with grism 7 ranges from 3270 to 5240 Å, the Balmer lines H_β to H_{12} as the weak He I 4471 Å lines are visible in the spectrum of MCT 0049-3059, as shown in Fig. 17. With the help of SPAS, we obtained the values for the atmospheric parameters that are listed in Table 3. The uncertainties of the values are calculated by SPAS as

well using a bootstrapping method. The values for effective temperature, surface gravity, and helium abundance demonstrate that the primary of MCT 0049-3059 is a helium-poor sdB star.

Table 3: Atmospheric parameters of PG 2259+134. Their values as well as their uncertainties were determined with SPAS using a NTT EFOSC2 spectrum.

BJD	T_{eff} [K]	$\log(g)$ $[\frac{cm}{s^2}]$	$\log(y)$ $[\frac{n_{He}}{n_H}]$
2457937.89323335	28965 ± 190	5.43 ± 0.035	-2.49 ± 0.27

5.4 PG 2259+134 - a reflection system with a companion close to the stellar limit

5.4.1 Radial velocity curve

For this work, 12 spectra of PG 2259+134 were available, whereby one half was recorded at La Silla while the other half was taken with the IDS spectrograph using the INT telescope at La-Palma. The advantage of the IDS spectra is that they can be used for both, determination of the radial velocities and quantitative spectroscopic analysis, since they are offering an unvignetted wavelength range of 3208 Å and a resolution of $R = 1596$ at $\lambda = 4500$ Å.[13] Consequently, a large number of helium and Balmer lines can be found in the IDS spectra taken with the R400V grating. Five of the six spectra, which were recorded with the EFOSC2 spectrograph, were taken with grism 19 so that overall eleven spectra can be used for the determination of the system's radial velocity curve. The spectra of PG 2259+134 show more helium lines than the previously discussed spectra of MCT 0049-3059 so that more lines could be used to determine the radial velocities which are given in Table 4. Beside this information, also the derived radial velocities, their uncertainties, and the observational times are given in this Table. The times as well as the velocities are barycentrically corrected, the velocities and their errors were determined by using SPAS. Because the IDS spectra are of lower resolution than the EFOSC2 spectra, their uncertainties calculated with a bootstrapping method are obviously larger.

Table 4: Radial velocities of PG 2259+134 from INT IDS and NTT EFOSC2 spectra. The RVs were determined by means of SPAS. In the last column the absorption lines of each spectrum are listed, that were used for calculating the radial velocities.

BJD	v_{rad} $[\frac{km}{s}]$	Δv_{rad}	used lines
2457655.56164738	-19	30	H_α-H_δ, He I 4026, He I 4471

---

[13]http://www.ing.iac.es/astronomy/instruments/ids/idsgrat_tables.html; last access on: 27.03.18

Table 4: (continuation)

2457655.56525858	-35	13	H_α-H_ε, He I 4438, He I 4471
2457655.58215668	-60	15	H_α, H_γ-H_ε, He I 4471
2457655.58576778	-41	15	H_α-H_8, He I 4471
2457655.60147378	-71	19	H_α-H_8, He I 4026
2457655.60508488	-85	50	H_α-H_ε, He I 4026, He I 4471
2457936.82095431	-44	14	H_β, He I 4471, He I 4921, He I 5015
2457936.84824382	-20	10	H_β, He I 4471, He I 4713, He I 4921
2457936.89115928	-100	9	H_β, He I 4471, He I 4921
2457936.92113040	-122	9	H_β, He I 4471, He I 4713, He I 4921
2457936.93483891	-109	11	H_β, He I 4471, He I 4921
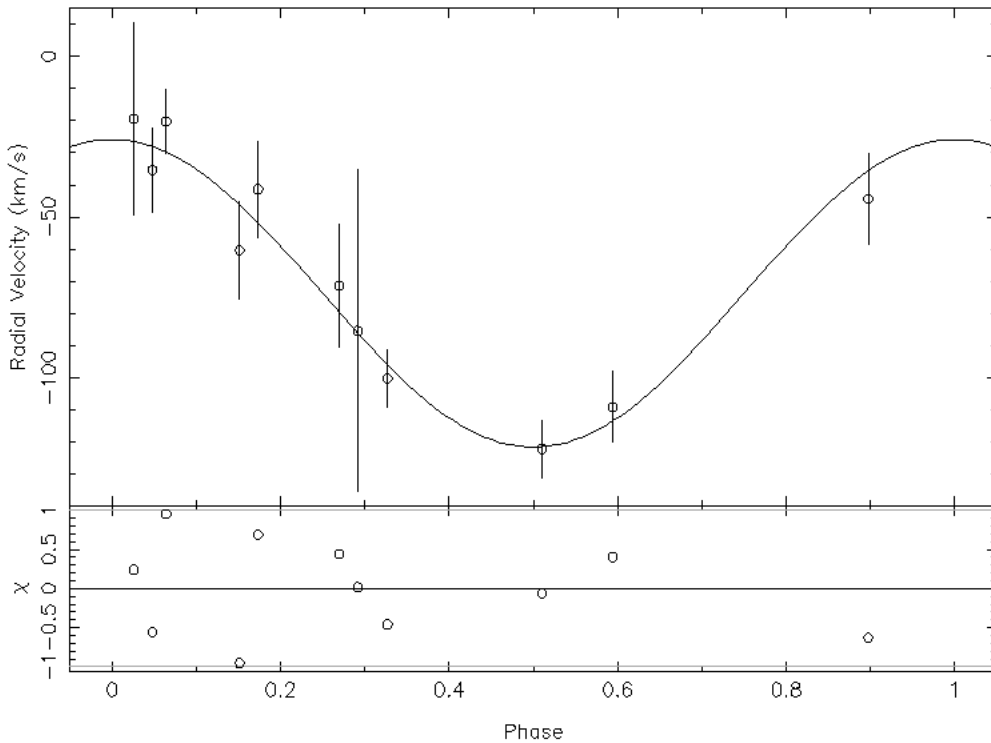
Figure 18: Phased radial velocity curve of PG2259+134 using IDS and EFOSC2 spectra and fitted with a sinusoidal function. The residuals are shown in the bottom panel.

We were able to determine the radial velocity curve of PG 2259+134 because enough spectra are available to derive a precise RV curve. For the analysis of the RV curve, an interactive ISIS script (Interactive Spectral Interpretation System) was used. The period of the system was

known from photometry and, hence, kept fixed. Since the orbital period of the binary is very short ($P = 0.1634401$ d), we assumed the orbit of the two components to be circular. Hence, the eccentricity e was set to zero. To derive the parameters of the radial velocity curve, a sinusoidal function is fitted to the phased radial velocities. We obtained the following results: The semiamplitude was found to be $K_1 = 47.9 \pm 3.4 \frac{km}{s}$, the systemic velocity is $\gamma_1 = -73.8 \pm 3.0 \frac{km}{s}$. As seen in Fig. 18, the fitted sine curve matches perfectly to the measured radial velocities; the curve lies inside the uncertainty of every point. The small value of the semiamplitude appears as very interesting because similar binaries with comparable orbital periods show usually larger values.

5.4.2 Quantitative spectral analysis

One of the six EFOSC2 spectra was taken with the grism 7 so that it can be used for the determination of the atmospheric parameters. As described before, the six IDS spectra can be used too for the quantitative spectroscopic analysis. Fig. 19 shows the fit of the synthetic spectra, which are calculated by using model atmospheres of Heber et al. (2000), to the absorption lines of an individual, measured spectrum of PG 2259+134. Since the IDS spectra are less accu-

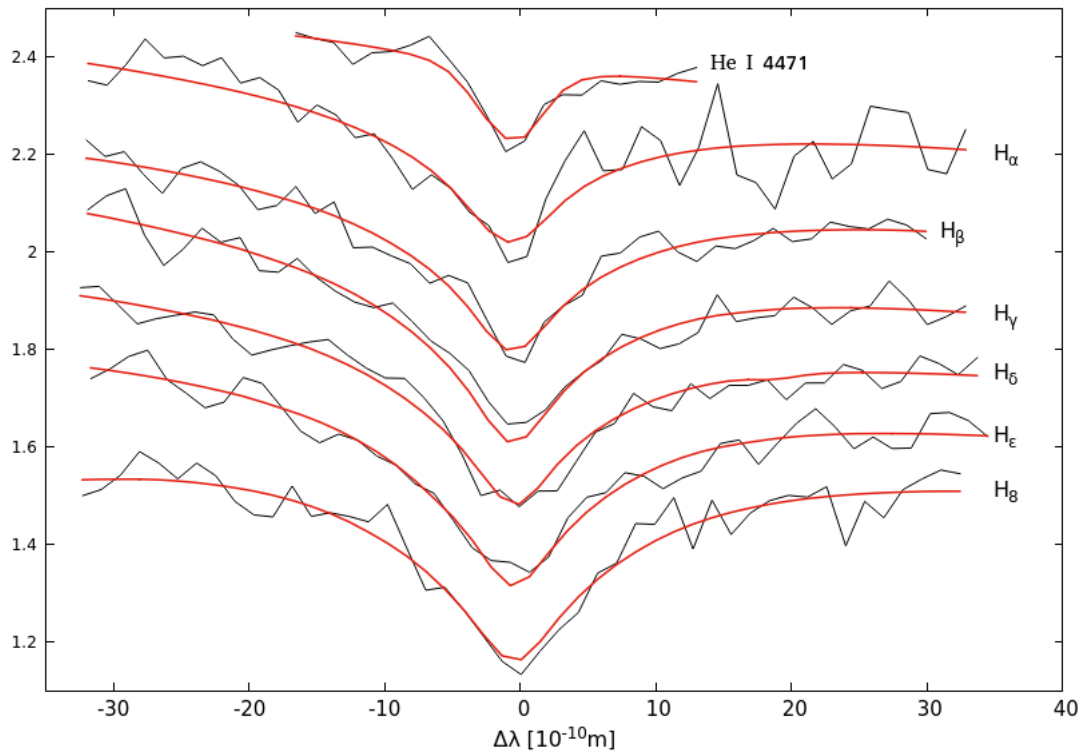Figure 19: Example fit to the absorption lines of an individual IDS spectrum of PG 2259+134 to determine the atmospheric parameters. The synthetic spectra were calculated from LTE model atmospheres (Heber et al., 2000).

rate in the UV, the Balmer lines of higher transitions (H_9 and higher) were not considered for the determination of the atmospheric parameters. The quantitative spectroscopic analysis of PG

2259+134 classified its primary as normal sdB-type star (see Table 5 for the results). The values for the three parameters of the single spectra, that were derived by using SPAS, were averaged. The standard deviation was calculated to estimate the uncertainty of the measured parameters' values. PG 2259+134 possesses the highest helium abundance of the seven hot subdwarf stars discussed in this work, but is still helium-deficient with respect to the Sun.

Table 5: Atmospheric parameters of PG 2259+134. Their values were determined with SPAS using the NTT EFOSC2 as well as the INT IDS spectra. The bottom line shows the averaged values of the three atmospheric parameters as well as the related standard deviation.

BJD	T_{eff} [K]	$\log(g)$ [$\frac{cm}{s^2}$]	$\log(y)$ [$\frac{n_{He}}{n_H}$]
2457655.56164738	30301	5.74	-1.73
2457655.56525858	29999	5.42	-1.64
2457655.58215668	30625	5.52	-1.83
2457655.58576778	30257	5.60	-1.56
2457655.60147378	30737	5.87	-1.57
2457655.60508488	30470	5.45	-1.75
2457936.79786417	30848	5.74	-1.72
Average & stand. dev.	30500 ± 300	5.62 ± 0.17	-1.69 ± 0.10

5.4.3 Light curve analysis

With the help of the spectroscopic results, the masses and radii can be derived by photometry. For the light curve analysis of PG 2259+134, photometric data of the Catalina Sky Survey (CSS) were used offering 357 several measurements of the system's magnitude. They data show periodic variations caused by the reflection effect, but no eclipses. Furthermore, a few measurements showed much higher magnitudes which can't be caused by astrophysical effects of the systems, which is why they have been removed. Since the CSS data are not heliocentric or barycentric corrected, they had to be corrected first. Then, we could start to constrain and determine the orbital period of the system by performing the LombScargle algorithm in Python. The period was found to be $P = 0.16345851995$ d. Using this result, the photometric data of the binary system could be phased, before the measured magnitudes M_v were converted to flux values ($F = 10^{(-0.4 \cdot M_v)}$). In this phased curve, the intensity maximum of the light curve is not yet located at a phase of $\Phi = 0.5$, as needed for the further analysis with MORO. Hence, a sinusoidal function f was fitted to the intensity values in the range of $\Phi = 0$ to $\Phi = 0.4$, where f is given by: $f(x) = a \cdot sin(2 \cdot \pi \cdot x + c) + d$. We were especially interested in the value of the variable c, which is displacing f in x-direction. With the help of gnuplot, we obtained:

$c = 0.760 \pm 0.077$, where the given uncertainty is the asymptotic standard error. The uncertainty is very high, but expected due to the large scatter of the data. Using the determined value of c, the light curve could be shifted so that the intensity maximum is located at $\Phi = 0.5$. Finally, the light curve was normalized to 1 at phase 0.25.
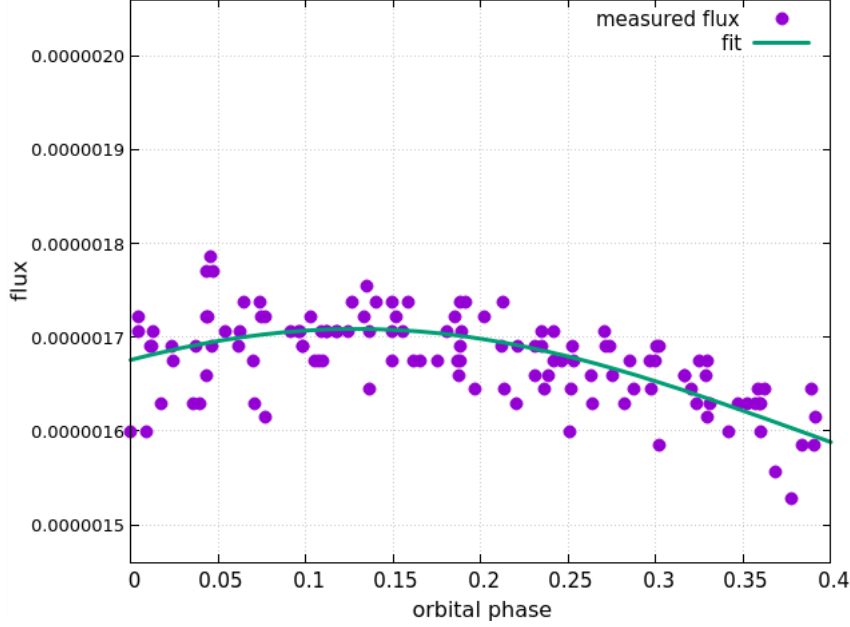

Figure 20: Plot of the sinusoidal function that was fitted to the phased light curve of PG 2259+134 in the range of $\Phi = 0$ to 0.4 in order to determine the maximum of the light curve.

For further analysis, we had to constrain the mass ratio $q = \frac{M_2}{M_1}$ and the inclination i by means of the spectroscopic results. The minimal inclination, under which eclipses may be seen from the observer's line of sight, can be expressed by (Perryman, 2011):

$$cos(i_{min}) \approx \frac{R_{sdB}}{a} \tag{11}$$

We estimated the radius of the sdB to be $R_{sdB} = 0.2R_{\odot}$ which is the usual radius of an sdB star. To determine the separation a, the third law of Kepler is used: $\frac{G(M_1+M_2)}{a^3} = \frac{4\pi^2}{P^2}$. For the system's primary, the canonical sdB mass is used so that $M_1 = 0.47M_{\odot}$ applies. The mass of the companion is assumed to be $M_2 = 0.15M_{\odot}$. Transforming of Kepler's law and plug in the values gives us: $a = 1.09R_{\odot}$. Thus we get $i_{min} = 79.43°$. Using the minimal inclination for eclipses, the systems' period, the canonical sdB mass, and the semiamplitude of the RV curve, the mass function gives us the mass of the secondary: $M_2 = 0.083M_{\odot}$.

It has to be considered that i_{min} is the lowest possible inclination to observe an eclipse from the observer's line of sight. Since PG 2259+134 is a reflection effect system showing no eclipses, i_{min} turns out to be an upper limit for the inclination angle and, hence, the derived value of M_2 is the minimal mass of the companion. To get more information about the lower limit of the inclination and how to set the start values and intervals of the other parameters, that are not fixed

during the light curve analysis, we started some test runs with MORO varying the parameters. Thereby, two results have to be emphasized: Firstly, the inclination angle moved always to values larger than $70°$ so that this value was chosen as lower limit. Plugging this result into the mass function gives the maximal mass of the secondary: $M_{2,max} = 0.089 M_{\odot}$. Consequently, the mass ratio interval, which has to be checked to find the best-fit solution, ranges from $q = 0.176$ to 0.189. Secondly, some trials tend to favour much higher inclinations and exhibit a very small
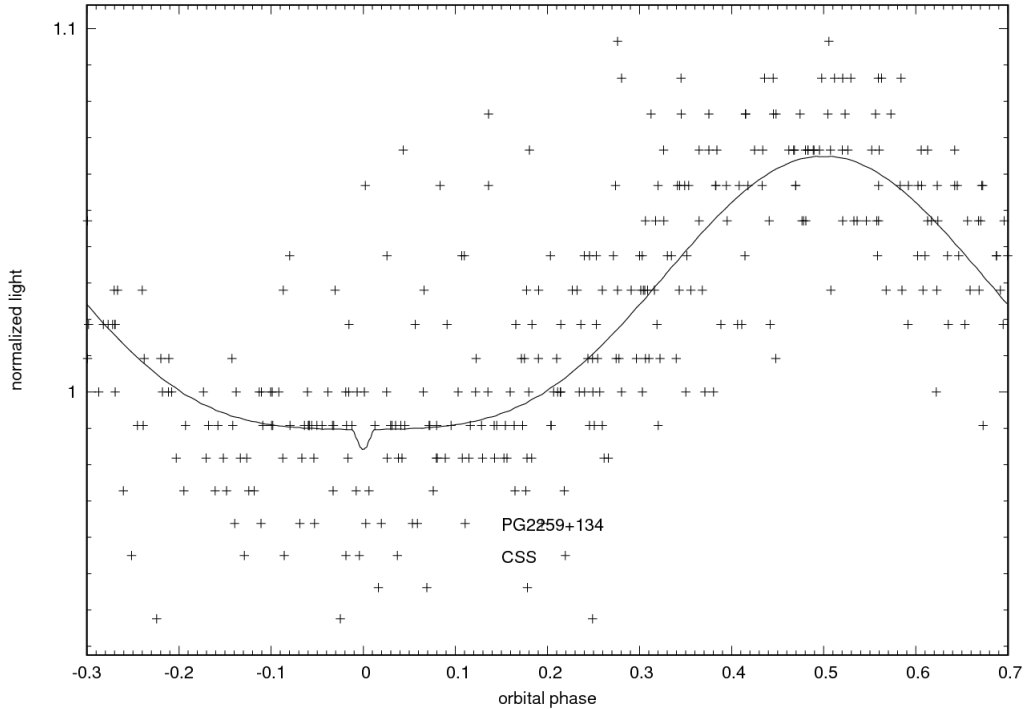
Figure 21: Fit of a synthetic light curve to the measured CSS data showing a small eclipse. The prominent deviations of many data points to the synthetic light curve are clearly noticable.

eclipse in their resulting synthetic light curve as displayed in Fig. 21. Unfortunately, the CSS light curve is not accurate enough to decide whether PG 2259+134 is an eclipsing system or not. For this reason, this sdB binary is a very interesting candidate for more precise follow-up observations.

As previously discussed in Sect. 5.1.1, MORO uses the Wilson-Devinney code for the calculation of a synthetic light curve introducing $12 + 5n$ parameters. In this work, only one light curve was available for every system, so that we got 17 parameters for each binary. The number of free, partly correlated parameters has to be reduced using spectroscopic results and values predicted from theory.

From spectroscopy, the effective temperature as well as the surface gravity of the primary are known. The gravity darkening exponent g_1 of the primary can be fixed at 1 because of its early spectral type (von Zeipel, 1924). The companion is a cool, late type main sequence star owning a convective envelope which is why its gravity darkening exponent could be set to $g_2 = 0.33$ (Lucy, 1967). By means of the the tables of Wade & Rucinski (1985), the linear limb darkening coefficient was interpolated and found to be $x_1 = 0.190$. The radiation pressure of a star

is highly correlated with its effective temperature. Hence, the radiation pressure effect, which exerts the cool secondary onto the primary, is negligible small so that δ_2 is estimated to be zero (Drechsel et al., 1995). The bolometric albedo of the sdB star was also fixed ($A_1 = 1$) because every sdB+dM binary, that was analyzed with MORO before, was close to this value (Schaffenroth, 2015). Furthermore, the first test fits haven't shown any indication for a third light. Consequently, the related parameter l_3 was set to zero. The other parameters were left as free and are listed in Table 6 (as well as the fixed parameters).
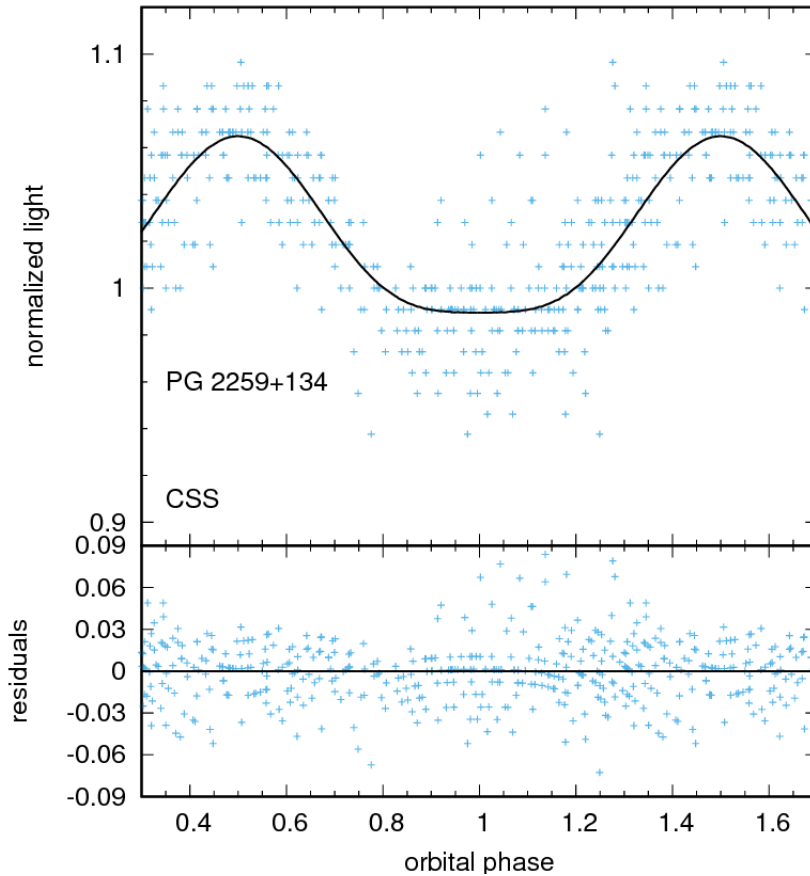
Figure 22: Plot of the phased and fitted light curve of PG 2250+134. The reflection effect is clearly recognisable. The bottom panel displays the residuals.

For the detailed light curve analysis, the mass ratio range was used which was constrained by the mass function and the spectroscopic results. During this analysis, the mass ratio interval was stepped through in 0.001 steps. Every mass ratio value was kept fixed, while the start values of the other free parameters were varied so that a large grid was calculated for each mass ratio. As described in Sect. 5.1.1, the quality of each fit is determined via the calculation of the standard deviation σ_{fit}. It pertains that the smaller σ_{fit} is, the higher is the quality of the related fit. Thus, the fit with the smallest standard deviation is assumed to be the best-fit solution. Usually, there is no unique best-fit solution owning a much smaller standard deviation than all other fits and so it relates here too. To derive the solutions with the highest quality, a Python script was used which sorts the fits by their σ_{fit} value. On the basis of this list, we adopted $q = 0.177$ to be

the best-fit solutions because this mass ratio is most frequently occurring at the top of this list. The values of the free parameters were calculated by averaging the results of the seven best-fits with $q = 0.177$. The results can be found in Table 6; the given uncertainties are the calculated standard deviations of the parameters. The shape of the synthetic and the measured light curve of the best-fit solution are shown in Fig. 21.

Table 6: Adopted light curve solution for $q = 0.177$

Fixed parameters			
Gravitational darkening exponent	g_1		1.000
	g_2		0.320
Primary's effective temperature	$T_{\text{eff,prim}}$	[K]	30500
Bolometric albedo	A_1		1.000
Radiation pressure parameter	δ_2		0.000
Limb darkening coefficient	x_1^{a}		0.190
Fraction of third light	l_3^{b}		0.000
Central wavelength	λ	[mm]	0.550
Adjusted parameters			
Inclination	i	[°]	72.7 ± 1.7
Secondary's effective temperature	$T_{\text{eff,sec}}$	[K]	2410 ± 590
Bolometric albedo	A_2		5.9 ± 1.4
Roche potential	Ω_1		7.6 ± 0.5
	Ω_2		3.40 ± 0.15
Radiation pressure parameter	δ_1		0 ± 0
Relative luminosity	$\frac{L_1}{L_1+L_2}^{\text{c}}$		0.99996 ± 0.00006
Limb darkening coefficient	$x_2(\lambda_1)$		1 ± 0
Related Roche radii			
	$r_{1,\text{pole}}$	[a]	0.136 ± 0.009
	$r_{1,\text{point}}$	[a]	0.136 ± 0.009
	$r_{1,\text{side}}$	[a]	0.136 ± 0.009
	$r_{1,\text{back}}$	[a]	0.136 ± 0.009
	$r_{2,\text{pole}}$	[a]	0.089 ± 0.007
	$r_{2,\text{point}}$	[a]	0.090 ± 0.007
	$r_{2,\text{side}}$	[a]	0.090 ± 0.007

Table 6: (continuation)

	$r_{2,\text{back}}$	[a]	0.090 ± 0.007

Comments:

[a] see Wade & Rucinski (1985)

[b] Previously done test fits showed no indication for a third light.

[c] L_2 isn't a completely indipendent parameter, but rather gets recomputed by r_2 and $T_{\text{eff,sec}}$.

Accordingly, the inclination is $i = 72.7 \pm 1.7°$. The error is quite large, but expected, since PG 2259+134 is not eclipsing. Furthermore, the luminosity of the secondary is much smaller than the sdB's luminosity revealing in a relative luminosity $L_{rel} = \frac{L_1}{L_1+L_2}$ very close to 1. Both star don't exhibit any evidences for ellipsoidal deformations. The derived result of the secondary's albedo is unusual showing a value distinctly larger than 1. But this effect is not new; it occurred also for other sdB binaries analyzed with MORO (see e.g. Schaffenroth et al., 2013; Schindewolf et al., 2015; Wolz et al., 2018) demonstrating that a simple reflection approach is failing here. In contrast to this stars, the bolometric albedo of PG 2259+134 exceeds 1 by a surprising large amount.

Furthermore, the orbital parameters may be calculated from photometry: The mass of the companion was found to be close to the stellar limit $M_2 = 0.087 \pm 0.008 M_\odot$. Since the calculated error is quite large, it is not possible to decide whether the companion's mass is slightly above or below the stellar limit. The separation can be determined by means of Eq. (2) and is found to be $a = 1.04 \pm 0.11 R_\odot$. The radii of the stars were already calculated by MORO in units of separation. Converted to solar radii, they are $R_{sdB} = 0.141 \pm 0.018 R_\odot$ and $R_{comp} = 0.093 \pm 0.013 R_\odot$. Last but not least, the surface gravity may be determined from photometry too in order to compare its value with the $log(g)$ value derived by spectroscopy. Using $g \propto \frac{M}{R^2}$, one can easily find for solar units:

$$log(g)_{phot} = \frac{log(M)}{log(R^2/R_\odot^2)} \cdot log(g_\odot) = log(M) - 2 \cdot log(R/R_\odot) + log(g_\odot) \qquad (12)$$

By this means, $log(g)_{phot} = 5.81 \pm 0.11$ resulted. The difference between the spectroscopic and the photometric surface gravity is distinct, but is within its error range. In summary, we identify PG 2259+134 as an most likely non-eclipsing reflection effect system consisting of an sdB and an M-dwarf close to the stellar limit (see Table 7).

Table 7: Parameters of PG 2259+134 that were derived by spectroscopic and photometric analysis. The errors of the radii and the separation were calculated by using the Gaussian error propagation.

PG 2259+134		
$T_{\text{eff,sdB}}$	[K]	30500 ± 300

K_1	$[\frac{km}{s}]$	47.9 ± 3.4
i	$[°]$	72.7 ± 1.7
M_{sdB}	$[M_\odot]$	0.47
M_{comp}	$[M_\odot]$	0.087 ± 0.008
a	$[R_\odot]$	1.04 ± 0.11
R_{sdB}	$[R_\odot]$	0.141 ± 0.018
R_{comp}	$[R_\odot]$	0.093 ± 0.013
$log(g)$ (sdB, spec)	$[\frac{cm}{s^2}]$	5.62 ± 0.17
$log(g)$ (sdB, phot)	$[\frac{cm}{s^2}]$	5.81 ± 0.11

5.5 OGLE 173411

5.5.1 Radial velocity curve

Seventeen EFOSC2 spectra of OGLE 173411 were recorded at the NTT telescope at La Silla whereof two were taken with grism 7 for the quantitative spectral analysis. Hence, fifteen spectra could be used to derive the radial velocity curve of the system. It appeared, that it was not possible to obtain reasonable radial velocities from two of these spectra, but for different reasons. While the first had a blended H_β line, a low (S/N) ratio, and, hence, only very noisy helium lines, the related calibration spectrum of the other showed a peculiar behavior, and other calibration lamps could not be used due to flexure of the spectrograph. Consequently, only 13 spectra could be utilized.

Table 8: Radial velocities of OGLE 173411 received from NTT EFOSC2 spectra. The RVs were determined by using SPAS. In the last column the absorption lines of each spectrum, that were used for calculating the radial velocities, are listed.

BJD	v_{rad} $[\frac{km}{s}]$	Δv_{rad}	used lines
2457936.60498921	-25	11	H_β, He I 4471
2457936.65597130	-45	10	H_β, He I 4471
2457936.71069650	1	12	H_β, He I 4471, He I 4921
2457936.76314257	59	14	H_β, He I 4471, He I 4921
2457936.81233656	65	15	H_β
2457936.83915460	77	10	H_β
2457937.53794182	51	8	H_β, He I 4471, He I 4713, He I 4921
2457937.60058509	11	6	H_β, He I 4471, He I 4713, He I 4921, He I 5015

Table 8: (continuation)

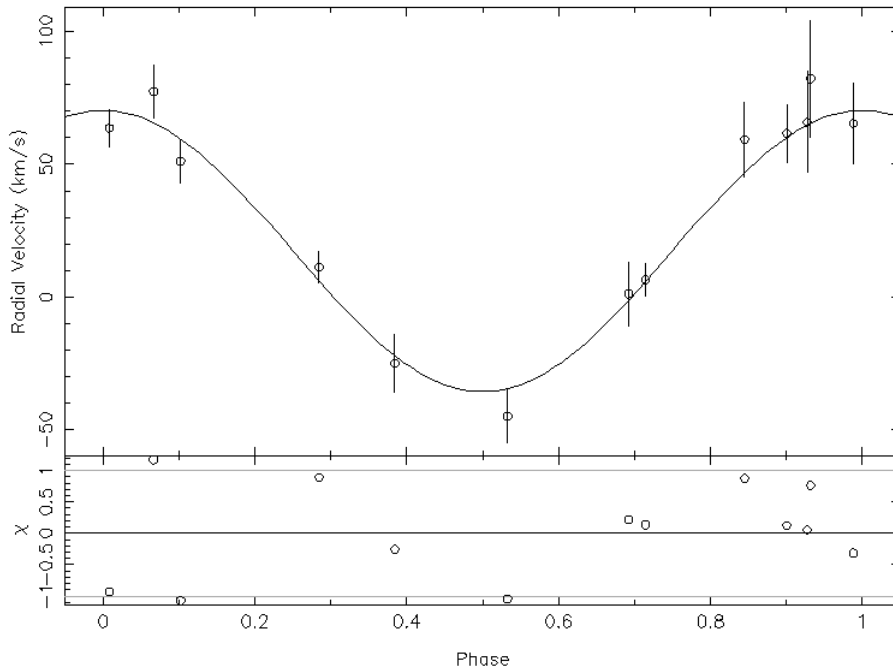| 2457937.74820954 | 7 | 6 | H_β, He I 4471, He I 4921, He I 5015 |
2457937.81201921	62	11	H_β, He I 4471, He I 4713, He I 5015
2457937.84900877	64	7	H_β, He I 4471, He I 4921
2457938.50933507	82	22	H_β, He I 4471, He I 4921, He I 5015
2457938.85109608	66	19	H_β, He I 4921, He I 5015

Figure 23: Plot of the phased radial velocity curve of OGLE 173411 and the best-fit sinusoid. In the bottom panel the residuals are shown.

Their radial velocities and the related uncertainties were calculated by SPAS and are listed in Table 8 as well as the observation times and the absorption lines used to determine the RVs. Both, observation times and radial velocities, were barycentrically corrected by using MIDAS. The errors of the RVs determined with SPAS reflect the observational conditions very well: In the second night, the seeing was good and and the Sky cloudless, so that we got the lowest errors for the RVs from this night, while poor seeing and clouds occurred in the third night increasing the uncertainties of v_{rad}.

By using the barycentric corrected radial velocities of the 13 EFOSC2 spectra, we were able to determine the radial velocity curve of OGLE 173411. As before, an interactive ISIS script was used for the analysis, the same assumptions were made (fixing period and eccentricity) and a sinusoidal function was fitted to the RV data of the system (see Fig. 23). We obtained

$K_1 = 52.9 \pm 3.3 \frac{km}{s}$ and $\gamma_1 = 17.4 \pm 2.3 \frac{km}{s}$. The sine curve, that was fitted to the measured radial velocities, match well with the observational data even though two RV points are slightly by more than 1σ from the sinusoid. As already discussed for PG 2259+134, the derived value of OGLE 173411's semiamplitudes is relatively low compared to binaries with similar orbital periods.

5.5.2 Quantitative spectral analysis

Two of the EFSOC2 spectra were taken with grism 7 and are thus suited for the determination of the atmospheric parameters. As before, SPAS was used for the quantitative spectral analysis. Fig. 24 shows a fit of synthetic spectra to one of the measured spectra of OGLE 173411. Since
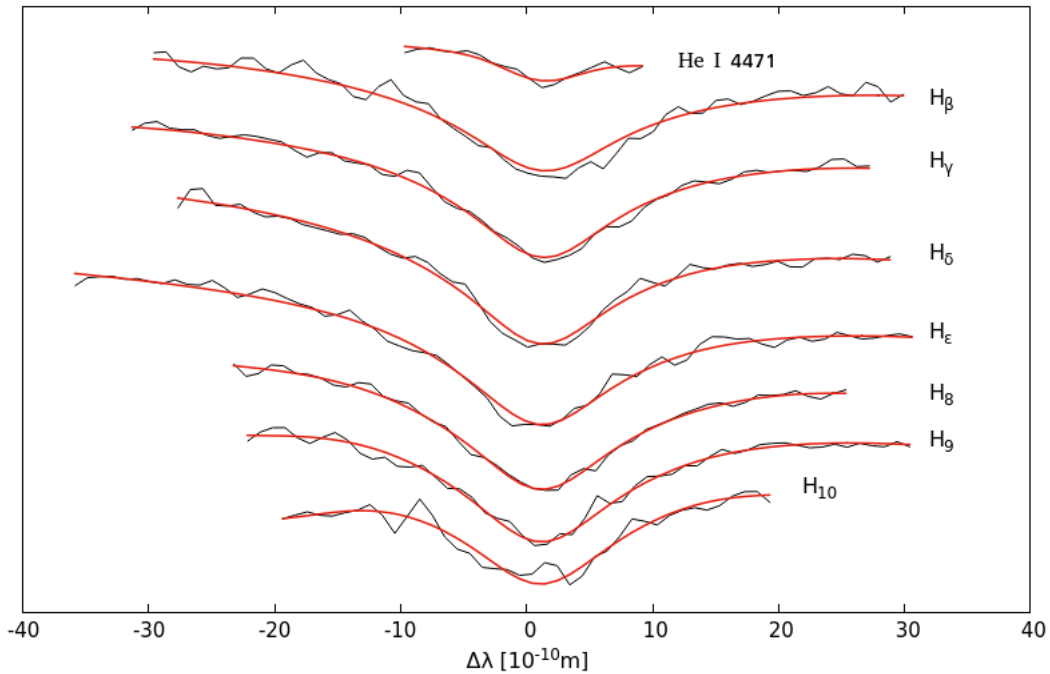
Figure 24: Example fit to the absorption lines of an individual EFOSC2 spectrum of OGLE 173411 in order to determine the atmospheric parameters. The synthetic spectra were calculated from LTE model atmospheres.

the resolution of the EFOSC2 spectra, that were recorded with grism 7, is significantly lower than the resolution of the spectra taken with grism 19, only the helium line at 4471 Å could be used to derive the atmospheric parameters in addition to the hydrogen Balmer lines which were located in the recorded wavelength range. The results are given in Table 9, the uncertainties of the parameters are the standard deviations.

Table 9: Atmospheric parameters of OGLE 173411. Their values were determined with SPAS using the NTT EFOSC2 spectra. The bottom line shows the averaged values of the three atmospheric parameters as well as the related standard deviation.

BJD	T_{eff} [K]	$log(g)$ $[\frac{cm}{s^2}]$	$log(y)$ $[\frac{n_{He}}{n_H}]$
2457936.50311162	25865	5.30	-2.40
2457937.49270576	26043	5.26	-2.55
Average & stand. dev.	25950 ± 130	5.28 ± 0.03	-2.48 ± 0.11

The primary of OGLE 173411 was found to be the coolest sdB star of our sample. The S/N ratio of the two spectra was quite low so that He I 4471 Å was the only helium line which could be used for the determination of the atmospheric parameters. Consequently, we derived a low helium abundance for the sdB star.

5.5.3 Light curve analysis

While we had photometric data from CSS for PG 2259+134, the light curve of OGLE 173411 was recorded by the OGLE program offering much more single observations (more than 4000) at better precision so that the light curve analysis would be more accurate. The light curve shows periodic variations caused by the reflection effect as well as eclipses. The primary minimum is very pronounced, the flux is descending to 50% of the flux at $\Phi = 0.25$ indicating a high inclination angle (see Fig. 25). Furthermore, the eclipse's duration is short compared to the orbital period. Since the radial velocity amplitude of the system is not very high, a rather long orbital period is expected. The ephemeris of the primary minimum was found to be

$$HJD = 2457000.0286 + 0.3435548 \cdot E \tag{13}$$

by Soszyński et al. (2017).

The OGLE light curve of the binary system was already phased by V. Schaffenroth, so that all the preliminary steps described for PG 2259+134 were not needed here. The phased curve was placed as needed for further analysis with MORO; the centre of the secondary eclipse is exactly at $\Phi = 0.5$ what was proved by fitting a Gaussian function to the eclipse. The only step, that had to be done, was normalizing the curve to 1 at $\Phi = 0.25$.

For further analysis of the light curve, we had to restrict the ranges for the mass ratio as well as for the inclination using the spectroscopic results as described in Sect. 5.4.3. Making the same assumptions for OGLE 173411 as before for PG 2259+134, we obtained $a = 1.78$, $i_{min} = 83.62°$, and a mass ratio interval ranging from $q = 0.260$ to $q = 0.268$. In contrast to PG 2259+134, which is non-eclipsing, i_{min} is the true lower limit for OGLE 173411 because this binary shows eclipses.

Furthermore, the same parameters were fixed as described for PG 2259+134 at similar values. Also the step interval of 0.001 for the mass ratio q was used again.

No unique best-fit solution could be found as for PG 2259+134, but the derived values of the standard deviation were one magnitude smaller than for the previously analyzed reflection effect system attributed to the much lower scatter of the measurements. Hence, our best-fit solutions was again adopted on the basis of the most frequently occurring q at the top of the list showing the lowest σ_{fit} values. We found $q = 0.267$ to be the best-fit solution for the light curve of OGLE 173411. The values of the free parameters were calculated via averaging the results of the four runs with $q = 0.177$ that had the best quality. The derived results are listed in Table 10; the given errors are the standard deviations of the parameters. The shape of the synthetic light curve with the lowest σ_{fit} as well as the measured light curve are displayed in Fig. 25.
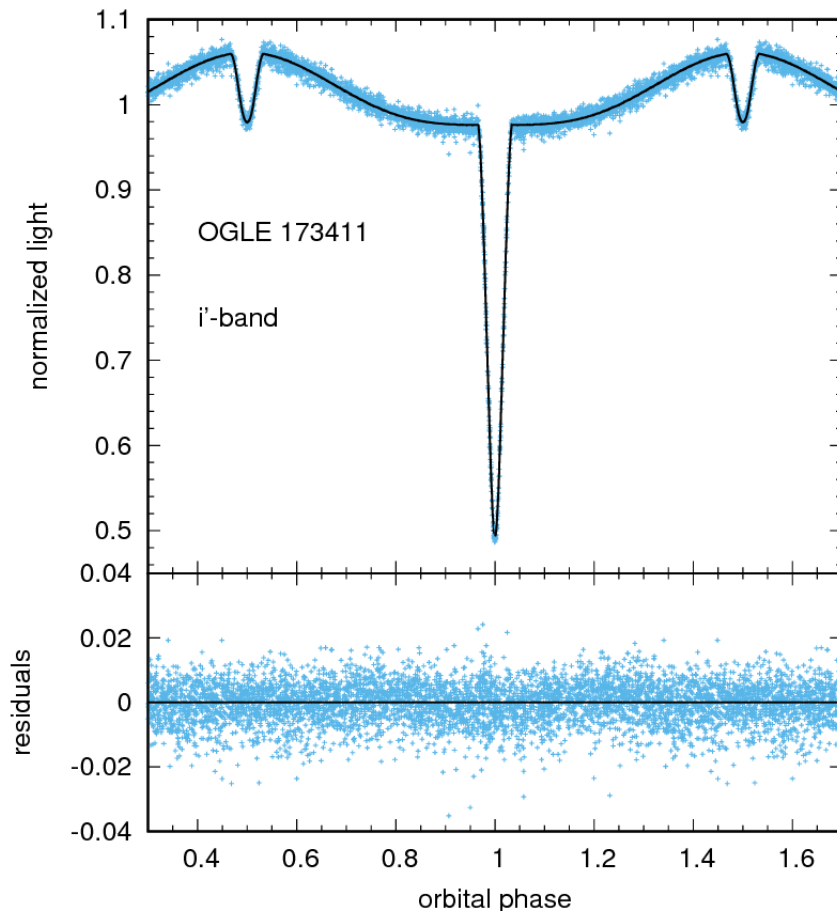
Figure 25: Plot of the phased and fitted OGLE light curve of OGLE 173411. Primary and secondary minima as well as the reflection effect are clearly recognisable. The residuals are shown in the bottom panel.

In contrast to the Catalina Sky Survey, the OGLE astronomers are using bandpass filters for their observation. Consequently, the central wavelength of the photometric observations is not provided by the CCD, but rather by the sensitivity range of the applied bandpass filter. All OGLE light curves, presented in this work, were recorded with an i'-band filter with the best

throughput at $\lambda = 8000$ Å.

Table 10: Model parameters of the light curve solution for $q = 0.267$

Fixed parameters			
Gravitational darkening exponent	g_1		1.000
	g_2		0.320
Primary's effective temperature	$T_{\text{eff,prim}}$	[K]	26000
Bolometric albedo	A_1		1.000
Radiation pressure parameter	δ_2		0.000
Limb darkening coefficient	x_1^{a}		0.190
Fraction of third light	l_3^{b}		0.000
Central wavelength	λ	[mm]	0.800
Adjusted parameters			
Inclination	i	[°]	86.75 ± 0.25
Secondary's effective temperature	$T_{\text{eff,sec}}$	[K]	2880 ± 950
Bolometric albedo	A_2		4.49 ± 0.20
Roche potential	Ω_1		8.23 ± 0.07
	Ω_2		4.21 ± 0.06
Radiation pressure parameter	δ_1		0.002 ± 0.003
Relative luminosity	$\frac{L_1}{L_1+L_2}^{\text{c}}$		0.998 ± 0.005
Limb darkening coefficient	$x_2(\lambda_1)$		0.950 ± 0.022
Related Roche radii			
	$r_{1,\text{pole}}$	[a]	0.1253 ± 0.0016
	$r_{1,\text{point}}$	[a]	0.1256 ± 0.0016
	$r_{1,\text{side}}$	[a]	0.1255 ± 0.0016
	$r_{1,\text{back}}$	[a]	0.1256 ± 0.0016
	$r_{2,\text{pole}}$	[a]	0.0936 ± 0.0020
	$r_{2,\text{point}}$	[a]	0.0942 ± 0.0019
	$r_{2,\text{side}}$	[a]	0.0938 ± 0.0020
	$r_{2,\text{back}}$	[a]	0.0942 ± 0.0020

Comments:

[a] see Wade & Rucinski (1985)

[b] Previously done test fits showed no indication for a third light.

[c] L_2 isn't a completely indipendent parameter, but rather gets recomputed by r_2 and $T_{\text{eff,sec}}$.

We obtained an inclination angle of $i = 86.75 \pm 0.25°$ so that the orbital plane of the system lays almost in the line of sight as predicted. Compared to the previously discussed non-eclipsing reflection effect system, the uncertainty of the inclination is much smaller owning to the visible eclipses. Again, the companion's luminosity is much smaller than that of the sdB star, but more than one order of magnitude higher than for the very small secondary of PG 2259+134. As seen before, the bolometric albedo of the companion is remarkable larger than 1 originating from the same phenomenon.

Using Kepler's law and the mass function and plugging in the parameters derived from spectroscopy and photometry, we obtain $M_2 = 0.123 \pm 0.009 M_\odot$, $a = 1.73 \pm 0.15 R_\odot$, and $R_{sdB} = 0.217 \pm 0.019 R_\odot$ as well as $R_{comp} = 0.1626 \pm 0.015 R_\odot$ showing that OGLE 173411 has an M-dwarf companion. For comparison, we determined the surface gravity from the photometric data yielding $log(g)_{phot} = 5.43 \pm 0.08$, which is significantly higher than the spectroscopic value. But, because only two spectra were available to derive the atmospheric parameters, the calculated uncertainty of $log(g)_{spec}$ is most likely underestimated. Assuming an error of ± 0.1 dex for $log(g)_{spec}$, which is more realistic, it is obvious that the values are within their respective error ranges. All results, which were derived from spectroscopic and photometric analysis, are summarized in Table 11.

Table 11: Parameters of OGLE 173411 that were derived by spectroscopic and photometric analysis. The errors of the radii and the separation were calculated by using the Gaussian error propagation.

OGLE 173411		
$T_{\text{eff,sdB}}$	$[K]$	25950 ± 130
K_1	$[\frac{km}{s}]$	52.9 ± 3.3
i	$[°]$	86.75 ± 0.25
M_{sdB}	$[M_\odot]$	0.47
M_{comp}	$[M_\odot]$	0.123 ± 0.009
a	$[R_\odot]$	1.73 ± 0.15
R_{sdB}	$[R_\odot]$	0.217 ± 0.019
R_{comp}	$[R_\odot]$	0.163 ± 0.015
$log(g)$ (sdB, spec)	$[\frac{cm}{s^2}]$	5.28 ± 0.03
$log(g)$ (sdB, phot)	$[\frac{cm}{s^2}]$	5.43 ± 0.08

Overall, the derived results are showing that OGLE 173411 is an eclipsing, short periodic binary star system consisting of an sdB and an M-dwarf. Accordingly, OGLE 173411 meets the requirements to be classified as a HW Vir system.

5.6 OGLE 361688

5.6.1 Radial velocity curve

At La Silla, eleven spectra of OGLE 361688 were taken whereof two were recorded by using grism 7 so that nine spectra remained for the determination of the radial velocity curve. Compared to OGLE 173411, OGLE 361688 is fainter and several other stars are visible on the raw spectra (see Fig. 26, left picture). During the data reduction of the eleven EFOSC2 spectra, it certainly appeared that two of the nine raw spectra recorded with grism 19 do not comprise the spectra of OGLE 361688 because the telescope was mostly likely wrong adjusted (see Fig. 26). Hence, we could only use seven spectra to derive the radial velocity curve of the system.
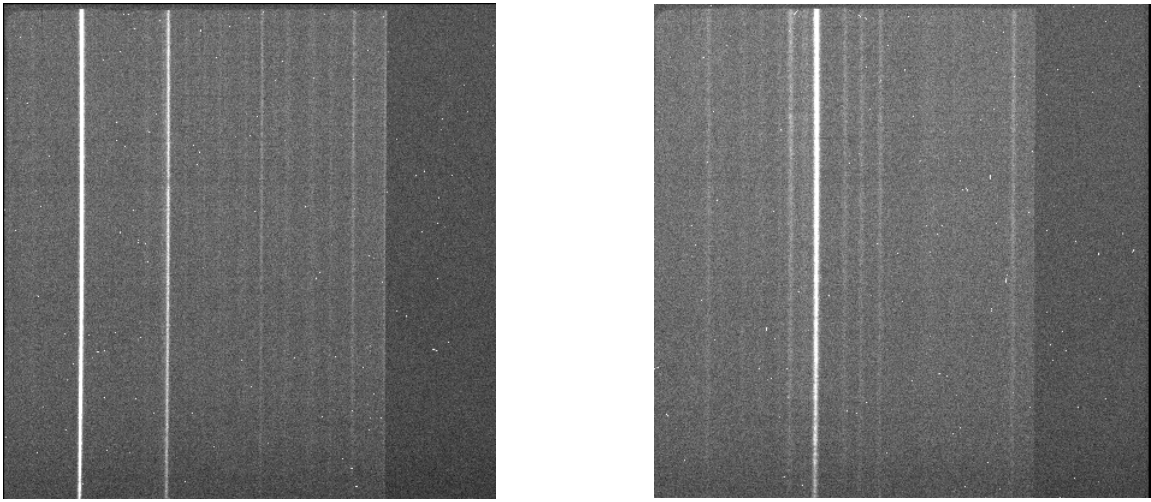

Figure 26: Left: Raw spectra of OGLE 361688. Right: Raw spectra that should display OGLE 361488. It is obvious that this spectrum shows a different Sky region comapred to the left picture.

Due to the low resolution of the spectra and their small number, the uncertainties of the RV curve are expected to be large causing also large errors for the orbital parameters of the system and the components' masses. For this reason, this system should be very interesting for spectroscopic follow-up observations. The remaining spectra were analyzed by using SPAS and their radial velocities as well as the related uncertainties were determined (see Table 12).

Table 12: Radial velocities of OGLE 361688 received from NTT EFOSC2 spectra. The RVs were determined by using SPAS. In the last column the absorption lines of each spectrum, that were used for calculating the radial velocities, are listed.

BJD	v_{rad} [$\frac{km}{s}$]	Δv_{rad}	used lines
2457936.5680348	25	29	H_β
2457936.6194562	-48	21	H_β, He I 4471
2457936.6959355	21	13	H_β
2457936.7485648	73	17	H_β, He I 4471

Table 12: (continuation)

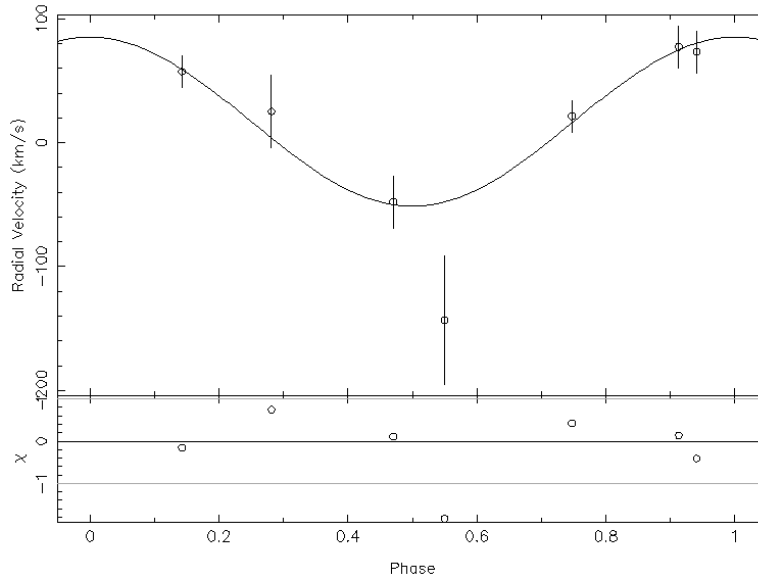| 2457937.5666626	77	17	H_β, He I 4471
2457937.6292262	57	13	H_β, He I 4471
2457938.5570901	-143	52	H_β, He I 4471

Figure 27: Plot of the phased radial velocity curve of OGLE 361688 and the best-fit sinusoidal function showing a significant outlier at a phase of $\Phi \approx 0.55$. In the bottom panel the residuals are pictured.

The last spectrum was also the last recorded spectrum of the third night before the astronomers had to abort their observations due to clouds and poor seeing. Hence, the uncertainty of the RV derived from the last spectrum is very high. Again, observational times and radial velocities were barycentrically corrected by using MIDAS.

By means of the barycentric corrected RVs of the seven EFOSC2 spectra, we were able to determine the related radial velocity curve of OGLE 361688. Making the same assumptions as before, we derived the radial velocity curve by fitting a sinusoid to the measured radial velocities (see Fig. 27). Obviously, the RV value, which we have received from the last recorded spectrum, is located far away from the fitted sine curve (almost 2σ), while the position of the other points match perfectly with the sinusoidal function. We obtained $K_1 = 68.1 \pm 11.8 \frac{km}{s}$ and $\gamma_1 = 16.91 \pm 8.0 \frac{km}{s}$. Because of this remarkable outlier, we got a reduced χ^2 larger than 1 increasing the calculated errors. This effect has already been considered during the error-calculation of the semiamplitude and the systemic velocity.

5.6.2 Quantitative spectral analysis

Two of the recorded spectra of OGLE 361688 are adapted for the determination of the effective temperature, surface gravity, and helium abundance, because they were taken with grism 7. The spectra showed the typical shape of an sdB-type star exhibiting strong hydrogen Balmer lines and weak helium lines. Model spectra calculated from LTE model atmospheres of Heber et al. (2000) were fitted to these absorption lines in order to determine the atmospheric parameters (see Fig. 28).
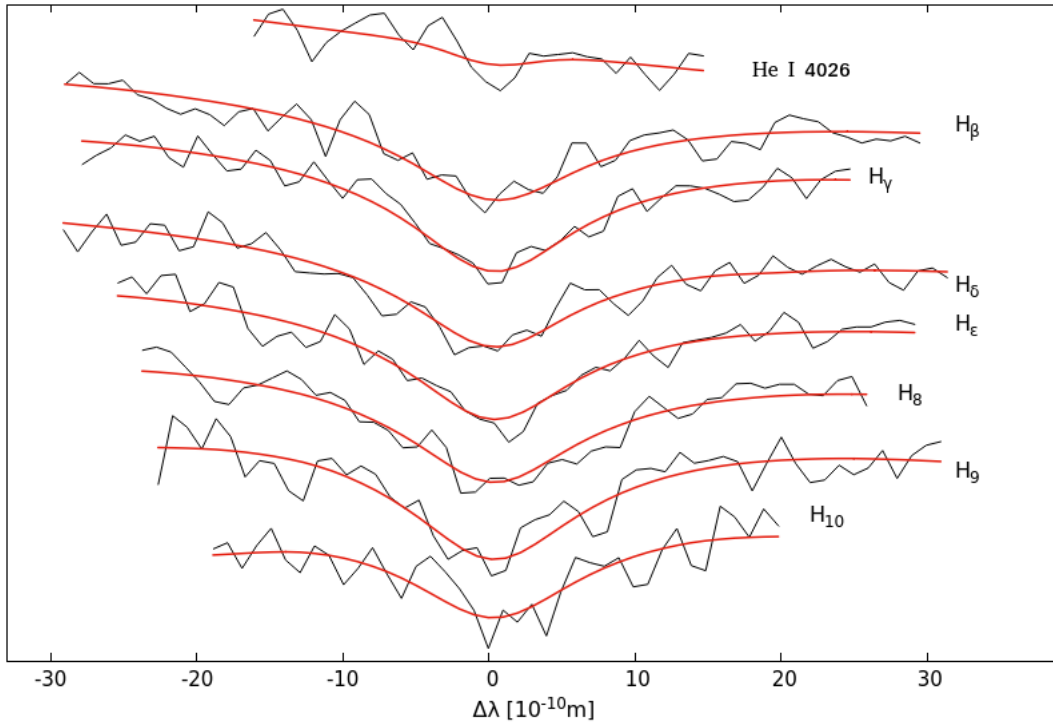

Figure 28: Example fit to the absorption lines of an individual EFOSC2 spectrum of OGLE 361688 in order to determine the atmospheric parameters. The synthetic spectra were calculated from LTE model atmospheres.

Table 13: Atmospheric parameters of OGLE 361688. Their values were determined with SPAS using the NTT EFOSC2 spectra. The bottom line shows the averaged values of the three atmospheric parameters as well as the related standard deviation.

BJD	T_{eff} [K]	$\log(g)$ [$\frac{cm}{s^2}$]	$\log(y)$ [$\frac{n_{He}}{n_H}$]
2457936.5194137	26298	5.14	-2.37
2457937.5047650	28170	5.25	-2.40
Average & stand. dev.	27200 ± 1300	5.20 ± 0.08	-2.385 ± 0.022

Compared to OGLE 173411 and PG 2259+134, OGLE 361688 possesses weaker and less helium lines in its spectra. The results derived by the quantitative spectroscopic analysis of the primary star are summarized in Table 13 demonstrating that the brighter component of OGLE 361688 is an sdB-type star. The primary shows a quite low temperature as well as a low surface gravity, although the temperature is higher than of OGLE 173411. The helium abundance ranges in the midfield of helium-poor sdB stars.

5.6.3 Light curve analysis

For the photometric analysis of the system, a light curve recorded by the OGLE program was used offering 669 several measurements of the system's magnitude. Periodic variations as well as primary and secondary eclipses can be found in the data. The periodic brightness variations are caused by the reflection effect. Even if the primary minimum of OGLE 173411 was very pronounced showing a decline to 50% of the flux at $\Phi = 0.25$, the eclipse of OGLE 361688 is still more pronounced showing a flux descending to 15% of the flux at $\Phi = 0.25$ (see Fig. 29). The flux decreasing by about 85% indicates that the systems' orbital plane lays almost in the same plane as the observer's line of sight and that the radius of the companion has to be as large as the primary's radius or even larger. The ephemeris of the primary minimum of OGLE 361688 was found to be

$$HJD = 2457000.0658 + 0.2723178 \cdot E \tag{14}$$

by Soszyński et al. (2017).

As before, the light curve was already phased by V. Schaffenroth and the only preliminary step, that had to be implemented, was the normalization of the curve at $\Phi = 0.25$. The minimal inclination was determined to be $i_{min} = 82.54°$ and the mass ratio interval was found to range from $q = 0.321$ to 0.330 by using the mass function and Kepler's law. For further light curve analysis, the same parameter were fixed at the similar values as before.

Again, no unique best-fit solution could be found. Compared to OGLE 173411, the values of the standard deviations are about 60% larger, which is caused by the considerable smaller number of individual measurements and some outliers e.g. near the minimum of the secondary eclipse (see Fig. 29). Hence, we applied the same procedure as before. In this way, we obtained $q = 0.328$ to be the best-fit solution of the light curve. The values of the fitted parameters are listed in Table 14 and were determined by averaging the results of the six best-fit runs with $q = 0.328$. The given uncertainties are the calculated standard deviations of the parameters.

Table 14: Best-fit model parameters of the light curve of OGLE 361688 for $q = 0.321$

Fixed parameters			
Gravitational darkening exponent	g_1		1.000
	g_2		0.320

Table 14: (continuation)

Primary's effective temperature	$T_{\text{eff,prim}}$	[K]	27200
Bolometric albedo	A_1		1.000
Radiation pressure parameter	δ_2		0.000
Limb darkening coefficient	x_1^{a}		0.190
Fraction of third light	l_3^{b}		0.000
Central wavelength	λ	[mm]	0.800

Adjusted parameters			
Inclination	i	[°]	86.35 ± 0.08
Secondary's effective temperature	$T_{\text{eff,sec}}$	[K]	3000 ± 700
Bolometric albedo	A_2		4.81 ± 0.47
Roche potential	Ω_1		8.06 ± 0.13
	Ω_2		3.40 ± 0.01
Radiation pressure parameter	δ_1		0.012 ± 0.014
Relative luminosity	$\frac{L_1}{L_1+L_2}^{\text{c}}$		0.995 ± 0.007
Limb darkening coefficient	$x_2(\lambda_1)$		0.77 ± 0.12

Related Roche radii			
	$r_{1,\text{pole}}$	[a]	0.1277 ± 0.0017
	$r_{1,\text{point}}$	[a]	0.1280 ± 0.0017
	$r_{1,\text{side}}$	[a]	0.1279 ± 0.0017
	$r_{1,\text{back}}$	[a]	0.1280 ± 0.0017
	$r_{2,\text{pole}}$	[a]	0.1549 ± 0.0008
	$r_{2,\text{point}}$	[a]	0.1582 ± 0.0012
	$r_{2,\text{side}}$	[a]	0.1561 ± 0.0008
	$r_{2,\text{back}}$	[a]	0.1587 ± 0.0008

Comments:

[a] see Wade & Rucinski (1985)

[b] Previously done test fits showed no indication for a third light.

[c] L_2 isn't a completely indipendent parameter, but rather gets recomputed by r_2 and $T_{\text{eff,sec}}$.

The inclination was found to be $i = 86.35 \pm 0.08°$ which is a slightly lower value than we had determined for OGLE 173411. The derived uncertainty of OGLE 361688's inclination angle is much smaller than of OGLE 173411 because the six used MORO fits of OGLE 361688's light

curve tend to a smaller inclination range. The luminosity of the companion is much smaller than the primary's luminosity, but compared to OGLE 173411 the companion's luminosity is 2.5 times larger. As seen for all the other analyzed systems, the bolometric albedo of the secondary is distinctly larger than 1 originating from an insufficient approach of the reflection effect. The related Roche radii exhibit no indications for ellipsoidal deformations (see Table 14).
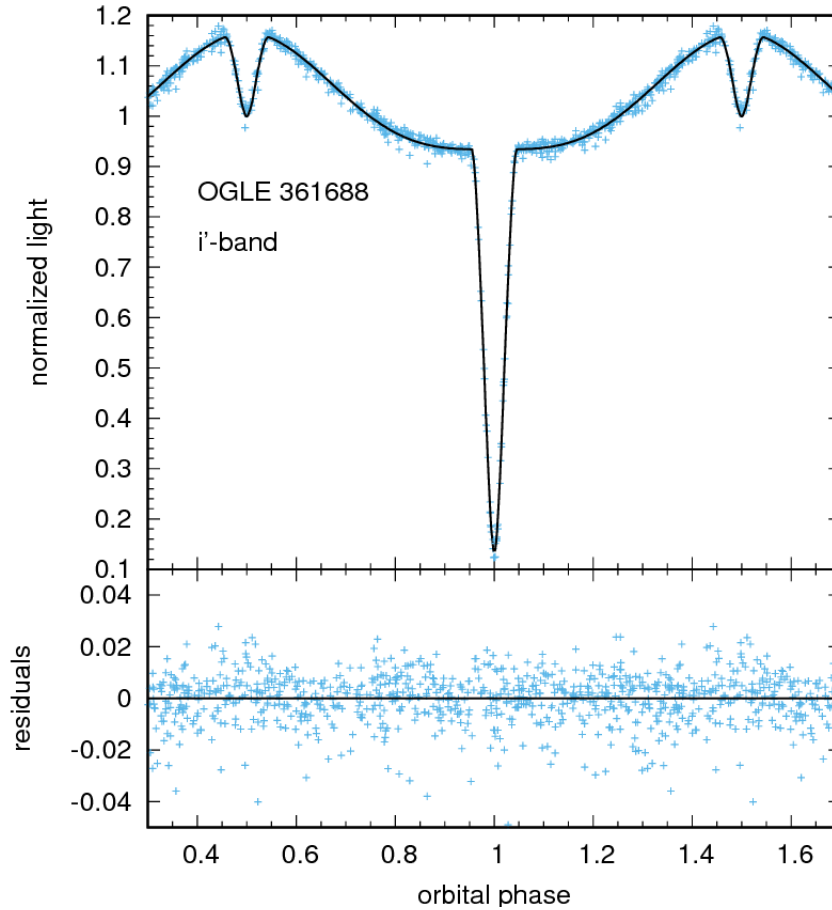

Figure 29: Plot of the phased and fitted OGLE light curve of the Hw Vir OGLE 361688. Primary and secondary minima as well as the reflection effect are clearly recognisable. The residuals are shown in the bottom panel.

With the help of the mass function and Kepler's law, the orbital parameters of the binary and the mass of the secondary could be calculated yielding $M_2 = 0.15 \pm 0.03 M_\odot$, $a = 1.51 \pm 0.29 R_\odot$, and $R_{sdB} = 0.19 \pm 0.04 R_\odot$ as well as $R_{comp} = 0.24 \pm 0.06 R_\odot$. As predicted, the companion owns a larger radius than the sdB causing - in combination with the high inclination angle - the very deep primary eclipse. Obviously, the companion possesses the typical mass and size of an M-dwarf which is why we may accordingly conclude that OGLE 361688 is another new HW Virginis system. The most important spectroscopic and photometric results are summarized in Table 15.

Table 15: Parameters of OGLE 361688 that were derived by spectroscopic and photometric analysis. The errors of the radii and the separation were calculated by using the Gaussian error propagation.

OGLE 361688		
$T_{\text{eff,sdB}}$	$[K]$	27200 ± 1300
K_1	$[\frac{km}{s}]$	68.1 ± 11.8
i	$[°]$	86.35 ± 0.08
M_{sdB}	$[M_\odot]$	0.47
M_{comp}	$[M_\odot]$	0.15 ± 0.03
a	$[R_\odot]$	1.52 ± 0.35
R_{sdB}	$[R_\odot]$	0.19 ± 0.05
R_{comp}	$[R_\odot]$	0.24 ± 0.06
$log(g)$ (sdB, spec)	$[\frac{cm}{s^2}]$	5.20 ± 0.08
$log(g)$ (sdB, phot)	$[\frac{cm}{s^2}]$	5.54 ± 0.19

5.7 OGLE 416194 – a hot HW Vir

5.7.1 Radial velocity curve

Twelve spectra of OGLE 416194 were taken with the EFOSC2 spectrograph, thereof eleven with grism 19 so that these eleven spectra could be used to determine the radial velocity curve of the system. OGLE 416194 is the faintest of the three OGLE objects analyzed in this work. Unfortunately, the same mistake as described for OGLE 361688 was revealed during data reduction so that three images do not show an sdB spectrum. Furthermore, the H_β line of one spectrum was blended so that SPAS wasn't able to fit this absorption line correctly. Because of the small spectral range, which is offered by spectra taken with grism 19, H_β is the main indicator for the determination of the radial velocity. For this reason, the spectrum with the blended H_β line could not be used for RV measurement. Hence, only seven spectra could be evaluated.

Table 16: Radial velocities of OGLE 416194 received from NTT EFOSC2 spectra. The RVs were determined by using SPAS. In the last column the absorption lines of each spectrum, that were used for calculating the radial velocities, are listed.

BJD	v_{rad} $[\frac{km}{s}]$	Δv_{rad}	used lines
2457936.59010735	-70	39	H_β
2457936.64121479	-122	40	H_β, He II 4686

Table 16: (continuation)

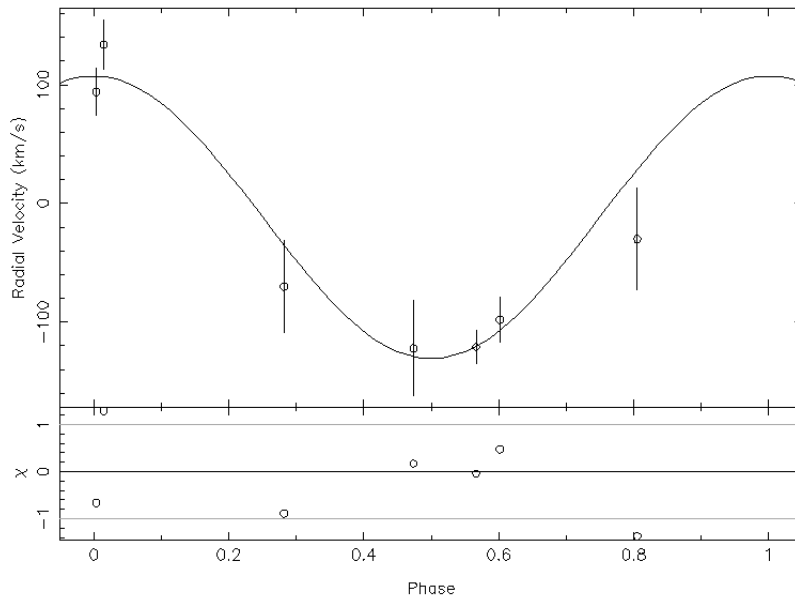|			
2457936.67538738	-98	19	H_β
2457936.72965193	-30	43	H_β
2457936.78257015	94	20	H_β
2457937.58537950	134	21	H_β, He II 4686
2457937.73245348	-121	14	H_β

Figure 30: Plot of the phased radial velocity curve of OGLE 416194 and the best-fit sinusoidal function. The RV curve has two outliers. In the bottom panel the residuals are shown.

With the help of SPAS, the radial velocities (and their uncertainties) of the seven remaining spectra were calculated; the results are given in Table 16 beside the observational times and the absorption lines used for the RV determination. Since the object is fainter than OGLE 173411, the derived errors are larger than for the brighter system OGLE 173411.

We used the barycentric corrected radial velocities of the related EFOSC2 spectra to derive the radial velocity curve of the binary. Again, our interactive ISIS script was used for the analysis. Therefor, the period as well as the eccentricity were fixed. The fit of a sinusoidal function to the measured and phased RVs revealed $K_1 = 118.1 \pm 10.7 \frac{km}{s}$ and $\gamma_1 = -11.75 \pm 9.2 \frac{km}{s}$. Hence, the binary's components orbiting much faster around their common centre of mass than the stars of the previously discussed systems. Not all of the RVs match well with the fitted sine curves; two are more than 1σ apart from the sine curve revealing in a reduced χ^2 larger than 1.

5.7.2 Quantitative spectral analysis

Just one spectrum of OGLE 416194 was recorded with grism 7 for the determination of the atmospheric parameters. As one can see in Fig. 31, the S/N-ratio was low, which is why the higher Balmer lines could not be used for the analysis. For the same reason, the weak helium lines were very noisy but are needed to determine the helium abundance of the star. To restrict the measuring error, three helium lines were used, even if they are shallow.
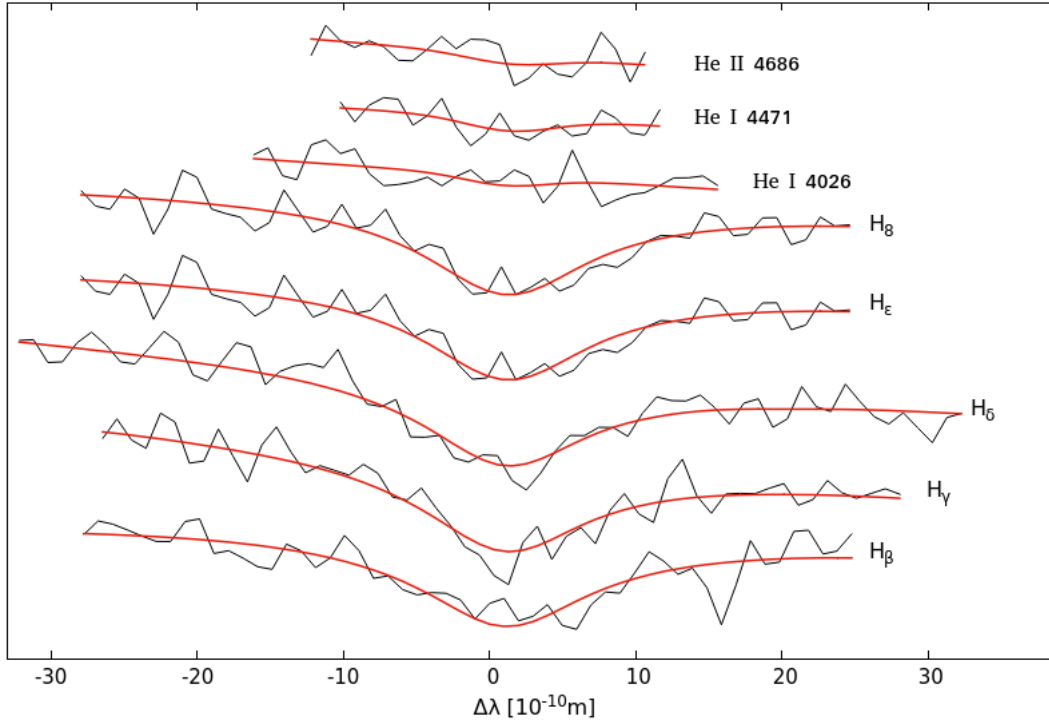

Figure 31: Example fit to the absorption lines of an individual EFOSC2 spectrum of OGLE 416194 in order to determine the atmospheric parameters. The synthetic spectra were calculated from LTE model atmospheres (Heber et al., 2000).

We obtained that the primary of OGLE 416194 is a hot subdwarf owning an effective temperature of $T_{\text{eff}} = 35600 \pm 920$ K ranging in the upper area of sdB's surface temperature. Since the temperature is so high, it another possibility exists: the primary could also be a helium-poor sdOB star. Which of the two options pertains, can't be answered on basis of our data. Surface gravity as well as helium abundance are located in the normal range for helium-poor hot subdwarfs.

Table 17: Atmospheric parameters of OGLE 416194. Their values were determined with SPAS using a NTT EFOSC2 spectrum.

BJD	T_{eff} [K]	$\log(g)$ [$\frac{cm}{s^2}$]	$\log(y)$ [$\frac{n_{He}}{n_H}$]
2457936.53947452	35600 ± 920	5.34 ± 0.20	-2.21 ± 0.35

5.7.3 Light curve analysis

The light curve of the binary system was taken by OGLE astronomers comprising 367 several observations, the lowest number of single measurements of the three OGLE stars. Consequently, the derived quality of the light curve fits should be lower than for OGLE 173411 or 316688. The photometric data were again phased by V. Schaffenroth, showing a periodic variability caused by the reflection effect and a primary as well as a secondary eclipse which are both deeper and more pronounced as already seen for OGLE 361688. For this reason this system should exhibit a very high inclination angle and a companion which has a larger radius than the hot subdwarf. During the first analysis of the data, we found out that the secondary minimum of the phased data was not exactly positioned at phase 0.5. Hence, we identified the precise location of the secondary minimum by fitting an inverse Gaussian function to the eclipse and subsequently shifting the light curve to the phase needed. The ephemeris of the primary minimum of OGLE 361688 was found to be

$$HJD = 2457000.2491 + 0.2666134 \cdot E \tag{15}$$

by Soszyński et al. (2017).

Before we started the light curve analysis with MORO, we had to normalize the light at $\Phi = 0.25$, to derive a lower minimum for the inclination, and to constrain the mass ratio range of the system. The minimal inclination was calculated to be $i_{min} = 82.42°$ the mass ratio interval ranges from $q = 0.644$ to 0.657. Furthermore, some parameters were fixed which were known from spectroscopy or theory (see Table 18). Again, a step interval of 0.001 was used for the mass ratio so that 14000 several synthetic light curves with different start parameters were fitted to the measured data.

As before, no unique solution could be found for OGLE 416194 too. In contrast to the two other OGLE binaries analyzed in this work the quality of the fit is worse owning a σ_{fit}, which is 50% higher than of OGLE 361688. Due to the less number of photometric measurements, this result was expected. To derive a conclusive solution, a list was created sorting the single fits by their σ_{fit} values. The mass ratio, which is most frequently named at the top of this list, was chosen to be the best-fit solution. On basis of this procedure, $q = 0.651$ was found to be the best-fit solution. The final results of the light curve analysis are listed in Table 18; the given values are the averaged values of the five solution with $q = 0.651$ possessing the highest quality. Again, the errors displayed in the Table are the calculated standard deviations of the parameters.

Table 18: Adopted best-fit light curve solution for $q = 0.651$

Fixed parameters			
Gravitational darkening exponent	g_1		1.000
	g_2		0.320

Table 18: (continuation)

Primary's effective temperature	$T_{\text{eff,prim}}$	[K]	34900
Bolometric albedo	A_1		1.000
Radiation pressure parameter	δ_2		0.000
Limb darkening coefficient	x_1^{a}		0.190
Fraction of third light	l_3^{b}		0.000
Central wavelength	λ	[mm]	0.800

Adjusted parameters			
Inclination	i	[°]	87.05 ± 0.21
Secondary's effective temperature	$T_{\text{eff,sec}}$	[K]	2800 ± 500
Bolometric albedo	A_2		7.44 ± 0.13
Roche potential	Ω_1		8.64 ± 0.11
	Ω_2		4.961 ± 0.022
Radiation pressure parameter	δ_1		0.006 ± 0.007
Relative luminosity	$\frac{L_1}{L_1+L_2}^{\text{c}}$		0.997 ± 0.004
Limb darkening coefficient	$x_2(\lambda_1)$		0.247 ± 0.023

Related Roche radii			
	$r_{1,\text{pole}}$	[a]	0.1244 ± 0.0008
	$r_{1,\text{point}}$	[a]	0.1248 ± 0.0008
	$r_{1,\text{side}}$	[a]	0.1246 ± 0.0008
	$r_{1,\text{back}}$	[a]	0.1248 ± 0.0008
	$r_{2,\text{pole}}$	[a]	0.1715 ± 0.0010
	$r_{2,\text{point}}$	[a]	0.1747 ± 0.0015
	$r_{2,\text{side}}$	[a]	0.1726 ± 0.0010
	$r_{2,\text{back}}$	[a]	0.1745 ± 0.0011

Comments:

[a] see Wade & Rucinski (1985)

[b] Previously done test fits showed no indication for a third light.

[c] L_2 isn't a completely indipendent parameter, but rather gets recomputed by r_2 and $T_{\text{eff,sec}}$.

The inclination was found to be $i = 87.05 \pm 0.21°$, which is the highest inclination angle of the six systems, that were photometrically analyzed in this thesis. Beside this, the system has also the highest secondary's bolometric albedo of all systems with $A_2 = 7.44 \pm 0.13$. Since MORO

uses an insufficient model of the reflection effect and OGLE 416194's primary owns the highest effective temperature of all systems, MORO needed a very high A_2 to recreate the shape of light curve. Hence, the derived results are expected.
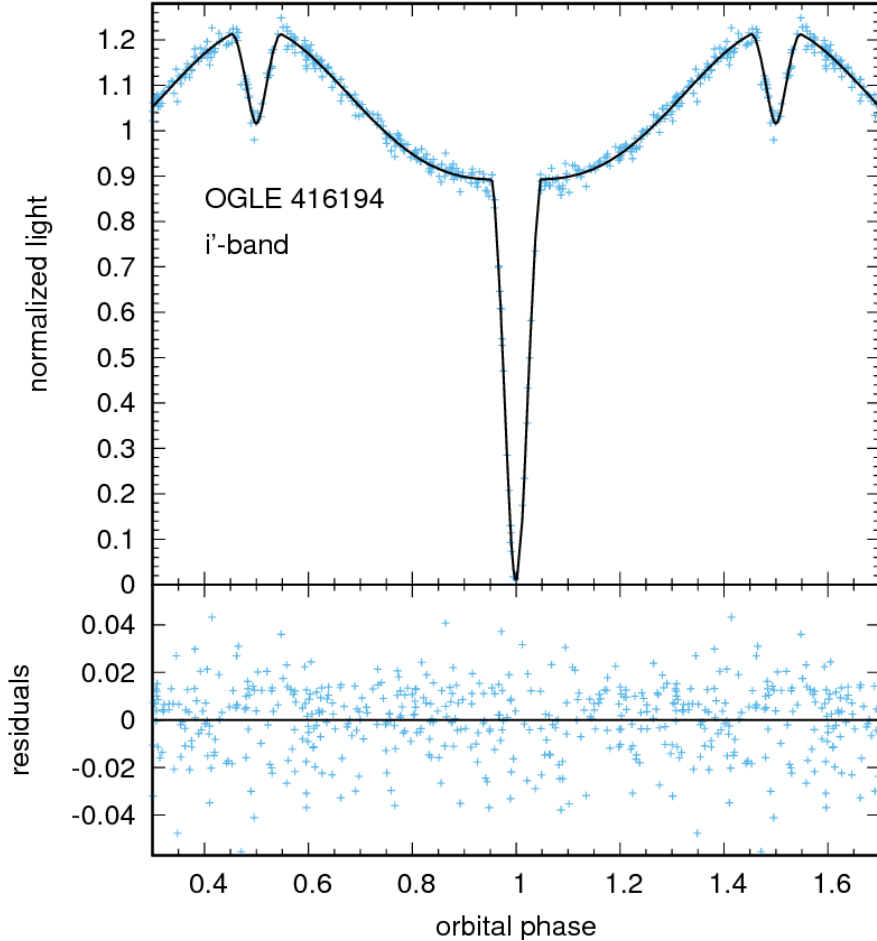

Figure 32: Plot of the phased and fitted OGLE light curve of the Hw Vir OGLE 416194. Primary and secondary minima as well as the reflection effect are clearly recognisable. The residuals are shown in the bottom panel.

Using Kepler's law as well as the mass function, the orbital parameters and the secondary's mass can be calculated. We obtained $a = 1.62 \pm 0.19 R_\odot$, $R_{sdB} = 0.202 \pm 0.024 R_\odot$, $R_{comp} = 0.281 \pm 0.033 R_\odot$, and $M_2 = 0.30 \pm 0.04 M_\odot$, wherewith the companion can be classified as an M-dwarf. As predicted by the light curve's shape, the radius of the secondary is larger than of the sdB causing - together with the high inclination - the deep primary eclipse whereby the flux descending to 2% of the flux at $\Phi = 0.25$ (see Fig. 32). For comparison, the surface gravity was determined by using the results from photometric analysis yielding $log(g)_{phot} = 5.49 \pm 0.11$. Obviously, this result lays in the error range of $log(g)_{spec}$ so that our photometric results are consistent with spectroscopy. Overall, we derived OGLE 416194 to be an eclipsing binary system, which consists of a hot sdB or an sdOB star and an M-dwarf. Hence, we found another HW Vir system.

Table 19: Parameters of OGLE 416194 that were derived by spectroscopic and photometric analysis. The errors of the radii and the separation were calculated by using the Gaussian error propagation.

OGLE 416194		
$T_{\text{eff,sdB}}$	$[K]$	35600 ± 920
K_1	$[\frac{km}{s}]$	118.1 ± 10.7
i	$[°]$	87.05 ± 0.21
M_{sdB}	$[M_\odot]$	0.47
M_{comp}	$[M_\odot]$	0.30 ± 0.04
a	$[R_\odot]$	1.62 ± 0.19
R_{sdB}	$[R_\odot]$	0.202 ± 0.024
R_{comp}	$[R_\odot]$	0.281 ± 0.033
$log(g)$ (sdB, spec)	$[\frac{cm}{s^2}]$	5.34 ± 0.20
$log(g)$ (sdB, phot)	$[\frac{cm}{s^2}]$	5.49 ± 0.11

5.8 Pn23l1-18

5.8.1 Radial velocity curve

Eighty spectra of Pn23l1-18 were recorded at La Palma using the IDS spectrograph. All of the spectra were taken with the R400V grating offering a large unvignetted wavelength range and a resolution of $R = 1592$ at $\lambda = 4500$ Å. Unfortunately, the first IDS spectra, which were analyzed with SPAS, were very noisy so that we could not derive viable results for their radial velocities. To increase the S/N ratio and derive RV values with lower uncertainties, we coadded four consecutively recorded spectra by using ISIS. Usually, spectra were firstly RV corrected before they get coadded to prevent a smearing of the absorption lines. In this case, we didn't, because the spectra, that were coadded, possess short exposure times and are immediately consecutively recorded, so that the effect of smearing is expected to be negligible. Some of the spectra could not be used for coadding because they did not exhibit an sdB star spectrum. Overall, we obtained 22 coadded spectra which could be used for further analysis.

The spectra of Pn23l1-18 show a large number of pronounced hydrogen Balmer lines and shallower helium lines. Since the hydrogen Balmer lines were perfectly fitted by SPAS and the spectra obtained enough lines of the Balmer series, the helium lines were rarely used to measure the radial velocities of the spectra. The times of the coadded spectra are derived by:

$$\frac{1}{n}\sum_{i=1}^{n} t_i (S/N)_i \qquad (16)$$

where n is the number of coadded spectra, t the time (in BJD), and S/N the S/N ratio of the individual spectra. The radial velocities were then barycentrically corrected. Their values as well as the related uncertainties are given in Table 20.

Table 20: Radial velocities of Pn23l1-18 received from the coadded INT IDS spectra. The RVs were determined by using SPAS. In the last column the absorption lines of each spectrum, that were used for calculating the radial velocities, are listed.

BJD	v_{rad} $[\frac{km}{s}]$	Δv_{rad}	used lines
2457654.49622101	70	30	H_γ-H_{10}, He I 4471
2457654.50562661	32	10	H_β-H_9
2457654.51992252	2	12	H_β-H_8
2457654.53578025	-51	9	H_β-H_ε
2457654.55256049	-76	8	H_β-H_8
2457654.57297216	-83	10	H_β-H_8
2457654.59146202	-61	12	H_β-H_8
2457654.60726123	-26	9	H_β-H_9
2457654.62057500	-17	16	H_β-H_8, He I 4471
2457654.63911053	40	18	H_β-H_8
2457655.61108552	-79	17	H_β-H_8
2457655.62026888	-95	8	H_β-H_9
2457656.47037293	-88	7	H_β-H_8
2457656.48419735	-74	8	H_β-H_8
2457656.49962185	-63	9	H_β-H_8
2457656.50854264	-55	13	H_β-H_8
2457656.54171394	13	9	H_β-H_8
2457656.55438206	42	8	H_β-H_8
2457656.57049774	70	10	H_β-H_8
2457656.60882559	52	12	H_β-H_8
2457656.62432879	29	8	H_β-H_8
2457656.63764649	-9	12	H_β-H_8 w.o. H_ε

By using the barycentric corrected RVs of Pn23l1-18, we could determine the radial velocity curve of the system. As seen before, a sine curve was fitted to the measured RVs yielding
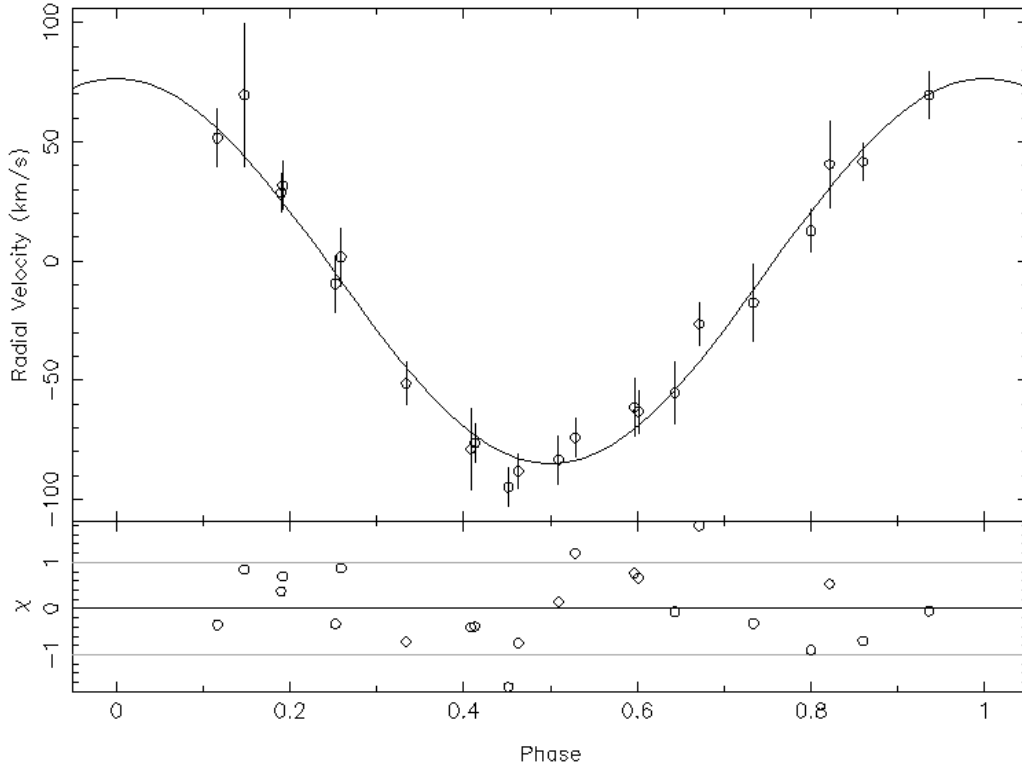
Figure 33: Plot of the phased radial velocity curve of Pn 23l1-18. Furthermore, the sinusoidal fit function is displayed. In the bottom panel the residuals are shown.

$K_1 = 80.8 \pm 2.8 \frac{km}{s}$ and $\gamma_1 = -4.1 \pm 1.7 \frac{km}{s}$. Fig. 33 displays the shape of the fitted sine curve and shows also the measured radial velocities of Pn23l1-18. Obviously, the sinusoid matches well with most of the data points even though the fit lays not inside the error range of some RV points. Nevertheless, we obtained the lowest uncertainties for semiamplitude and systems velocity for Pn23l1-18 of all systems analyzed in this work.

5.8.2 Quantitative spectral analysis

Since the IDS spectra are offering a large spectral range, many hydrogen Balmer and helium lines can be found in the spectra of Pn23l1-18 so that these spectra are suited for the quantitative spectral analysis. As before, the coadded spectra were used. Fig. 34 shows the fit of synthetic spectra to the recorded absorption lines of a coadded IDS spectrum. Since the IDS spectra are less accurate in the UV range, the hydrogen Balmer lines of higher transitions (H_{10} and higher) were not regarded for the determination of the atmospheric parameters. Again, the derived results of the three parameters, which were calculated foreach of the coadded spectra by using SPAS, were averaged. We obtained that the primary of Pn23l1-18 has an effective temperature of $T_{eff} = 29100 \pm 900$ K, a surface gravity of $log(g) = 5.61 \pm 0.09$, and a helium abundance of $log(y) = -2.25 \pm 0.10$ indicating a typical helium-poor sdB star. These results as well as the values, which were derived for the individual, coadded spectra, are given in Table 21.

On closer consideration of the values of the three atmospheric parameters listed in Table 21, it was conspicuous that the effective temperature of the primary star is systematically varying, while such trends can't be found for surface gravity or helium abundance.
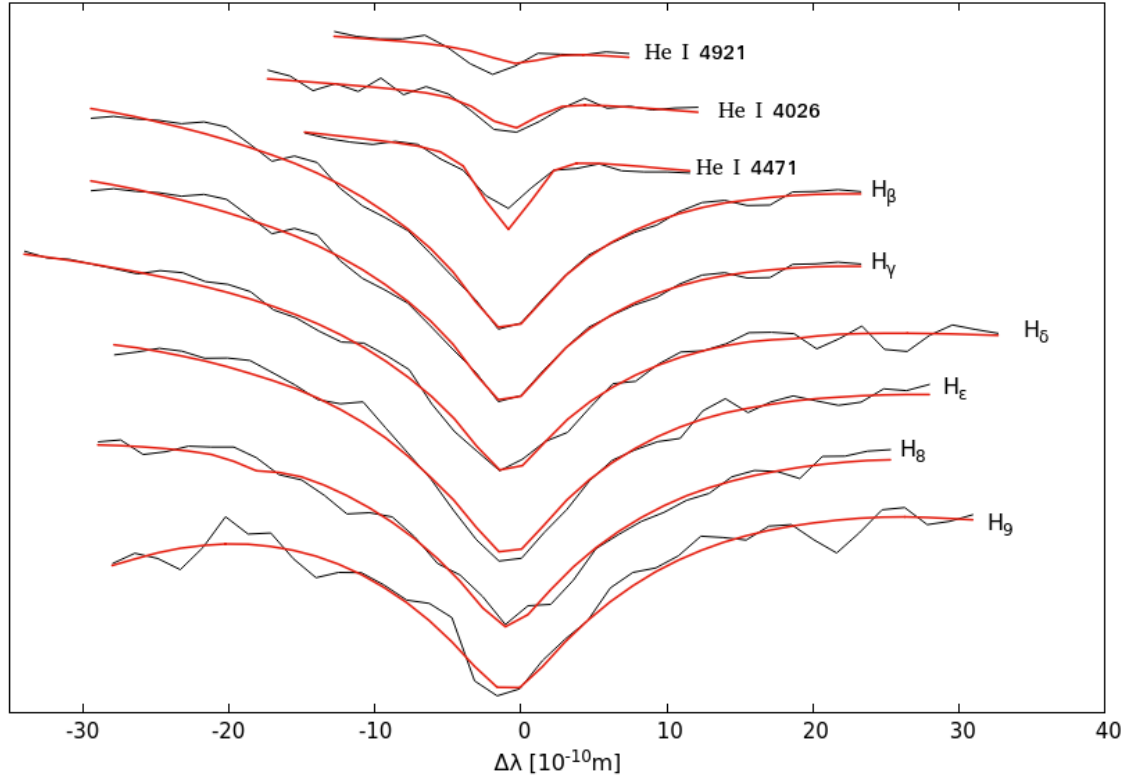

Figure 34: Example fit to the absorption lines of an individual IDS spectrum of Pn23l1-18 to determine the atmospheric parameters. The synthetic spectra were calculated from LTE model atmospheres developed by Heber et al. (2000).

Table 21: Atmospheric parameters of Pn23l1-18. Their values were determined with SPAS using the INT IDS spectra. The bottom line shows the averaged values of the three atmospheric parameters as well as the related standard deviation.

BJD	T_{eff} [K]	$\log(g)[\frac{cm}{s^2}]$	$\log(y)[\frac{n_{He}}{n_H}]$
2457654.49622101	28583	5.41	-2.35
2457654.50562661	28817	5.75	-2.49
2457654.51992252	27895	5.49	-2.38
2457654.53578025	28294	5.66	-2.24
2457654.55256049	28137	5.70	-2.20
2457654.57297216	28982	5.67	-2.14
2457654.59146202	29881	5.62	-2.24

Table 21: (continuation)

2457654.60726123	29827	5.48	-2.36
2457654.62057500	30180	5.66	-2.32
2457654.63911053	30484	5.61	-2.28
2457655.62026888	28458	5.69	-2.15
2457656.47037293	28756	5.60	-2.19
2457656.48419735	29448	5.61	-2.32
2457656.49962185	29887	5.63	-2.27
2457656.50854264	30244	5.70	-2.18
2457656.54171394	29740	5.50	-2.32
2457656.55438206	29757	5.63	-2.15
2457656.57049774	29227	5.66	-2.23
2457656.60882559	28588	5.59	-2.21
2457656.62432879	27902	5.52	-2.06
2457656.63764649	27207	5.70	-2.24
Average & stand. dev.	29100 ± 900	5.61 ± 0.09	-2.25 ± 0.10

This first proving of the data from Table 21 could not clarify whether this trend is real and depends on orbital phase or is randomly occurring due to the large standard deviation of the effective temperature. To check this, we had to phase the data. Therefor, we used the orbital period which was determined from the light curve under the usage of the LombScargle method (see 5.8.3). After the effective temperatures were phased, we could plot them in a Φ-T_{eff} diagram and fit a sinusoidal function to the data by using gnuplot (see Fig. 35).

For the fit, the general term of the sinusoid was used: $f(x) = a \cdot sin(b \cdot x + c) + d$. Since the period of the sine shall coincide with one orbital phase, the parameter b was set to 2π. The other three parameters were free and could be adjusted by gnuplot. As seen in Fig. 25, we derived a remarkable temperature variation with the phase reaching its minimum at $\Phi \approx 0.25$ and its maxmimum a half term later. Compared with the radial velocity curve of the primary, the temperature minimum occurs at the first inflection point of the RV curve, where the sine curve is monotonically decreasing (see Fig. 33). Consequently, the primary has its maximum effective temperature at the second inflection point which marks the upper conjunction.

We obtained the following results for the three, free parameters: $a = 1160 \pm 100$ K, $c = -3.10 \pm 0.09$, and $d = 29044 \pm 72$ K. Obviously, the displacement of the sinusoidal function in y-direction matches well with the averaged value for T_{eff} which we had derived by spectroscopic analysis with SPAS. The amplitude of the variation is with more than 1100 K quite large so that

the difference between maximal and minimal effective temperature (peak-to-peak amplitude) amounts to more than 2300 K.
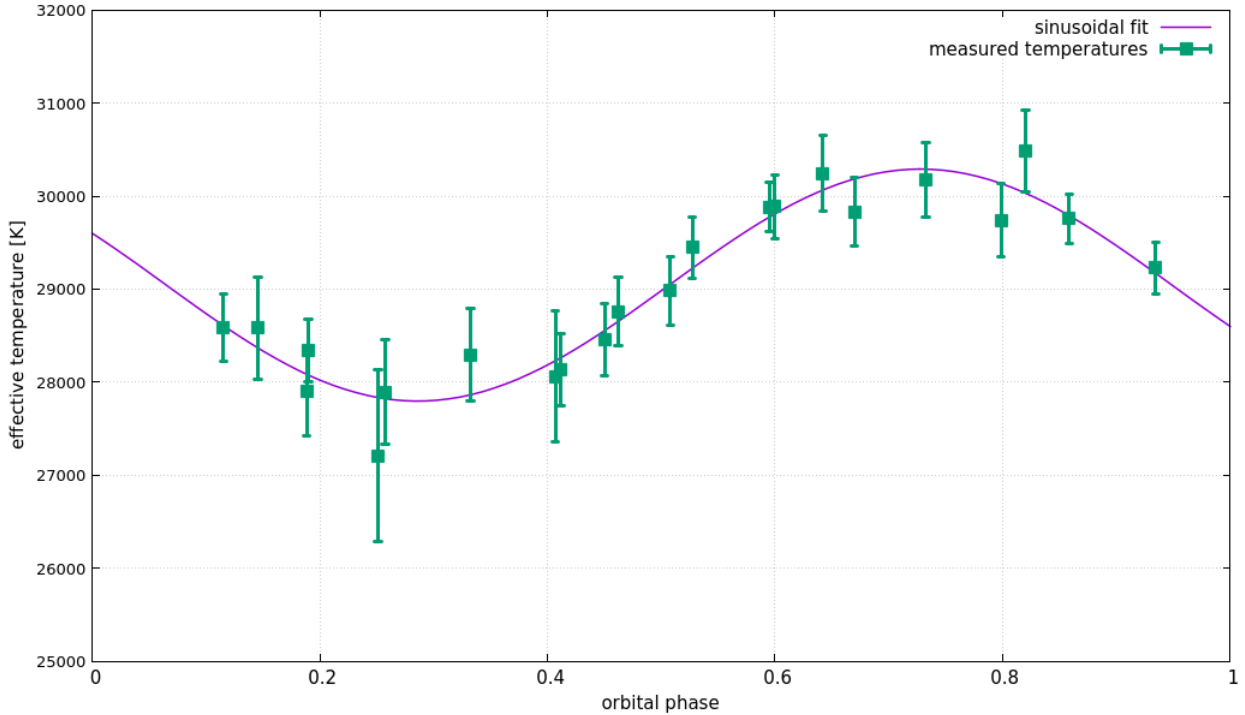

Figure 35: Plot of Pn23l1-18's effective temperature variation with orbital phase. To determine the magnitude of the variation, a sinusoidal funtction was fitted to the measured temperatures by using gnuplot.

5.8.3 Light curve analysis

In contrast to the three previously described OGLE binary stars, the light curve of Pn23l1-18 was recorded by the Catalina Sky Survey with the 0.7m telescope offering 371 single measurements of the systems magnitude. The original data obtain the observed time in MJD, the measured magnitude, and the magnitude's uncertainty. Since Pn23l1-18 is just slightly brighter than PG 2259+134, the magnitudes' errors are of similar size, but larger than for the three OGLE systems. A first plot of the not-phased data on the CSS DR2 webpage gives already a hint of that this system is eclipsing, because significantly fainter magnitudes of the system were measured as displayed in Fig. 36. As one may see there, the range between the usual magnitude of the system and the faintest measurements exhibit also several observed data points, which is why this behavior has to be a real trend of the system's magnitude.

As described for PG 2259+134, we had to phase and normalize the light curve of the system again. Therefor, the orbital period, which was given at the CSS webpage, was used ($P = 0.2119061$ d).[14]   But, if we tried to phase the light curve by using this given period,

---

[14]http://nesssi.cacr.caltech.edu/cgi-bin/getcssconedb_id_phase.cgi?ID=1112124025089&
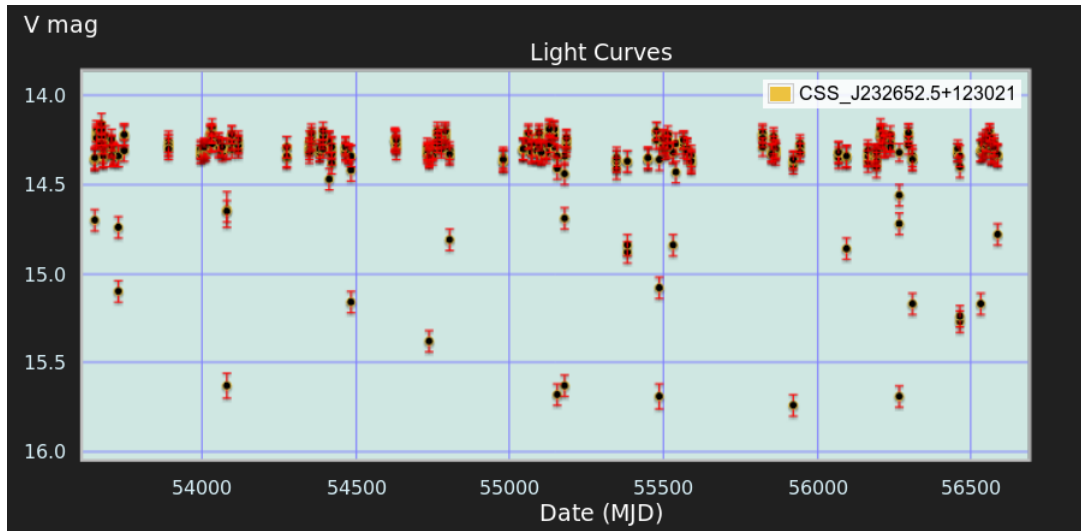PLOT=plot; last access on: 03.04.18

Figure 36: Appearance of the original CSS photometry data of Pn23l1-18 as it is shown on the CSS data release 2 webpage.[15] The magnitude is plotted against the observation date in MJD.

we obtained a badly shaped primary minimum because most of the values differ largely from their usual position on the inverse Gaussian bell (see left picture of Fig. 37). For this reason, we thought the quoted period on the CSS webpage is not accurate enough and, hence, wrote a Python script to determine precisely the orbital period of the binary system by using the Lomb-Scargle method. Although several modes of the LombScargle were tested, we did not find a solution for *P* that would give us the wanted shape of the primary eclipse. The best-fit solution
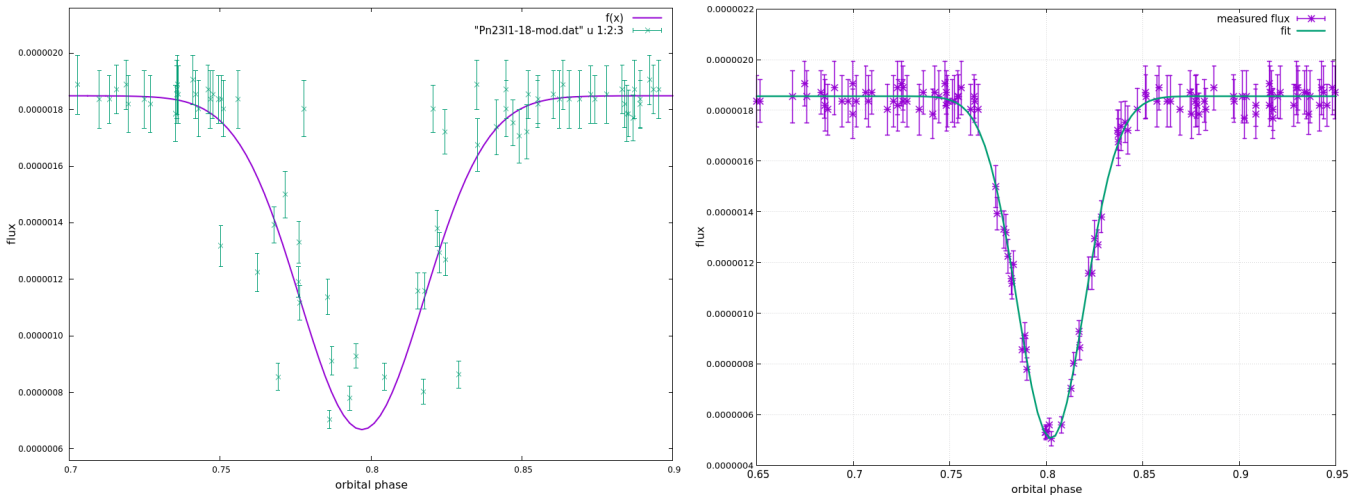
Figure 37: Left: Plot of the measured, not barycentric corrected flux of Pn23l1-18 in the orbital phase of $\Phi = 0.7$ and 0.9 and a Gaussian function, which was fitted to the primary minimum in this range. Right: The same situation is shown, but here the measured data points are barycentrically corrected. It is obvious that Gaussian function and recorded light curve match significantly more than before.

derived by the LombScargle method was $P = 0.211905669$ d - this is corresponding to a difference of 0.037 s to the orbital period given by CSS. Consequently, this could not be the crucial effect which is causing the abnormal shape of the primary eclipse. On closer examination of the data, we found out that the observational times of the data were not helio- or barycentric corrected, but are given in MJD. Since the photometric data of Pn23l1-18 were recorded for more than ten years, the deficiency of a barycentric correction may cause a distortion of the eclipse. For the correction, again, a Python script was written and adapted to the data. As displayed in the right plot of Fig. 37, the primary eclipse of the barycentric corrected light curve matches smoothly with the Gaussian function as usual.

For further analysis of the phased, barycentric corrected, and normalized light curve, the mass ratio q had to be constrained and the minimal inclination determined. We obtained $i_{min} = 81.15°$ and a mass ratio interval ranging from $q = 0.357$ to 0.367. As before, some parameters were fixed as seen in Table 22 and the derived mass ratio range was stepped through in 0.001 steps. For each mass ratio value of the given interval, a large number of synthetic light curves was fitted to the observed photometric data by varying the free parameters' start values. Since the light curve of Pn23l1-18 was not recorded during one night, but during a decade, we were not able to derive the ephemeris precisely.

Table 22: Best-fit model parameters of the light curve for $q = 0.366$ calculated by MORO.

Fixed parameters			
Gravitational darkening exponent	g_1		1.000
	g_2		0.320
Primary's effective temperature	$T_{\text{eff,prim}}$	[K]	29100
Bolometric albedo	A_1		1.000
Radiation pressure parameter	δ_2		0.000
Limb darkening coefficient	x_1^{a}		0.190
Fraction of third light	l_3^{b}		0.000
Central wavelength	λ	[mm]	0.550
Adjusted parameters			
Inclination	i	[°]	85.7291 ± 0.0022
Secondary's effective temperature	$T_{\text{eff,sec}}$	[K]	3760 ± 310
Bolometric albedo	A_2		3.043 ± 0.016
Roche potential	Ω_1		7.964 ± 0.008
	Ω_2		3.8788 ± 0.0005
Radiation pressure parameter	δ_1		0.0012 ± 0.0013
Relative luminosity	$\frac{L_1}{L_1+L_2}^{\text{c}}$		0.9982 ± 0.0009

Table 22: (continuation)

Limb darkening coefficient	$x_2(\lambda_1)$		0.9991 ± 0.0009
Related Roche radii			
	$r_{1,\text{pole}}$	[a]	0.13139 ± 0.00005
	$r_{1,\text{point}}$	[a]	0.13178 ± 0.00005
	$r_{1,\text{side}}$	[a]	0.13160 ± 0.00005
	$r_{1,\text{back}}$	[a]	0.13175 ± 0.00005
	$r_{2,\text{pole}}$	[a]	0.14233 ± 0.00003
	$r_{2,\text{point}}$	[a]	0.14501 ± 0.00010
	$r_{2,\text{side}}$	[a]	0.14310 ± 0.00003
	$r_{2,\text{back}}$	[a]	0.14473 ± 0.00003

Comments:

[a] see Wade & Rucinski (1985)

[b] Previously done test fits showed no indication for a third light.

[c] L_2 isn't a completely indipendent parameter, but rather gets recomputed by r_2 and $T_{\text{eff,sec}}$.

As for all the previously discussed systems, no unique best-fit solution could be found for Pn23l1-18. The values of the standard deviation are about 20% larger than of OGLE 416194, but also about 20% lower than of PG 2259+134. Hence, our best-fit solution was again adopted on the basis of a list in which the solutions are sorted to their σ_{fit} values. We received that $q = 0.366$ was most frequently placed at the top of the list occurring seven times under the first ten positions. The values of the adjusted parameters were calculated by averaging the results of the eight runs with $q = 0.366$ which had the best quality and the lowest σ_{fit} values. The derived results for the free parameters are given in Table 22.

Compared to the OGLE stars, the relative luminosity is slightly closer to 1 indicating a much fainter companion (relatively to the primary star). The inclination of the system was found to be $85.7291 \pm 0.0022°$. The error is of statistical nature and, since the eight solutions, which were used here, possess very similar values for the inclination, the standard deviation became unrealistically low. As before, the bolometric albedo of the secondary is largely extending 1, but not as much as for the OGLE stars where the values exceeded 7. The synthetic light curve of the run with the lowest σ_{fit} fits very well to the measured data displayed in Fig. 38. The light curve shows distinct primary and secondary eclipses and a periodic flux variability which are caused by the reflection effect. The primary minimum is very pronounced descending to less than 30% of the flux at phase 0.25. The determined high inclination angular coincides well with the deep primary eclipse. Furthermore, the strong decrease of the flux during the first eclipse indicates a large companion, that should be of similar size as the hot subdwarf star. By

using the mass function, the third law of Kepler, and the results obtained from spectroscopy and photometry, we could determine the radii of the stars, their separation, as well as the secondary's mass to be: $R_{sdB} = 0.170 \pm 0.008 R_\odot$, $R_{comp} = 0.185 \pm 0.009 R_\odot$, $a = 1.29 \pm 0.06 R_\odot$, and $M_2 = 0.168 \pm 0.007 M_\odot$. Hence, the results of the radii match exactly with the predicted
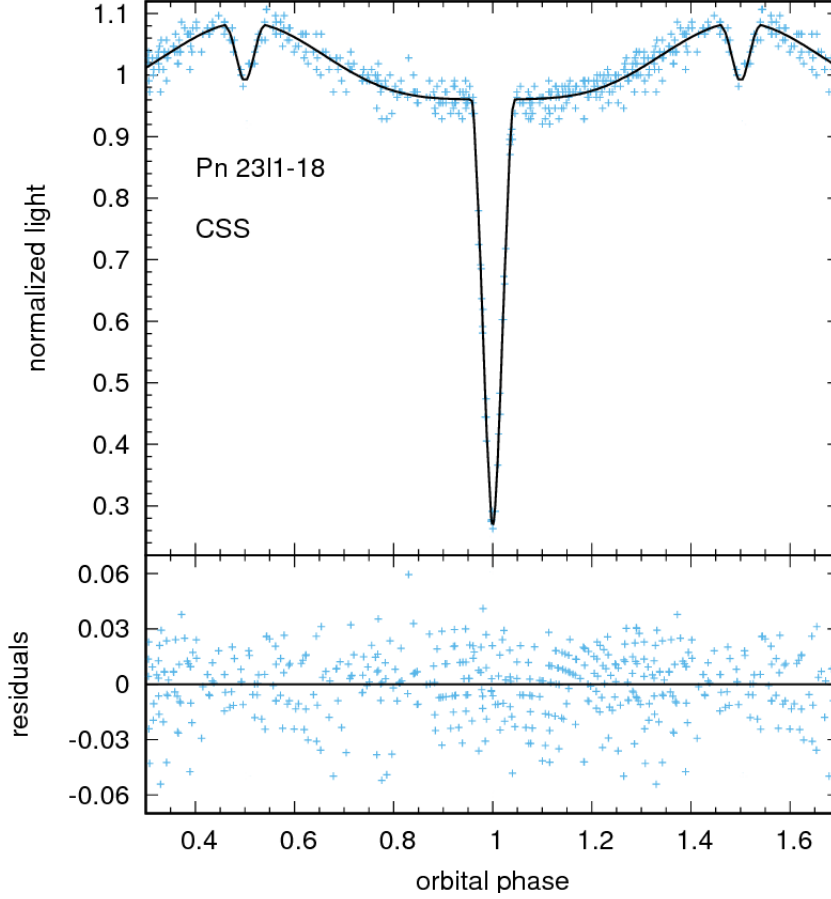

Figure 38: Plot of the phased and fitted CSS light curve of the Pn23l1-18. Primary and secondary minima as well as the reflection effect are clearly recognisable. The residuals are shown in the bottom panel.

assumptions. With the help of the obtained mass and radius of the secondary, we can classify the companion as an M-dwarf. Overall, the derived results are revealing that Pn23l1-18 is an eclipsing, short-periodic binary system consisting of an sdB and an M-dwarf. For this reason, Pn23l1-18 meets the requirements of a HW Vir system.

To prove the consistency of the spectroscopic and photometric analysis, one can also calculate the suface gravity from photometric results and compare its value with the result derived from quantitative spectroscopy. By using Eq. (12), we obtained: $log(g)_{phot} = 5.65 \pm 0.05$. Obviously, both values are within their respective error ranges. The results of Pn23l1-18 derived by spectroscopic and photometric analysis are summarized in Table 23.

Table 23: Parameters of Pn23l1-18 that were derived by spectroscopic and photometric analysis. The errors of the radii and the separation were calculated by using the Gaussian error propagation.

Pn23l1-18		
$T_{\text{eff,sdB}}$	$[K]$	29100 ± 900
K_1	$[\frac{km}{s}]$	80.8 ± 2.8
i	$[°]$	85.7291 ± 0.0022
M_{sdB}	$[M_\odot]$	0.47
M_{comp}	$[M_\odot]$	0.168 ± 0.007
a	$[R_\odot]$	1.29 ± 0.06
R_{sdB}	$[R_\odot]$	0.170 ± 0.008
R_{comp}	$[R_\odot]$	0.185 ± 0.009
$log(g)$ (sdB, spec)	$[\frac{cm}{s^2}]$	5.61 ± 0.09
$log(g)$ (sdB, phot)	$[\frac{cm}{s^2}]$	5.65 ± 0.05

5.9 EC 20323-4648 – the HW Vir with the longest period ever reported

5.9.1 Radial velocity curve

Last but not least, we want to analyze the binary star system EC 20323-4648. For spectroscopic analysis, seven spectra were taken with the NTT telescope and the EFOSC2 spectrograph whereof six spectra were recorded by using grism 19. Hence, six spectra could be used to determine the radial velocity curve, while one spectrum is suited for the quantitative spectral analysis. Unfortunately, one of these spectra is not showing a hot subdwarf star's spectrum so that the radial velocities of only five spectra could be determined. As before, SPAS was used to derive the RVs of the individual spectra. The obtained RVs as well as the related observation times were barycentrically corrected and are given in Table 24. Beside this, the uncertainties of the RVs and the used absorption lines are listed.

Table 24: Radial velocities of EC 20323-4648 received from NTT EFOSC2 spectra. The RVs were determined by using SPAS. In the last column, the absorption lines of each spectrum, that were used for calculating the radial velocities, are listed.

BJD	v_{rad} $[\frac{km}{s}]$	Δv_{rad}	used lines
2457937.6749527	-15	17	H_β, He I 4471
2457937.8406704	-49	9	H_β, He I 4921

Table 24: (continuation)

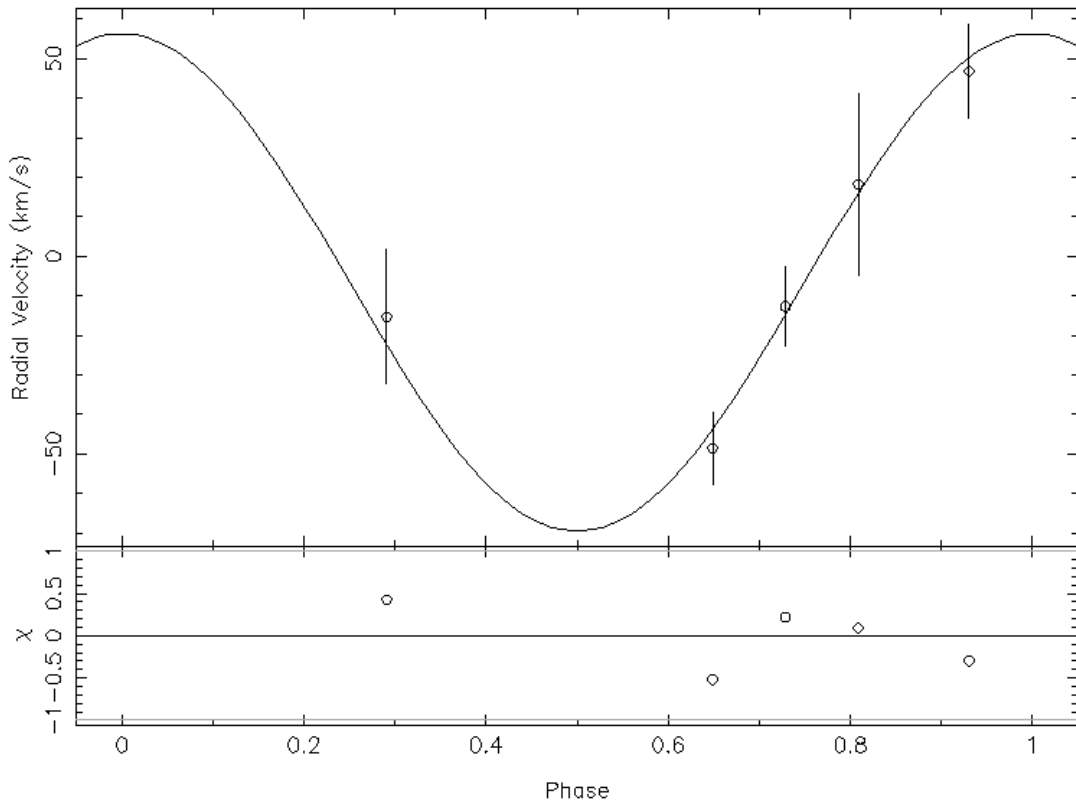| 2457937.8777961 | -13 | 10 | H_β, He I 4471 |
| 2457937.9147565 | 18 | 23 | H_β, He I 4471, He I 4921 |
| 2457938.8972802 | 47 | 12 | H_β, He I 4471 |

Figure 39: Plot of the phased radial velocity curve of EC 20323-4648 and of the related sinusoidal fit function. In the bottom panel the residuals are shown.

By using the barycentric corrected radial velocities, we are able to determine the related RV curve to EC 20323-4648. As usual, the interactive ISIS script was used firstly phasing the data, before it fits a sine curve to them. Again, the period, known from photometry, was fixed ($P = 0.4630668$) and the eccentricity e was set to zero due to the short orbital period of the system. Because of the large errors and the less number of RV measurements, the fitted sinusoid matches very precisely to the observed data (see Fig. 39) resulting in a very low reduced χ^2 of 0.2409401. Considering this for the calculation of the uncertainties, we obtained $K_1 = 62.9 \pm 4.8 \frac{km}{s}$ and $\gamma_1 = -6.6 \pm 3.5 \frac{km}{s}$, which are quite normal values for sdB binary stars.

5.9.2 Quantitative spectral analysis

Only one of the seven spectra, that were taken of EC 20323-4648, was recorded with grism 7 so that it is adapted for the determination of the atmospheric parameters. The spectrum exhibits the typical appearance of an sdB-type star owning strong hydrogen Balmer lines and shallower helium lines. As before, the program SPAS was used for the quantitative spectral analysis calculating synthetic spectra by means of LTE model atmospheres from Heber et al. (2000) which were then fitted to the measured absorption lines. Fig. 40 shows the fit of a synthetic spectrum to the only measured spectrum of EC 20323-4648.
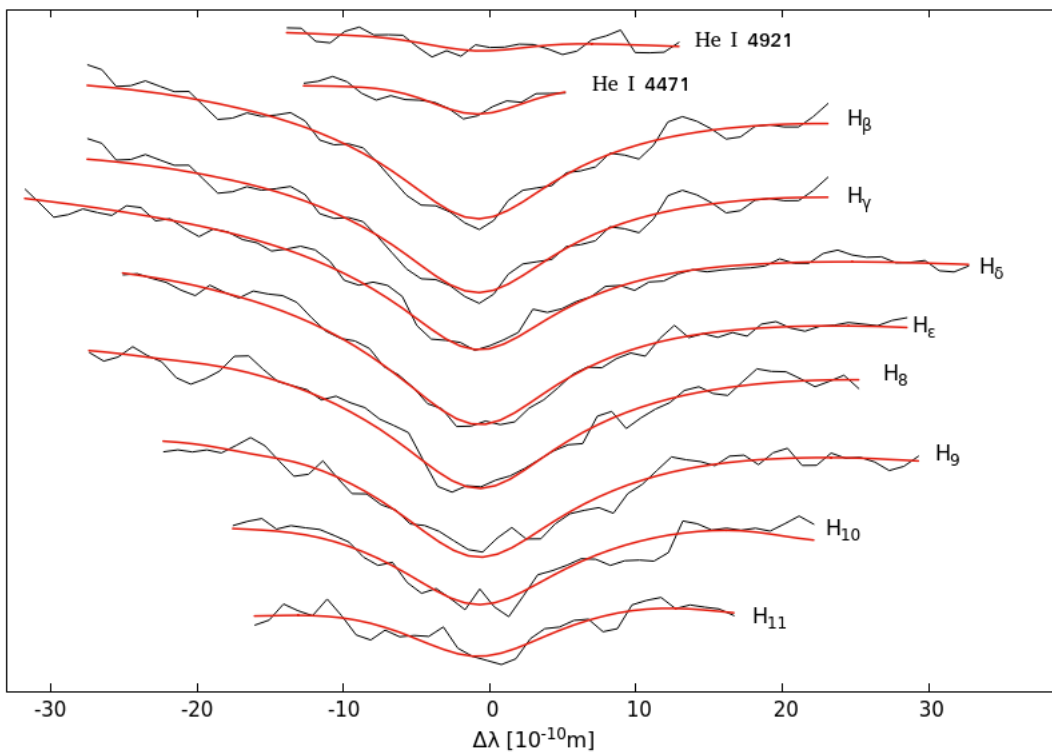
Figure 40: Example fit to the absorption lines of an individual EFOSC2 spectrum of EC 20323-4648 in order to determine the atmospheric parameters. The synthetic spectra were calculated from LTE model atmospheres (Heber et al., 2000).

For the quantitative spectral analysis of EC20323-4648, we could use all hydrogen lines from H_β to H_{11} as well as the weak helium lines at 4471 Å and 4921 Å. The results derived with SPAS are given in Table 25. Since only one spectrum was available to determine the atmospheric parameters, we could not calculate the uncertainties in the usual way. Rather, the given errors are determined by SPAS under the usage of a bootstrapping method. All the three parameters are indicating that the primary of the binary system EC 20323-4648 is a helium-poor sdB star. While the errors of the effective temperature and the surface gravity are quite low, the helium abundance shows a large uncertainty originating in too few and noisy helium lines (see Fig. 40).

Table 25: Atmospheric parameters of EC 20323-4648. Their values were determined with SPAS using the NTT EFOSC2 spectra.

BJD	T_{eff} [K]	$\log(g)$ [$\frac{cm}{s^2}$]	$\log(y)$ [$\frac{n_{He}}{n_H}$]
2457936.91857955	28400 ± 400	5.44 ± 0.06	-2.36 ± 0.33

5.9.3 Light curve analysis

As for Pn23l1-18, the light curve of EC 20323-4648 was recorded by the Catalina Sky Survey using a 0.7m telescope in the Arizona mountains. 313 several measurements of the system's magnitude were taken. Compared to Pn23l1-18, 16% less photometric data of EC 20323-4648 are available and the system is fainter possessing a 0.6 larger magnitude than Pn23l1-18. Furthermore, a few outliers could be found in the data, which had to be removed so that the number of suitable measurements was further reduced. As described before, the light curve had to be phased, barycentrically corrected, and normalized again. With the help of the LombScargle method, we derived the orbital period of the system to be $P = 0.463073891$ d which is the largest period observed in this work. To barycentrically correct the data, the previously described Python script was used resulting to the typical shape of the primary eclipses as displayed in Fig. 41. Since the system is fainter than Pn23l1-18, the uncertainties were larger so
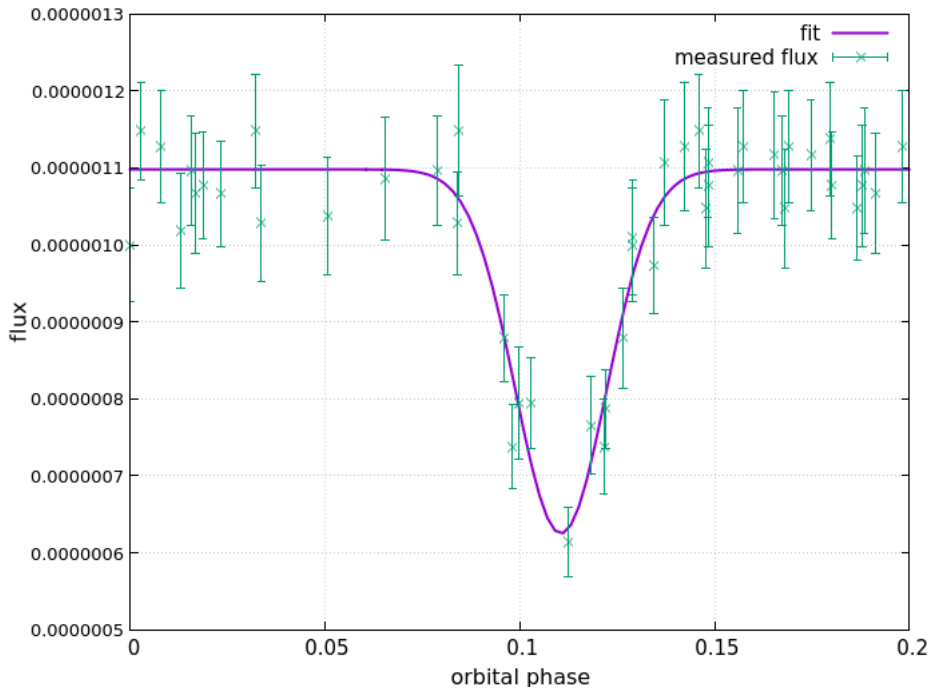
Figure 41: Determination of the minimum of the light curve's primary eclipse with the help of an inverse Gaussian function fitted the data.

that the values do not fit as precise to the inverse Gaussian function as seen for the primary

eclipse of Pn23l1-18. Besides the primary eclipse, the light curve of EC 20323-4648 further exhibits a secondary minimum which is not clearly visible in the observed data because they are not accurate enough. Furthermore, a slight periodic variation can be seen in the light curve caused by the reflection effect (see Fig. 42). Since EC20323-4648 has a long orbital period with respect to the other, previously discussed systems, the reflection effect is much weaker than for the other binaries. The primary minimum is pronounced, but not as deep as for the other systems. Therefor, several reasons are possible: Firstly, the companion could be smaller than the sdB star so that only some parts of the hot star's disc are covered during the eclipse. Additionally, the effect could have its origin in inclination. Due to the long period and the thereof resulting large separation between the two components, the inclination angle must be quite high because otherwise no eclipses could be detected. However, the long period ensures that smaller deviation of $90°$ have larger effects on the extent of the occultation. In reality, we will probably have a combination of both effects.

Before we started the light curve analysis with MORO, we had to normalize the light curve. Therefore, the measured flux was set to 1 at phase 0.25. Furthermore, the mass ratio had to be constrained and the minimum inclination to be found. We derived $i_{min} = 84.76°$; the mass ratio interval ranges from $q = 0.360$ to 0.368. As discussed a few times, we fixed some parameters at values that were known from theory or spectroscopy (see Table 26) and stepped through the mass ratio range in 0.001 steps so that a large grid of synthetic light curves was calculated for EC 20323-4648. First trials showed an inadequate fit of the light curve which was most likely caused by the scattered data around the eclipses so that they could not be accurately fitted. For this reason we decided to weight trustworthy values higher than measurements, that were far away from their usual position. By doing so, we could decrease the standard deviation of the fits.

Again, no unique solution could be found for a system's light curve. Compared to the other systems the σ_{fit} values are larger originating from the scattered data and unprecise measurements. However, we used the normal procedure to determine a best-fit solution. With the help of our Python script, we found $q = 0.363$ to be most frequently at the top of the list showing the runs with the lowest standard deviation values. The final results of the light curve analysis performed with MORO are the averaged values of the seven best-fit solutions and are given in Table 26. The displayed uncertainties of the adjusted parameters are the calculated standard devations.

Table 26: Adopted light curve solution for $q = 0.363$

Fixed parameters			
Gravitational darkening exponent	g_1		1.000
	g_2		0.320
Primary's effective temperature	$T_{\text{eff,prim}}$	[K]	28400
Bolometric albedo	A_1		1.000

Table 26: (continuation)

Radiation pressure parameter	δ_2		0.000
Limb darkening coefficient	x_1^{a}		0.190
Fraction of third light	l_3^{b}		0.000
Central wavelength	λ	[mm]	0.550

Adjusted parameters			
Inclination	i	[°]	86.511 ± 0.004
Secondary's effective temperature	$T_{\text{eff,sec}}$	[K]	3240 ± 830
Bolometric albedo	A_2		4.58 ± 0.11
Roche potential	Ω_1		8.78 ± 0.02
	Ω_2		5.837 ± 0.003
Radiation pressure parameter	δ_1		0.0026 ± 0.0022
Relative luminosity	$\frac{L_1}{L_1+L_2}^{\text{c}}$		0.9995 ± 0.0008
Limb darkening coefficient	$x_2(\lambda_1)$		1 ± 0

Related Roche radii			
	$r_{1,\text{pole}}$	[a]	0.11846 ± 0.00004
	$r_{1,\text{point}}$	[a]	0.11871 ± 0.00004
	$r_{1,\text{side}}$	[a]	0.11859 ± 0.00004
	$r_{1,\text{back}}$	[a]	0.11869 ± 0.00004
	$r_{2,\text{pole}}$	[a]	0.08029 ± 0.00005
	$r_{2,\text{point}}$	[a]	0.08050 ± 0.00007
	$r_{2,\text{side}}$	[a]	0.08036 ± 0.00004
	$r_{2,\text{back}}$	[a]	0.08053 ± 0.00005

Comments:

[a] see Wade & Rucinski (1985)

[b] Previously done test fits showed no indication for a third light.

[c] L_2 isn't a completely indipendent parameter, but rather gets recomputed by r_2 and $T_{\text{eff,sec}}$.

We received an inclination of $i = 86.511 \pm 0.04°$. The error is unrealistically low because of its statistical nature and the seven solutions, which were used to derive the results of the free parameters, possessed similar values of inclination. Again, we obtained a light curve fit with a secondary's bolometric albedo way above 1. The relative luminosity is very close to 1 indicating a very faint companion. Compared to Pn23l1-18, which had a relative luminosity of

0.9982, the companion of EC 20323-4648 has to have a 70% lower intensity than Pn23l1-18's companion. The Roche radii of the stars do not indicate ellipsoidal deformations.

Using the mass function and Kepler's law und plugging in the obtained spectroscopic and photometric results, we derive the companion's mass, the stars separation, and their radii yielding $M_2 = 0.170 \pm 0.016 M_\odot$, $a = 2.17 \pm 0.23 R_\odot$, $R_{sdB} = 0.257 \pm 0.028 R_\odot$, and $R_{comp} = 0.175 \pm 0.019 R_\odot$. Considering the results derived for the secondary, this star can be classified as an M-
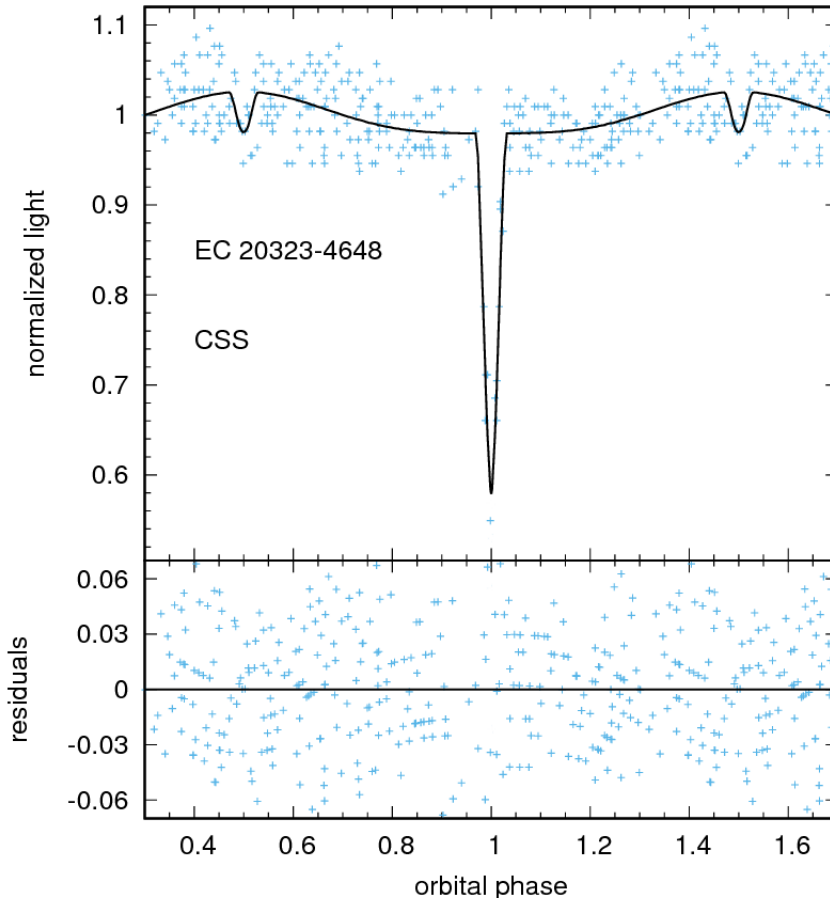
Figure 42: Plot of the phased and normalized fluxes and the synthetic light curve of the best-fit solution, which was derived by using MORO. Due to the relatively large orbital period, the reflection effect isn't as prominent as previously seen for the other HW Vir stars.

dwarf. As we had assumed by analysing the light curve's shape, the companion has a smaller radius than the sdB star and the inclination is slightly below 90°. Overall, we found EC 20323-4648 to be an eclipsing, short-periodic sdB+dM binary system, so that it can be classified as HW Vir. Very remarkable is the duration of one orbital period with respect to the derived periods of other HW Vir systems, which is by far the longest period of all currently known HW Vir systems (see Table A.1 for further information).

Again, we are able to calculate the surface gravity by using the photometric results in order to check the accordance of the photometric and spectroscopic analysis. We obtained $log(g)_{phot} = 5.29 \pm 0.10$ for the photometric surface gravity. Since we had only one low resolution spectrum

to derive the spectroscopic surface gravity, its error is definitely underestimated so that both results coincide well. Beside this, the most important results from our analysis are summarized in Table 27.

Table 27: Parameters of EC 20323-4648 that were derived by spectroscopic and photometric analysis. The errors of the radii and the separation were calculated by using the Gaussian error propagation.

EC 20323-4648		
$T_{\text{eff,sdB}}$	$[K]$	28400 ± 400
K_1	$[\frac{km}{s}]$	62.9 ± 4.8
i	$[°]$	86.511 ± 0.004
M_{sdB}	$[M_\odot]$	0.47
M_{comp}	$[M_\odot]$	0.170 ± 0.016
a	$[R_\odot]$	2.17 ± 0.23
R_{sdB}	$[R_\odot]$	0.257 ± 0.028
R_{comp}	$[R_\odot]$	0.175 ± 0.019
$log(g)$ (sdB, spec)	$[\frac{cm}{s^2}]$	5.44 ± 0.06
$log(g)$ (sdB, phot)	$[\frac{cm}{s^2}]$	5.29 ± 0.10

6 Summary and outlook

Finally, we can use the results from quantitative spectroscopic analysis, which were derived for all the seven binary systems to examine their position in a T_{eff}-$log(g)$-diagram and in a T_{eff}-$log(y)$-diagram as well and compare it with the currently known HW Vir systems. Firstly, the T_{eff}-$log(g)$-diagram shall be presented and discussed. Even if, PG 2259+134 was not distinctly classified as HW Vir system and MCT 0049-3059 could not be classified anyway, we treated them in this analysis as usual HW Vir systems and compare them with the previously reported systems too. The position of the seven systems, that were analyzed in this work, is displayed in Fig. 43 as well as the positions of the currently known HW Vir systems. The precise values
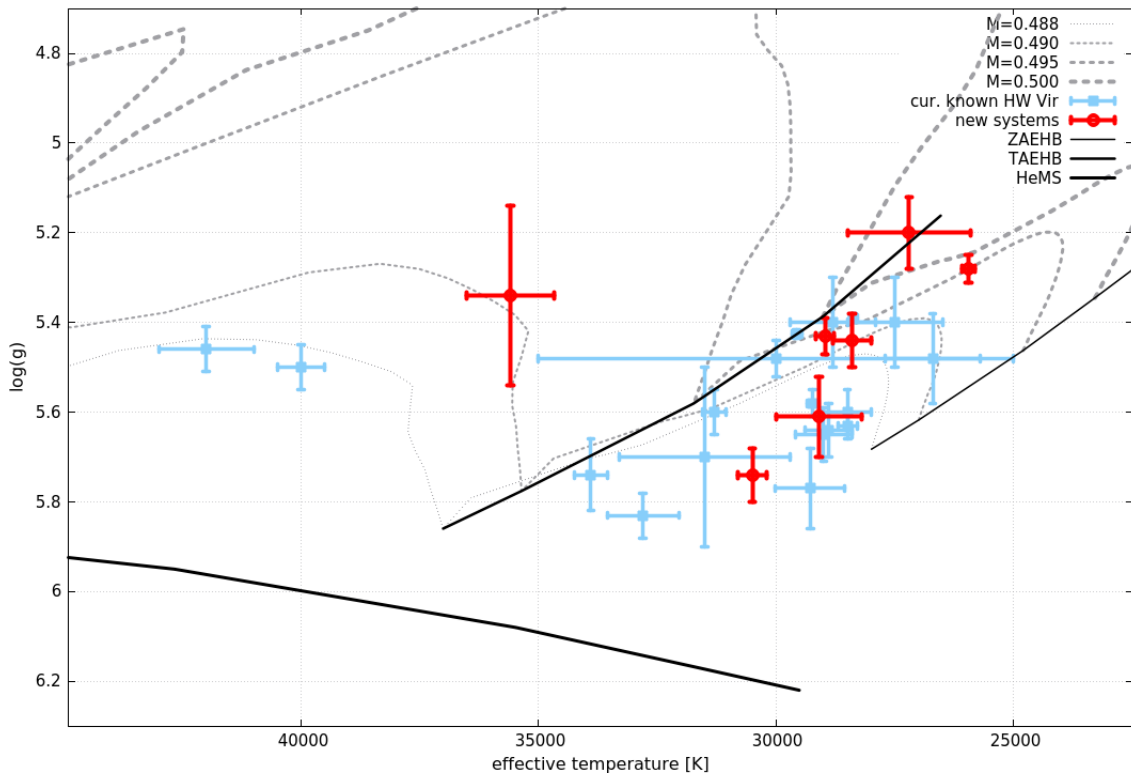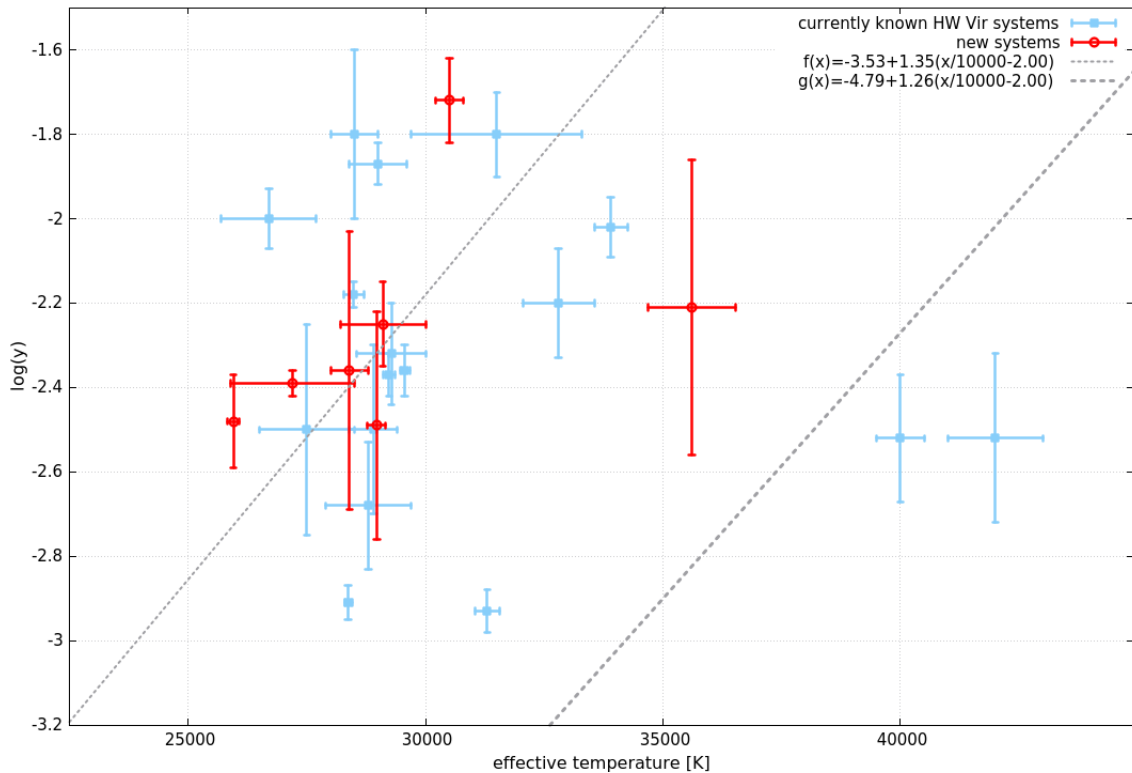

Figure 43: Position of the Hw Vir stars, which were presented in this work, and PG 2259+134 in a T_{eff}-$log(g)$ diagram. For better comparison, the currently known HW Vir systems are also shown. The dash dotted lines describe the extreme horizontal branch evolutionary models for various sdB star masses (Dorman et al., 1993). Additionally, the zero-age extreme horizontal branch (ZAEHB), the terminal-age extreme horizontal branch (TAEHB), and the helium main-sequence (HeMS) are illustrated.

and the related uncertainties of every system are listed in the appendix. As one can see in Fig. 43, most of the systems are located in the usual area between the zero-age extreme horizontal branch (ZAEHB) and the terminal-age extreme horizontal branch (TAEHB). The sdB of OGLE 173411 marks a new lower limit for the effective temperature of a HW Vir system's sdB. According to evolutionary models of Dorman et al. (1993), this may indicates a larger mass of the primary star than assumed. Very interesting is also the position of OGLE 361688's primary

star, which is slightly beyond the TAEHB portending that the sdB has fused almost its entire helium in its core. Probably, an alteration in the system's light curve and spectrum may be seen in the next thousands or ten thousands years. But most conspicuously should be the location of OGLE 416194 in the diagram defining a complete new possible region for HW Vir systems in the T_{eff}-$log(g)$ diagram. Most likely, the hot subdwarf is evolving to a star which is quite similar to the primary of AA Dor.

Furthermore, we are interested in the position of the primary stars of the analyzed systems in a T_{eff}-$log(y)$ diagram which are displayed in Fig. 44. Edelmann (2003) discovered a strong

Figure 44: Position of the Hw Vir stars, which were presented in this work, and PG 2259+134 in a T_{eff}-$log(y)$ diagram. The other HW Vir stars are displayed too. The dash dotted lines mark the relation which was found by Edelmann (2003) for the helium abundances of sdB stars.

coherence between the effective temperature and the helium abundance of sdB stars. In its PhD thesis, he could further show that the sdBs are separated into two different sequences showing different trends, where the minority of the sdB stars ($\sim 15\%$) has a significantly lower helium abundances than the rest. The two sequences can be approximately described by two linear regressions lines given by $f(x) = -3.53 + 1.35 \cdot \left(\frac{x}{10000} - 2.00\right)$ for the bulk and $g(x) = -4.79 + 1.26 \cdot \left(\frac{x}{10000} - 2.00\right)$ for the other sequence, where x is the effective temperature of the star. As seen in Fig. 44, most of our systems match well with the upper regression line as well as the majority of the currently known HW Vir does. Again, the exception is OGLE 416194's primary star which is positioned right between the regression lines. A possible explanation could be the circumstance that the primary was not distinctly identified as sdB star,

also the possibility of a sdOB star was revealed. Since these trends were only validated for sdB stars, they don't have any significance for sdOB stars.

In summary, five of the seven systems could be classified as new HW Vir systems increasing the number of currently known systems about 25%. Furthermore, a new sdB+dM system could be detected exhibiting a strong reflection effect in its light curve. Due to the noisy light curve, it could not be unequivocally resolved whether the system shows shallow eclipses or not. With MCT 0049+3059, another systems was spectroscopically analyzed, but since too few spectra were available to derive an expressive RV curve, no light curve analysis was performed. Very interesting systems were found and analyzed with OGLE 416194 and EC 20323-4648. While OGLE 416194 has a unique position in both, T_{eff}-$log(g)$ and T_{eff}-$log(y)$ diagram, EC 20323-4648 is the HW Vir system with the longest period and the largest separation ever described. Beside this, a detailed analysis with preciser data could doubtlessly prove, whether the companion of PG 2259+134 is a brown dwarf or a low massive M-dwarf close above the stellar limit. With Pn23l1-18, we found a HW Vir system showing a remarkable temperature variation with the phase in their spectra.

In the near future, many new HW Vir stars will be found and reported by the EREBOS project (Eclipsing Refletion Effect Binaries from the OGLE Survey) where astronomers examining the photometric OGLE data to eclipsing, short-periodic binary stars in order to find low-mass stellar or sub-stellar companions. For this reason, the project aims at recording and analysing time-series spectroscopy and photometric follow-up observations to derive the systems' atmospheric and orbital parameters (Schaffenroth et al., 2017). As described in Sect. 4.2, 111 HW Vir candidates were currently found by the EREBOS project, so that one can say already today the number of known HW Vir systems will be multiplied by this project. Consequently, three of the systems, that were described in this thesis, were found on this way.

Appendix

Table A.1: In this table the atmospheric parameters as well as the period of the known HW Vir systems and PCEBs with reflection effect consisting of an sdB and an M-dwarf or a B-dwarf are listed. The systems, that were firstly discussed in this thesis, are also included and printed in bolded. Their uncertainties are of statistical nature only.

System	Period [d]	T_{eff} [K]	log(g) [$\frac{cm}{s^2}$]	log(y) [$\frac{n_{He}}{n_H}$]	References
Currently known HW Vir Systems					
NSVS 07826247	0.16177042	29230 ±125	5.58 ±0.03	-2.37 ±0.05	1)
2M1938+4603	0.1257653	29564 ±106	5.425 ±0.009	-2.36 ±0.06	2)
NY Vir	0.101015999	31300 ±250	5.60 ±0.05	-2.93 ±0.05	3)
PTF1 J07245+1253	0.0998025	33900 ±350	5.74 ±0.08	-2.02 ±0.07	4)
HS 0705+6700	0.095646644	28800 ±900	5.40 ±0.10	-2.68 ±0.15	5)
HS 2231+2441	0.110588	28370 ±80.0	5.39 ±0.01	-2.91 ±0.04	6)
HW Vir	0.116719599	28488 ±208	5.63 ±0.03	-2.18 ±0.03	7), 8)
BUL-SC 16335	0.125050278	31500 ±1800	5.70 ±0.20	-1.80 ±0.10	9), 10)
EC 10246-2707	0.118507994	28900 ±500	5.64 ±0.06	-2.50 ±0.20	11)
SDSS J1922+372220	0.168876	27500 ±1000	5.40 ±0.10	-2.50 ±0.25	12)
AA Dor	0.261539736	42000 ±1000	5.46 ±0.05	-2.52 ±0.20	13), 14)
NSVS 14256825	0.11037	40000 ±500	5.50 ±0.05	-2.52 ±0.15	15)
ASAS 10232	0.13927	28500 ±500	5.60 ±0.05	-1.80 ±0.20	16)
SDSS J082053+000843	0.096	26700 ±1000	5.48 ±0.10	-2.00 ±0.07	17)
SDSS J162256+473051	0.0696859	29000 ±600	5.65 ±0.06	-1.87 ±0.05	18)
V2008-1753	0.065817833	32800 ±750	5.83 ±0.05	-2.20 ±0.13	19)
VSX J075328+722424	0.2082535	26200	not av.	not av.	20)
OGLE-GD-ECL-11388	0.147806180	30000 ±5000	5.48 ±0.04	not av.	21)
Kon. J064029+385652	0.187284394	55000 ±3000	6.20 ±0.04	-2.24 ±0.40	22)
PTF1 J011339+225739	0.093348	28600 ±600	5.69 ±0.10	-2.21 ±0.09	23)
OGLE 173411	0.3435548	25950 ±130	5.28 ±0.03	-2.48 ±0.11	**this work**
OGLE 361688	0.2723178	27200 ±1300	5.20 ±0.08	-2.39 ±0.03	**this work**
OGLE 416194	0.2666134	35600 ±920	5.34 ±0.20	-2.21 ±0.35	**this work**
Pn 23l1-18	0.211905669	29100 ±900	5.61 ±0.09	-2.25 ±0.10	**this work**
EC 20323-4648	0.463073891	28400 ±400	5.44 ±0.06	-2.36 ±0.33	**this work**

Table A.1: (Continuation)

Currently known, non eclipsing PCEBs with reflection effect					
HS 2333+3927	0.1718023	36500 ±1000	5.70 ±0.10	-2.15 ±0.15	24)
PHL 457	0.3131	26500 ±500	5.38 ±0.05	-2.54 ±0.10	25), 44)
CPD-64 481	0.27726315	27500 ±500	5.60 ±0.05	-2.47 ±0.03	25), 26)
HS2043+0615	0.30156	26157 ±374	5.28 ±0.05	-2.38 ±0.07	27), 28)
V 1405 Ori	0.398	35100 ±800	5.66 ±0.11	-2.50 ±0.20	28)
KBS 13	0.2923	29700 ±100	5.70 ±0.10	-1.70 ±0.10	29)
GALEX J0321+4727	0.26584	29200 ±300	5.50 ±0.10	-2.60 ±0.10	30)
J204613-045418	0.24311	31600 ±600	5.55 ±0.10	-3.00 ±0.05	31)
BPS CS 22169-0001	0.1780	39300 ±500	5.60 ±0.05	-2.68 ±0.18	26), 32)
PG 1017-086	0.073	30300 ±80	5.61 ±0.02	-2.80 ±0.03	33)
PG 1329+159	0.249699	29100 ±873	5.62 ±0.10	-2.40 ±0.10	34), 35)
PG 1438-029	0.336	27700 ±1000	5.55 ±0.15	-2.30 ±0.15	36), 37)
HE 0230-4323	0.451	31552 ±100	5.60 ±0.02	-2.58 ±0.04	26), 27), 38)
JL 82	0.7371	26500 ±500	5.22 ±0.10	-2.55 ±0.10	26), 33), 38)
FBS 0117+396	0.252	28500 ±500	5.42 ±0.10	-3.05 ±0.10	39)
UVEX J0328+5035	0.11017	28500	5.50	not av.	40)
Feige 48	0.376	29500 ±300	5.50 ±0.05	-2.93 ±0.05	41), 42)
KIC 11179657	0.3944769	26000 ±800	5.14 ±0.13	not av.	43)
KIC 02991403	0.4430428	27300 ±200	5.43 ±0.03	not av.	43)
PG 2259+134	0.16345852	30500 ±300	5.62 ±0.17	-1.69 ±0.10	**this work**
MCT 0049-3059	0.2428139	28970 ±190	5.43 ±0.04	-2.49 ±0.27	**this work**

Referenzen: 1) For et al. (2010), 2) Østensen et al. (2010a), 3) Vučković et al. (2007), 4) Schindewolf et al. (2015),5) Drechsel et al. (2001), 6)Østensen et al. (2007), 7) Lee et al. (2009), 8) Wood & Saffer (1999), 9) Polubek et al. (2007), 10) Geier et al. (2014), 11) Barlow et al. (2013), 12) Schaffenroth (2015), 13) Rauch (2004), 14) Kudritzki et al. (1982), 15) Almeida et al. (2012), 16) Schaffenroth et al. (2013), 17) Geier et al. (2011c), 18) Schaffenroth et al. (2014b), 19) Schaffenroth et al. (2015), 20) Pribulla et al. (2013),21) Hong et al. (2017), 22) Derekas et al. (2015), 23) Wolz et al. (2018), 24) Heber et al. (2004), 25) Schaffenroth et al. (2014a), 26) Nagel (2012), 27) Lisker et al. (2005), 28) Geier et al. (2014), 29) Østensen et al. (2010b), 30) Kawka et al. (2010), 31) Geier et al. (2011b), 32) Geier et al. (2010), 33)Maxted

et al. (2002), 34) Maxted et al. (2001), 35) Morales-Rueda et al. (2003), 36) Saffer et al. (1994), 37) Green et al. (2005), 38) Edelmann et al. (2005), 39) Østensen et al. (2013), 40) Kupfer et al. (2014), 41) Heber et al. (2000), 42) O'Toole & Heber (2006), 43) Kawaler et al. (2010), 44) Geier et al. (2013)

Bibliography

Abt, H. A. 1983, ARA&A, 21, 343 [ADS]

Almeida, L. A., Jablonski, F., Tello, J., et al. 2012, MNRAS, 423, 478 [ADS]

Barlow, B. N., Kilkenny, D., Drechsel, H., et al. 2013, MNRAS, 430, 22 [ADS]

Bloemen, S., Marsh, T. R., Østensen, R. H., et al. 2011, MNRAS, 410, 1787 [ADS]

Carroll, B. W., & Ostlie, D. A. 2007, An introduction to modern astrophysics, Vol. 2 (Pearson International Edition)

Chen, X., Han, Z., Deca, J., et al. 2013, MNRAS, 434, 186 [ADS]

Derekas, A., Németh, P., Southworth, J., et al. 2015, ApJ, 808, 179 [ADS]

Dorman, B., Rood, R. T., & O'Connell, R. W. 1993, APJ, 419, 596 [ADS]

Drake, A. J., Djorgovski, S. G., Mahabal, A., et al. 2015, ApJ, 696, 870 [ADS]

Drechsel, H., Haas, S., Lorenz, R., et al. 1995, A&A, 294, 723 [ADS]

Drechsel, H., Heber, U., Napiwotzki, R., et al. 2001, A&A, 379, 893 [ADS]

Edelmann, H. 2003, PhD thesis, Friedrich-Alexander-Universität Erlangen-Nürnberg [LINK]

Edelmann, H., Heber, U., Altmann, M., et al. 2005, AAS, 442, 1023 [ADS]

Eggleton, P. 2006, Evolutionary processes in binary and multiple stars, Cambridge Astrophysics Series No. 40 (Cambridge University Press)

Espinosa Lara, F., & Rieutord, M. 2012, A&A, 547, 32 [ADS]

Ferguson, H. C., Davidsen, A. F., Kriss, G. A., et al. 1991, APJ, 382, 69 [ADS]

For, B.-Q., Green, E. M., Fontaine, G., et al. 2010, APJ, 708, 253 [ADS]

Geier, S. 2015a, Sterne und Weltraum, 38 [LINK]

—. 2015b, Seminar Doppelsterne und extrasolare Planeten, Friedrich-Alexander-Universität Erlangen-Nürnberg

Geier, S., Heber, U., Edelmann, H., et al. 2013, A&A, 557, 122 [ADS]

Geier, S., Heber, U., Podsiadlowski, P., et al. 2010, A&A, 519, 25 [ADS]

Geier, S., Hirsch, H., Tillich, A., et al. 2011a, A&A, 530, 28 [ADS]

Geier, S., Kupfer, T., Heber, U., et al. 2015, A&A, 577, 26 [ADS]

Geier, S., Maxted, P. F. L., Napiwotzki, R., et al. 2011b, A&A, 526, 39 [ADS]

Geier, S., Østensen, R. H., Heber, U., et al. 2014, A&A, 562, 95 [ADS]

Geier, S., Schaffenroth, V., Drechsel, H., et al. 2011c, ApJ, 731, 22 [ADS]

Green, E. M., For, B.-Q., & Hyde, E. A. 2005, ASPC, 334, 363 [ADS]

Groot, P. J. 2012, ApJ, 745, 55 [ADS]

Han, Z., Podsiadlowski, P., Maxted, P., et al. 2002, PASP, 336, 449 [ADS]

Han, Z., Podsiadlowski, P., Maxted, P. F. L., et al. 2003, MNRAS, 341, 669 [ADS]

Heber, U. 1986, A&A, 155, 33 [ADS]

—. 2009, ARA&A, 47, 211 [ADS]

—. 2016, PASP, 128, 966 [ADS]

Heber, U., Drechsel, H., Østensen, R. H., et al. 2004, A&A, 420, 251 [ADS]

Heber, U., Reid, I. N., & Werner, K. 2000, A&A, 363, 198 [ADS]

Hilditch, R. W. 2001, An introduction to close binary stars (Cambridge University Press)

Hirsch, H. 2009, PhD thesis, Friedrich-Alexander-Universität Erlangen-Nürnberg [LINK]

Hong, K., Lee, J. W., Lee, D.-J., et al. 2017, PASP, 129, 14202 [ADS]

Irrgang, A. 2014, PhD thesis, Friedrich-Alexander-Universität Erlangen-Nürnberg [LINK]

Kallrath, J., & Linnell, A. P. 1987, ApJ, 313, 346 [ADS]

Kawaler, S. D., Reed, M. D., Østensen, R. H., et al. 2010, MNRAS, 409, 1509 [ADS]

Kawka, A., Vennes, S., Németh, P., et al. 2010, MNRAS, 408, 992 [ADS]

Kilkenny, D., Koen, C., O'Donoghue, D., et al. 1997, MNRAS, 285, 640 [ADS]

Kopal, Z. 1989, The roche problem and its significance for double-star astronomy (Kluwer Academic Publish Library)

Kudritzki, R. P., Simon, K. P., Lynas-Gray, A. E., et al. 1982, A&A, 106, 254 [ADS]

Kupfer, T., Geier, S., McLeod, A., et al. 2014, ASPC, 481, 293 [ADS]

Lee, J. W., Kim, S.-L., Kim, C.-H., et al. 2009, AJ, 137, 3181 [ADS]

Lehmann, H., Southworth, J., Tkachenko, A., et al. 2013, A&A, 557, 79 [ADS]

Liebert, J., & Wehrse, R. 1983, A&A, 122, 297 [ADS]

Lisker, T., Heber, U., Napiwotzki, R., et al. 2005, A&A, 430, 223 [ADS]

Loeb, A., & Gaudi, B. S. 2003, ApJ, 588, 117 [ADS]

Lucy, L. B. 1967, ZA, 65, 89 [ADS]

Maxted, P. F. L., Heber, U., Marsh, T. R., et al. 2001, MNRAS, 326, 1391 [ADS]

Maxted, P. F. L., Marsh, T. R., Heber, U., et al. 2002, MNRAS, 333, 231 [ADS]

Maxted, P. F. L., Marsh, T. R., & North, R. C. 2000, MNRAS, 317, 41 [ADS]

Morales-Rueda, L., Maxted, P. F. L., Marsh, T. R., et al. 2003, MNRAS, 338, 752 [ADS]

Nagel, K. 2012, Master's thesis, Friedrich-Alexander-Universität Erlangen-Nürnberg [LINK]

Napiwotzki, R., Koester, D., Nelemans, G., et al. 2002, A&A, 386, 957 [ADS]

Napiwotzki, R., Yungelson, L., Nelemans, G., et al. 2004, ASPC, 318, 402 [ADS]

O'Connell, R. W. 1999, ARA&A, 37, 603 [ADS]

Østensen, R. H., Geier, S., Schaffenroth, V., et al. 2013, A&A, 559, 35 [ADS]

Østensen, R. H., Green, E. M., Bloemen, S., et al. 2010a, MNRAS, 408, 51 [ADS]

Østensen, R. H., Oreiro, R., Drechsel, H., et al. 2007, ASPC, 372, 483 [ADS]

Østensen, R. H., Silvotti, R., Charpinet, S., et al. 2010b, MNRAS, 409, 1470 [ADS]

O'Toole, S. J., & Heber, U. 2006, A&A, 452, 579 [ADS]

Perryman, M. 2011, The Exoplanet Handbook, Vol. 1 (Cambridge University Press)

Pietrukowicz, P., Mróz, P., Soszyński, I., et al. 2013, AcA, 63, 115 [ADS]

Podsiadlowski, P., Han, Z., Lynas-Gray, A. E., et al. 2008, ASPC, 392, 15 [ADS]

Politano, M., Taam, R. E., van der Sluys, M., et al. 2008, ApJ, 687, 99 [ADS]

Polubek, G., Pigulski, A., Baran, A., et al. 2007, ASPC, 372, 487 [ADS]

Press, W. H., Flannery, B. P., TeukolSky, S. A., et al. 1986, Numerical Recipes - The Art of Scientific Computing, Vol. 1 (Cambridge University Press)

Pribulla, T., Dimitrov, D., Kjurkchieva, D., et al. 2013, IBVS, 6067, 1 [ADS]

Rauch, T. 2004, Ap&SS, 291, 275 [ADS]

Saffer, R. A., Bergeron, P., Koester, D., et al. 1994, ApJ, 432, 351 [ADS]

Schaffenroth, V. 2015, PhD thesis, Friedrich-Alexander-Universität Erlangen-Nürnberg [LINK]

Schaffenroth, V., Barlow, B., Geier, S., et al. 2017, arXiv, 171203823, 1 [ADS]

Schaffenroth, V., Barlow, B. N., Drechsel, H., et al. 2015, A&A, 576, 123 [ADS]

Schaffenroth, V., Classen, L., Nagel, K., et al. 2014a, A&A, 570, 70 [ADS]

Schaffenroth, V., Geier, S., Drechsel, H., et al. 2013, A&A, 553, 18 [ADS]

Schaffenroth, V., Geier, S., Heber, U., et al. 2014b, A&A, 564, 98 [ADS]

Schindewolf, M., Levitan, D., Heber, U., et al. 2015, A&A, 580, 117 [ADS]

Soszyński, I., Pawlak, M., Pietrukowicz, P., et al. 2016, AcA, 66, 405 [ADS]

Soszyński, I., Stepień, K., Pilecki, B., et al. 2015, ACA, 65, 39 [ADS]

Soszyński, I., Udalski, A., Szymański, M. K., et al. 2017, AcA, 67, 297 [ADS]

Udalski, A., Szymański, M. K., & Szymański, G. 2015, AcA, 65, 1 [ADS]

Voigt, H.-H. 2012, Abriss der Astronomie, Vol. 6 (Wiley-VHC)

von Zeipel, H. 1924, MNRAS, 84, 665 [ADS]

Vučković, M., Aerts, C., Østensen, R. H., et al. 2007, A&A, 471, 605 [ADS]

Wade, R. A., & Rucinski, S. M. 1985, A&AS, 60, 471 [ADS]

Wilson, R. E., & Devinney, E. J. 1971, ApJ, 166, 605 [ADS]

Wolz, M., Kupfer, T., Drechsel, H., et al. 2018, OAst, 27, 130

Wood, J. H., & Saffer, R. 1999, MNRAS, 305, 820 [ADS]

Acknowledgement

An dieser Stelle würde ich mich gerne bei all den Leuten bedanken, die mich während dieser Arbeit unterstützt und somit ihr Gelingen überhaupt erst möglich gemacht haben.

Einen besonders großen Anteil hat daran mein Betreuer **Ulrich Heber**, der diese Arbeit erst ermöglichte und mir dabei die Gelegenheit gab, mich noch intensiver mit dem Themenbereich der HW Virginis Systeme zu befassen. Ferner bot er mir die Möglichkeit, an einer internationalen astrophysikalischen Konferenz in Krakau teilzunehmen, wofür ich mich nochmals ganz besonders bedanken möchte. Während der meiner gesamten Zeit auf der Sternwarte wusste ich außerdem seine stets offene Tür und seine Geduld bei jedweder Frage immer sehr zu schätzen.

Großen Anteil an dieser Arbeit haben auch **Stephan Geier** und **Veronika Schaffenroth**, die mir einerseits immer wieder interessante Daten zur Verfügung stellten, sich aber andererseits bei Problemen oder Nachfragen meinerseits auch immer die Zeit nahmen, diese zu beantworten und mir weiterzuhelfen. Auch **Andreas Irrgang** gilt mein Dank; war er doch immer mit Rat und Tat zur Stelle, wenn man ihn bei Datenreduktionsproblemen brauchte.

Daneben möchte ich meinen Arbeitskollegen **David Schneider**, **Jonathan Knies** und **Markus Schindewolf** für die angenehme und immer lustige Arbeitsatmosphäre im Drechsel-Zimmer danken.

Ferner möchte ich **Marilyn Latour** und nochmals **David Schneider** für die schönen gemeinsamen Abende, bei denen wir die verschiedensten kulinarischen Köstlichkeiten probierten, danken. Ich war wirklich froh, euch als Arbeitskollegen an meiner Seite zu wissen.

Abschließend möchte ich dem ganzen Team der Dr. Karl Remeis-Sternwarte danken, die dieses Institut überhaupt erst zu einem so schoenen Arbeitsplatz machen und dazu beitragen, dass es so bleibt. Vielen Dank dafür!

List of Tables

List of Figures

Erklärung

Hiermit erkläre ich, dass die vorliegende Masterarbeit von mir selbstständig verfasst wurde und dass keine anderen als die angegebenen Hilfsmittel benutzt wurden. Die Stellen der Arbeit, die anderen Werken dem Wortlaut oder Sinn nach entnommen sind, sind in jedem einzelnen Fall unter Angabe der Quelle als Entlehnung kenntlich gemacht.

Erlangen, den 11. April 2018   **Maximilian Wolz**